Negative microfilm
received from university

67-1470

JENKINS, Edward Beynon, 1939-
THE INTERPRETATION OF ATMOSPHERIC FLUORESCENCE SIGNALS FROM MULTIJOULE COSMIC RAY AIR SHOWERS.

Cornell University, Ph.D., 1966
Physics, nuclear

University Microfilms, Inc., Ann Arbor, Michigan

PLEASE NOTE:

The negative microfilm copy of this dissertation was prepared and inspected by the school granting the degree. We are using this film without further inspection or change. If there are any questions about the film content, please write directly to the school.

UNIVERSITY MICROFILMS

This is an authorized facsimile, made from the microfilm master copy of the original dissertation or master thesis published by UMI.

The bibliographic information for this thesis is contained in UMI's Dissertation Abstracts database, the only central source for accessing almost every doctoral dissertation accepted in North America since 1861.

UMI® Dissertation Services

From:ProQuest COMPANY

300 North Zeeb Road
P.O. Box 1346
Ann Arbor, Michigan 48106-1346 USA

800.521.0600 734.761.4700
web www.il.proquest.com

Printed in 2003 by digital xerographic process
on acid-free paper

DPBT

INFORMATION TO USERS

This manuscript has been reproduced from the microfilm master. UMI films the text directly form the original or copy submitted. Thus, some thesis and dissertation copies are in typewriter face, while other may be from any type of computer printer.

The quality of this reproduction is dependent upon the quality of the copy submitted. Broken of indistinct print, colored or poor quality illustrations and photographs, print bleedthrough, substandard margins, and improper alignment can adversely affect reproduction.

In the unlikely event that the author did not sent UMI a complete manuscript and there are missing pages, these will be noted. Also, if unauthorized copyringt material had to be removed, a note will indicate the deletion.

Oversize materials (e.g., maps, drawings, shorts) are reproduced by sectioning the original, beginning at the upper left hand corner and continuing from left to right in equal sections with small overlaps. Each original is also photographed in one exposure and is included in reduced form at the back of the book.

Photographs included in the original manuscript have been reproduced xerographically in this copy. Higher quality 6" x 9" black and white photographic prints are available for may photographs or illustrations appearing in this copy for an additional charge. Contact UMI directly to order.

UMI®
A Bell & Howell Information Company
300 North Zeeb Road, Ann Arbor, MI. 48106-1346 USA
734/761-4700 800/521-0600

Biographical Sketch

Edward Beynon Jenkins was born on March 20, 1939, in San Francisco, California. After education in the Berkeley (California) Public School System he attended the University of California at Davis, California, where he received his Bachelor of Arts degree (majoring in physics) in June 1962. He married Miss Myrna Stewart in June 1963. During his attendance at Cornell University, which began in September 1963, he held an NSF Coop Fellowship for one year and a NASA Traineeship for two years. He is presently a member of Phi Kappa Phi honorary society.

Acknowledgements

The author wishes to express his appreciation to Professor Kenneth Greisen, who suggested and supervised this research and gave valuable advice throughout the project's period of operation. It is a pleasure to thank Dr. Seinosuke Ozaki and Dr. Goro Tanahashi, both of whom were visiting professors from Japan, who performed a major contribution in the design, construction, and operation of the pilot experiment in addition to their participation in the overall planning of the experimental approach. The author is also indebted to Mr. Alan Bunner, a fellow graduate student, who also collaborated in this research and made valuable contributions toward its success.

The author is grateful to the staff of the Cornell Computing Center for training in the operation of the CDC 1604 computer and for permission for its use during early morning hours. While the research was underway, the author received financial support from a National Aeronautics and Space Administration Traineeship. The research project was supported by the U.S. Atomic Energy Commission.

Table of Contents

Table of Contents (continued)

FOREWORD

The research to be described was carried out by the author collaborating with the Cornell University Cosmic Ray Group. A principal co-worker, Mr. Alan Bunner, has directed his efforts toward determining with some care the character and strength of the particle-excitation fluorescence effect in air, the mechanism upon which the experiment is dependent for the detection of energetic cosmic ray air showers. In addition he has also been intimately connected with the design and fabrication of the electronics in the pilot version of the experimental apparatus. Mr. Bunner has described the results of his undertakings in his Ph.D. thesis.[28] The author, on the other hand, in addition to surveying the general problems and implications associated with the gathering of information from air showers sensed by the proposed method of detection, has been principally concerned with devising a method of measuring and interpreting the signals to be received from the pilot experiment. This document and Bunner's thesis therefore concentrate on different topics relevant to a study of the detection scheme, and it is suggested that the interested reader consult both accounts for a complete survey of subject material applicable to the technique under consideration. Both Mr. Bunner and the author briefly outline the results of the other's work to give a balanced presentation in each case. It is inevitable that there should be some overlap of material in the separate discussions; however, one will

find considerable variance in the emphasis and choice of detail in the treatment of the few subjects having a mutual coverage. Frequent reference to Bunner's thesis will be made in the discussion of matters treated more superficially here.

Following a presentation of background material and a discussion of interesting theoretical problems associated with energetic cosmic rays in the first two chapters, we shall explore in Chapters III and IV the nature of the scintillation process and make quantitative predictions relating to the effectiveness of the cosmic ray detection scheme. Chapter V gives a description of the apparatus in the pilot experiment, together with a summary of results obtained after several years' running. Chapter VI outlines in a general fashion the underlying problems associated with the extraction of information from the received signals. The expected appearance of air shower signals for the pilot experiment and the analysis of typical pulse forms are presented in Chapter XII, which is followed by a concluding chapter describing the Cornell Group's future plans for fabricating an improved version of the experiment.

The aforementioned chapters are of general interest in discussing the overall problem of cosmic ray detection by the proposed method. Chapters VII through XI, on the other hand, deal with highly specific details of experimental and analytical techniques which should be of interest only to a person who would wish to critically examine the more intricate

methodology. It is suggested, therefore, that the reader interested in restricting his attention to a general survey of the problem omit the latter chapters.

I. INTRODUCTION

As experimental facilities have been enlarged and refined through the years, investigators concerned with observing the presence of energetic cosmic rays have been able to extend the range of detectability into regions of higher energies where the particles become extremely scarce. Recent experiments[1,2], for instance, have established the existence of incoming particles having kinetic energies which reach as high as 10^{19} to 10^{20} electron volts. The flux in this energy range is extremely low: It is estimated to be in the neighborhood of several events per year per ten square kilometers. This scarcity accounts for the difficulty of past and present experiments to detect many events --less than a dozen have been observed altogether. However the mere existence of these highly energetic cosmic rays carries in itself considerable astrophysical significance, as we shall see later. Figure 1.1 shows an approximate representation of the integral energy spectrum of primary cosmic rays[3].*

The infrequency of very energetic events necessitates the planning of experiments sensitive over a large area to the extensive air showers produced by the primary particle as it hits the atmosphere. Generally the conventional means for detecting an air shower consists of having an array of particle detectors spread over a region of ground large enough to insure a reasonably good count rate. The arrival of a large air shower is signified by coincident detection of secondary particles in

*Nearly identical plots of the spectrum may be seen in references (4) and (5).

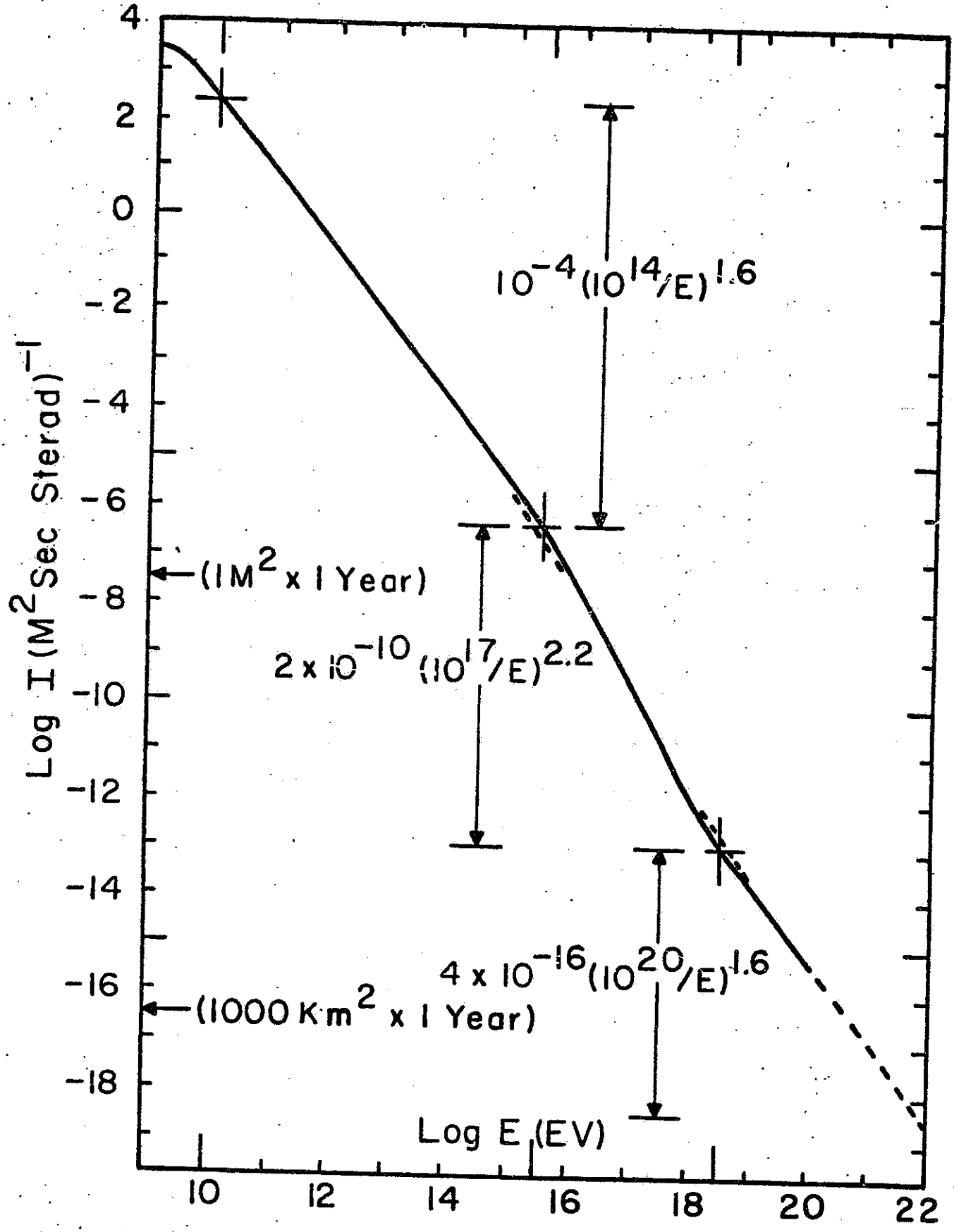

Figure 1.1 Approximate integral energy spectrum for primary cosmic rays.

a number of nearby detectors. The detectors must be close enough to one another to allow some determination of the spatial characteristics of the particle density in the shower as it hits the earth. As a rule the size of the array is limited by economic considerations.

In contrast to the direct measurements of air showers by particle detection, one may consider monitoring various forms of electromagnetic radiation given off during an event. For instance, some success has been found in viewing the Čerenkov light produced in the atmosphere by the relativistic particles in the shower[6]. Owing to the low refractive index of the atmosphere, the maximum angle of emission is small (1°), and the Čerenkov light is confined to a narrow region surrounding the air shower. In reality the angle of emission of the light with respect to the shower axis is chiefly determined by the angular distribution of the shower's relativistic electrons undergoing multiple Coulomb scattering. Studies[7,8] have shown that the detectability of the shower falls off rapidly with distance away from the shower axis, however the use of optical imaging techniques[9] allows one to determine the incoming direction of the primary with good accuracy. Nonetheless, as in the case of the particle detection method, the effective area is limited, and the information arrives almost instantaneously, thus giving little indication of the shower development in time.

Recently several papers have appeared[10,11] which reported

the observation of radio pulses emitted from air showers. The chief mechanisms involved in the radio emission appear to be attributable to Čerenkov and synchrotron radiations. Kahn and Lerche[12] have done a theoretical investigation of the strength of the radio signals which might be expected. Colgate[13] has suggested that radio detection combined with optical monitoring may allow one to detect energetic showers at some distance from the apparatus.

A number of investigators[14,15] have shown interest in devising new methods of shower detection, and in particular K. Greisen of Cornell University has suggested that an investigation should be made to ascertain the feasibility of detecting large air showers by the optical observation of the fluorescence radiation emitted isotropically from the shower region in the atmosphere. It is the intention of the study presented here to carry out this proposal by exploring the practical considerations related to the detectability of air showers by atmospheric scintillation. On the basis of preliminary calculations, which now appear to have been somewhat optimistic, a pilot experiment was designed and constructed by the Cosmic Ray Group at Cornell to utilize this method to detect air showers created by primary particles whose energies exceed 10^{19} electron volts. Observing stations were constructed in the countryside surrounding Ithaca, New York, which monitored, by means of five large photomultiplier tubes facing different directions, the night sky for pulses of light. Concurrent with the running of the

experiment, detailed computations were made by the author on the expected intensity and character, together with the readability and analyzability, of signals which could be obtained with the apparatus in use at the time.

Measurements performed by members of the Cornell Cosmic Ray Group, the results of which will be summarized later, indicate that the atmosphere acts as an inefficient scintillator in the ultraviolet region when it is excited by ionizing radiation. In spite of the poor light yield for a given energy loss of the secondary electrons in an air shower, the overwhelming quantity of energy available in the type of event we hope to detect gives us some promise of being able to utilize this effect in an experiment. Since the radiation is emitted isotropically, in principle a single observing station designed to observe the scintillation light coming from any direction has an effective area of sensitivity for events determined by the line of sight distance. In practice, however, we shall learn that optical intensity limitation will restrict the sensitivity of the pilot experiment to a region within five to ten kilometers from the station.

A major portion of this study is devoted to the derivation of a means of data interpretation for the pilot experiment. The mathematical treatment of the recorded information was devised by the author with the hope that it would be applied to a fair number of meaningful events which were anticipated to be recorded during the years of running the experiment.

Unfortunately the experiment yielded events which, after being carefully scrutinized analytically, either were of too low a signal to noise ratio to be useful or seemed to lack a number of basic requirements for self-consistency. Although the presentation of a detailed description of the analysis technique specifically applicable to the pilot experiment may therefore seem unworthy of serious consideration, many important lessons concerning the nature of the uncertainties in measurement and the basic problems involved in deciphering the information may nonetheless be learned by examinating the procedures devised in this instance. Much of the treatment, especially the later stages of the analysis, is of a general enough nature to be relevant, after minor modifications, to a more advanced version of the experiment presently under construction whose capability for detection far surpasses that of the present version. The improved version, which will be described in the last chapter, would have much smaller errors in measurement for showers of reasonable size, nonetheless the basic nature of the uncertainties should retain the properties which will be discussed shortly, and an exhaustive treatment of the data, employing methods similar to the procedures used in conjunction with the pilot experiment, may be well justified.

II. ASTROPHYSICAL IMPLICATIONS

Particle Trajectories Within the Galaxy

To begin with, a superficial survey may be made on the character of energetic charged particle motions within the galaxy to acquaint ourselves with relevant physical implications and questions which might arise from an interpretation of experimental data on high energy cosmic rays. Up to the present time, measurements of arrival directions of cosmic rays have generally failed to reveal any pronounced anisotropy in the celestial sphere for particles whose energies are roughly 10^{18} ev or less. For instance the findings of experiments performed by groups at MIT[16] and Cornell[1] suggest (without strong proof) the existence of only broad, weak asymmetries in direction. The establishment of isotropy may be principally attributed to the magnetic deflection and consequent mixing of the particles within the galaxy. If one assumes that within the plane of the galaxy magnetic field strengths are on the order of 10^{-5} gauss[17], then according to the relation

$$R = \frac{p}{300ZB} \qquad (2.1)$$

--where p is the momentum of the particle expressed in $\frac{ev}{c}$ (which, for the extreme relativistic case we are concerned with, equals the energy in ev), Z equals the particle's charge, and B is the magnetic field in gauss--we find, provided Z = 1, the cyclotron radius R for 10^{18} ev to be approximately 3×10^{20} cm

or 100 pc, which is smaller than dimensions over which the magnetic field is expected to maintain some degree of regularity. Hence the arrival directions of these particles bear no relation to source directions, and indeed particles of higher charge or considerably lower energy may have been retained within the galaxy by magnetic trapping for considerable periods of time.

On the other hand, as energies of 10^{20} ev are approached, the galaxy becomes relatively transparent; that is, the protons experience little deflection as they penetrate the interstellar medium. The trajectory's radius of curvature, although roughly equal to the radius of the galactic disk, is larger than the mean correlation length of the magnetic field, therefore the deflections would be less than one would calculate for a large homogeneous field. A similar argument could be applied to the passage of cosmic rays between galaxies although there is less certainty about the strength and structure of intergalactic magnetic fields. In general, if better statistics and resolution could be obtained on the arrival directions of very energetic particles, one might hope to identify actual sources or at least make some useful inferences based on the existence of a flux anisotropy (or lack of it).

The magnetic rigidity cutoff for the containment of charged particles within the galaxy may account for the steepening of the energy spectrum above 10^{16} ev as depicted in Figure 1.1. One would expect the abundance of particles from sources

within the galaxy to be highly dependent on trapping times, and the mean galactic containment time for charged particles should steadily decrease as the rigidity progresses from complete containment to complete penetrability. The fact that the spectrum does not fall off precipitously at some energy may be explained by the presence of nuclei of different chemical composition (different Z) which smoothes out the drop-off[5,18]. One might, then, suppose that a plot of intensity versus rigidity (instead of energy) may reveal a more distinct cutoff. For the most part, however, identifications of events in experiments have been made on the basis of air shower size, which is an indication of the energy of the primary cosmic ray. Present and future experiments capable of measuring more subtle features (such as the relative number of muons present or the detailed structure of the air shower's core) may clarify the picture on the chemical compositions.[5,18,19]

Although the statistical certainty in the evaluation of the high energy end of the intensity plot (based on the results of Linsley's[2] observations) shown in Figure 1.1 may be subject to question, it might be tentatively asserted that the reduction of the slope above 10^{18} ev may be due to the appearance of a background of extra-galactic cosmic rays. We shall find some support for the extra-galactic origin of high energy cosmic rays in the discussion that follows.

The Nature of Source Regions

A simplified quantitative examination of the dynamical properties of charged particles whose energies are on the order of 10^{19} to 10^{20} ev demands certain limitations on interpretations related to the character and location of source regions responsible for containment and acceleration of the particles. As the foregoing arguments are presented, it should become increasingly clear that the presence of cosmic rays in this energy range raises some provocative astrophysical questions. The need to answer such questions should add emphasis for the establishment of an experimental research program aimed at determining the composition, arrival directions and energy spectrum of the high energy cosmic rays.

Greisen[3] has pointed out that any plausible natural acceleration process would require a magnetic field whose typical dimension is substantially larger than the gyroradius of the particles. Following an argument similar to that presented by Greisen, we may specify that the radius of a roughly spherical magnetic trapping region be larger than the gyroradius by a factor of some large number K.

$$R > K \frac{P}{300B} \qquad (2.2)$$

However the total magnetic energy of the source would be equal to the product of the energy density $\frac{B^2}{8\pi}$ and the source's volume $\frac{4\pi R^3}{3}$. Substituting Equation (2.2) for R gives the following lower limit for the source energy

$$U > \frac{K^3 p^3}{6(300)^3 B} = 6\times10^{-9}\,\frac{K^3 E^3}{B} \qquad (2.3)$$

An approximate upper limit for the value of B may be obtained by noting that synchrotron radiation energy losses become increasingly important as the field strength is increased. The total energy lost by a charged particle (considered here to be a proton of mass m_p) during one orbit of radius r is[20]

$$\Delta E = \frac{4\pi}{3}\,\frac{\gamma^4}{r}\,\frac{e^2}{m_p c^2}\,m_p c^2 \qquad (2.4)$$

where $\frac{e^2}{m_p c^2}$ is the classical electron radius times $\frac{m_e}{m_p}$ which equals 1.5×10^{-16} cm. Substituting $\frac{p}{300B}$ for r and noting that $\gamma = \frac{E}{10^9 \text{ ev}}$ we get

$$\Delta E = 2\times10^{-40}\,E^3 B \qquad (2.5)$$

We now require that the relative loss of energy be small during one revolution; that is,

$$\frac{\Delta E}{E} = 2\times10^{-40}\,E^2 B \ll 1 \qquad (2.6)$$

Applying the above limitation for B to Equation (2.3) yields a compounded inequality steeply dependent upon energy

$$U \gg 10^{-48}\,K^3 E^5 \qquad (2.7)$$

which, for 10^{20} ev, gives $U \gg 10^{55}$ ergs if one assigns a conservative value of 10 for K. Such a strong relation should preclude the possibility of the energetic particle source regions being ascribable to known features within our own galaxy. With our present knowledge it appears likely that

quasars or galaxies responsible for strong radio emissions would be the best candidates for source regions.

Absorption Processes

Adopting the premise that the energetic cosmic rays must travel large distances before reaching the earth, it is of interest to investigate the effect of known energetic reactions which would be expected to occur in interstellar or intergalactic regions. The probability that high energy nucleons would suffer a significant depletion as a result of interacting with matter, either galactic or extragalactic, seems remote. Even if one adopts an estimate of 2×10^{-29} g/cm^3 (the mass density required to close the universe) for the density of intergalactic gas, the total thickness of matter to the radius of the observable universe (one Hubble Length which equals 10^{28} cm) would be only 0.2 g/cm^2. Similarly our own galaxy having a density of 10^{-24} g/cm^3 (21) and a thickness of roughly 300 pc(22) (9×10^{20} cm) would interpose only 10^{-3} g/cm^2 (times the secant of the galactic polar angle). It is well known that the absorption length for nuclear interactions at high energies should be in the neighborhood of 100 g/cm^2.

On the other hand, the chances for high energy cosmic rays to interact in various ways with different forms of electromagnetic radiation, namely starlight and the recently discovered thermal microwave radiation(23), appear to be significant. For the purpose of exploring the gross quantitative features of the effects one may denote starlight as consisting of visible

photons having a mean energy ε_v equal to roughly 2 ev, with a number density of $0.5/cm^3$ within our galaxy and $5x10^{-3}/cm^3$ in extragalactic space. The microwave radiation, whose mean energy ε_m is around 10^{-3} ev, we may presume to have a constant density of about $5x10^2/cm^3$ over the entire observable universe. Theoretical predictions and experimental evidence (on the interactions of gamma rays in matter) indicate the magnitude of the relevant cross sections and--if applicable--the energy losses which may occur. In the end it is possible for one to compute an order of magnitude for the distance over which an effect would be significant. We may denote this length with microwave photons as L_m, keeping in mind the fact that the length for visible photons L_v is roughly 10^3 L_m within the galaxy and 10^5 L_m in extragalactic regions.

Briefly some relevant processes which have been discussed in the literature are the following:

1. Photodisintegration of nuclei through excitation of the giant dipole resonance: $L_m \approx 2x10^{22}$ cm (24)

2. Inverse Compton scattering of electrons: $L_m \approx \frac{10^{36} \text{ cm}}{E \text{ (ev)}}$ (25)

3. Electron-positron pair production (from a photon-photon interaction) by high energy gamma rays: $L_m \approx 10^{22}$ cm (26,27)

4. Photoproduction of pions from energetic nucleons: $L_m \approx 4x10^{25}$ cm (24)

5. Electron-positron pair production from energetic nucleons: $L_m \approx 10^{27}$ cm (24)

The microwave photodisintegration of nuclei should become important for energies approaching 10^{19} ev/nucleon which makes the appearance of 10^{20} ev air showers initiated by complex nuclei of extragalactic origin seem unlikely. Lower energy nuclei ($\sim 10^{16}$ ev/nucleon) if confined within our galaxy would in all likelihood experience the same effect with the visible starlight. Likewise the relationship expressed above for the L_m of electrons undergoing Compton scattering would suggest that energetic electrons from distant regions would not be observed to arrive at the earth.

For processes involving the production of matter (the remaining three effects listed earlier) the energy threshold E of the cosmic ray (whose rest mass is M) for producing a mass m may be found by equating with the minimum necessary energy M + m in the center of momentum frame the invariant total energy in the rest frame for a head-on collision with a photon whose energy is ε.

$$(E + \varepsilon)^2 - (P - \varepsilon)^2 = (M + m)^2 \qquad (c \equiv 1) \quad (2.8)$$

For highly relativistic cosmic rays (or for cosmic gamma rays) this reduces to

$$E = \frac{2Mm + m^2}{4\varepsilon} \qquad (2.9)$$

The threshold for $\gamma + \gamma \Longrightarrow e^+ + e^-$ may be found from Equation (2.9) (setting M = 0 and $m = 2m_e = 10^6$ ev) to be 2.5×10^{14} ev with microwaves and 10^{11} ev with visible light. Similarly we learn that protons ($M = 10^9$ ev) begin to produce from the microwave component $e^- e^+$ pairs and pions ($m = 1.4 \times 10^8$ ev) at

5×10^{17} ev and 7×10^{19} ev, respectively.

Comparing the threshold energies and interaction lengths with our notions about typical distances of travel for the high energy cosmic rays forces us to conclude that significant reductions in flux should take place. In particular, the pion production should have a drastic effect on extragalactic protons in the energy range applicable to our experiment, and in addition we might question the validity of the extrapolation beyond 5×10^{19} ev of the integral cosmic ray spectrum shown in Figure 1.1. Indeed a careful investigation of the shape of the energy spectrum in the neighborhood of 5×10^{19} ev may provide valuable information on the history of particles in this energy range.

III. CHARACTER OF THE ATMOSPHERIC SCINTILLATION

General Description

The secondary electrons produced in an air shower ultimately lose their energy in the atmosphere by either ionization or excitation of the air molecules. This process may occur either by direct collisions or indirectly through the generation of radiation which in turn interacts with the air or produces additional energetic electrons. After recombination or after the direct excitation, the electronic states of a molecule usually become de-excited upon colliding with a nearby molecule, and the energy is transferred into some form of kinetic motion. Not all of the energy is lost by finally heating the air however; there is some chance that the molecule will spontaneously emit a photon. We are well aware of the nature of this process from ordinary spectroscopy, and in our experiment we are relying on this radiation as a means for detecting the existence of air showers.

The transitions from the excitation levels which will occupy our attention are either the only modes of optical decay permitted by requirements of rigid selection rules or conservation laws, or they are very strongly favored over transitions to other levels (such as magnetic dipole radiations). Hence the collisional losses may be considered to be the only competitive process for the particular optical emissions involved. The mean collision frequency of a gas is proportional to the

density of the gas times the mean velocity of the molecules. The collision frequency is also proportional to the cross section of course, and we may assign a value for the effective cross section for collisional de-excitation based on measurements on the extent of the quenching of the spectral emissions. The cross section will be seen to vary among the different lines representing different molecular excited states. The total rate of de-excitation for n molecules at a particular level is given by

$$\frac{dn}{dt} = n(f_r + f_c) \tag{3.1}$$

where f_c equals the collision frequency and $\frac{1}{f_r}$ is the state's mean lifetime given by the sum of the Einstein coefficients for radiative transition to all lower levels. The efficiency for the conversion of excitation energy into light, therefore, may be defined by the following ratio of transition rates:

$$E = \frac{nf_r}{n(f_r + f_c)} \tag{3.2}$$

Since $f_c \propto \rho\bar{v}$ which in turn is proportional to the pressure divided by the square root of the absolute temperature, we may alternately express the efficiency in terms of pressure and temperature by the form

$$E = \frac{1}{1 + \frac{p}{p_o}\sqrt{\frac{T_o}{T}}} \tag{3.3}$$

where p_o equals the pressure at which the collisional and optical de-excitation rates are equal (for a temperature $T_o \equiv 293°K$).

It is dangerous to assume that the intensities of various emission lines resulting from ionizing radiation in air will correspond to spectral patterns found in other natural processes. Electric arc discharges in air, for instance, do not contain electrons whose energies greatly exceed the breakdown potential gradient times the mean distance between collisions. Hence levels of high energy will not be easily excited, and the population of lower levels may not resemble the distribution obtained from faster electrons. Although they are excited by energetic particles, auroral displays occur in very low pressure regions of the atmosphere where the collisions are relatively infrequent and where there is an abundance of atoms and ions. In the end, we must resort to actual laboratory experiments carried out to observe the optical transition radiation caused by energetic charged particles in order to obtain quantitative data on the nature of the air's scintillation yield. It is difficult to estimate beforehand the relative probability of obtaining various levels of excitation since a number of production modes may play an important role in populating the states. A summary of the theoretical interpretations related to the processes involved may be found in reference 28.

The apparent inconsistencies existing among laboratory measurements performed by a number of investigators[14,29,30] prompted a survey to be made by Mr. Alan Bunner, Dr. Seinosuke Ozaki and Dr. Kenneth Greisen at Cornell. Accurate quantitative determinations of the line strengths for a given amount of energy loss were necessary to ascertain which spectral regions

are most important to observe in the cosmic ray experiment and to estimate an expectation for the total signal strength within a given wavelength range. Three sets of measurements were taken: the first two were performed at the Cornell electron synchrotron, and the third set used the University of Rochester cyclotron which supplied deuterons as a source of ionizing radiation. The measurements taken at Cornell were not as satisfactory as the ones performed at Rochester because of background problems resulting from shielding difficulties.

Results of Measurements

A detailed coverage of the techniques employed, together with a comprehensive outline of the results, has been given by Mr. Bunner[28,31]. We shall summarize here only some of the more important conclusions obtained from the measurements. The primary source of useful radiation comes from nitrogen. At normal pressures oxygen transitions are strongly quenched, and the overall contribution of light from oxygen is much less than one percent of the amount found from nitrogen. In actuality the presence of oxygen in air severely affects the yield from nitrogen. A twentyfold reduction in light was experienced as a result of mixing a normal abundance of oxygen (20%) to pure nitrogen. The interpretation of this attenuation may be attributed to the fact that the de-excitation cross section for an excited nitrogen molecule colliding with an oxygen molecule is significantly higher than the cross section for an interaction with another nitrogen molecule. Varying the

amount of trace gases (e.g. H_2O, CO_2) found in the atmosphere seemed to have little effect however. Needless to say, at the highest altitudes at which we expect to see air showers the composition of the atmosphere is identical to the sea level mixture.

Outside of some emissions found in the infrared which are of little concern to us because of the lack of phototube sensitivity, the strongest output of light occurs below about 4200 Å. The contributions come chiefly from what are referred to as the first negative and second positive systems. These band systems respectively represent the decays of the many vibrational sublevels of the excited $^2\Sigma_u^+$ state of the N_2^+ ion to the ion's $^2\Sigma_g^+$ ground state and the excited $^3\Pi_u$ state of the N_2 neutral molecule to an intermediate state, $^3\Pi_g$. We need not be concerned over the possibility of the existence of particularly strong resonant self-absorption in the atmosphere at the corresponding wavelengths since neither of the transitions go to the ground state of the neutral nitrogen molecule.

Some measurements on a few lines were made at different pressures to verify the pressure relationship for the efficiency as expressed in Equation (3.3). A plot of one of these measurements is shown in Figure 3.1. The net yield of photons Y per unit track length for an ionizing particle should equal E times a parameter describing the probability that a particular level is excited, which is in turn multiplied by the density of the gas ρ. ρ determines the rate of energy loss per unit length

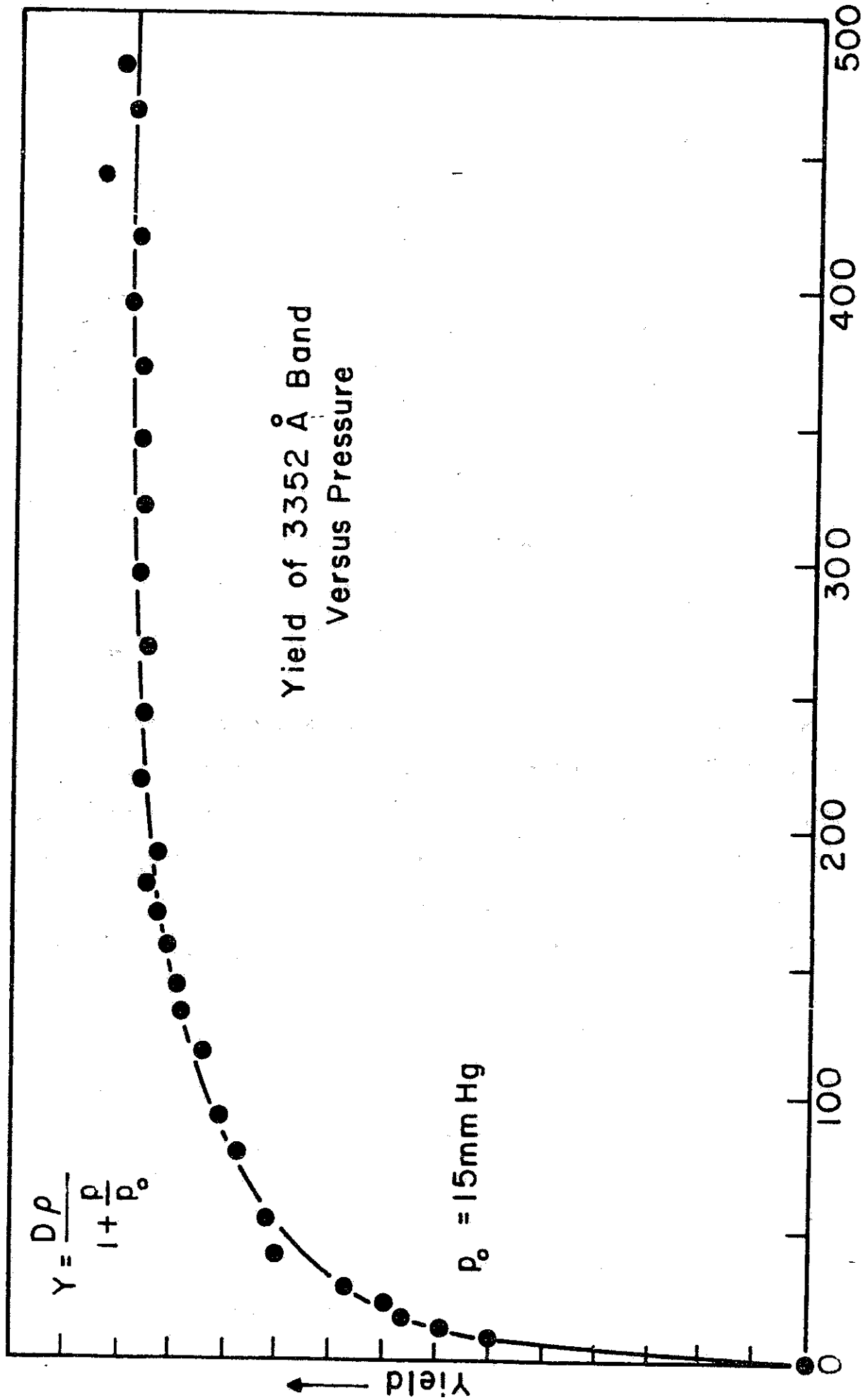

Figure 3.1 A comparison of experimental readings with the predicted behavior

for the charged particle passing through the medium. We may incorporate into a single empirically measurable quantity D the product of the excitation probability per unit energy loss and the energy loss per unit thickness of air ($2.24\ \frac{\text{Mev}}{\text{g/cm}}$), giving us the equation

$$Y = \frac{D\rho}{1 + \frac{p}{p_o}\sqrt{\frac{T_o}{T}}} \qquad (3.4)$$

A drawing showing the spectral profile of the scintillation light for pressures much higher than any of the measured p_o values may be seen if one looks ahead to Figure 12.2. As an aid to calculations for wavelength dependent effects which are to be presented in later chapters, the values for D and p_o are formulated for thirteen principal emission bands which together represent nearly all of the light emitted in the region 3100 Å to 4200 Å. These values with their corresponding wavelengths are listed in Table 3.1. Most of the p_o values quoted here are based on the measurements of other investigators; in all cases D was deduced from the Cornell group's measurements of the yield Y at high pressures ($p \gg p_o$). The D values shown in the table give an indication of the yields which would be found under very low pressure conditions ($p \ll p_o$) where collisional quenching would be nearly absent. The Y values, on the other hand, are representative of the performance under high pressures.

After calculations requiring the use of values quoted in Table 3.1 had been performed, A. Bunner revised some of the

λ(Å)	$D\left(\frac{\text{photons}}{g/cm^2}\right)$	p_o(mm Hg)	$Y\left(\frac{\text{photons}}{m}\right)_{p>>p_o,\ T = 293°K}$
3159	291	6.5	0.300
3371	217	15.0	.517
3469	123	2.5	.049
3500	61	4.6	.044
3537	179	6.5	.115
3577	152	15.0	.363
3711	67	4.6	.049
3756	116	6.5	.120
3805	119	15.0	.282
3914	1970	1.0	.312
3998	105	6.5	.109
4059	49	15.0	.117
4278	103	1.0	.159

Table 3.1 A listing of the emission strength D and quenching pressure p_o for the dominant nitrogen emission features. To facilitate identification of principal transitions, the wavelengths are listed according to the position of the band head; however D represents the total quantity of light emitted over a wavelength interval containing transitions between the many rotational sublevels. All measurements are based on a T_o of approximately 293°K (i.e. a typical laboratory temperature, 20°C).

numbers by taking into account the measurements made by others. The revised numbers, together with a more comprehensive listing of weaker emission bands, may be found in Bunner's thesis[28] which the interested reader may also consult for a detailed account of the basis for choosing the values. A substitution of the more up-to-date numbers (which still retain a moderately large degree of uncertainty) into the calculations to be described later should not alter the results significantly.

In short, the overall efficiency of air as a scintillator is about .004% at pressures found near sea level. This may be compared to the energy loss conversion efficiency typically found with organic crystal, liquid, and plastic scintillators of one to five percent and ten to twenty-five percent for activated inorganic crystals such as ZnS and NaI. For pressures significantly larger than p_o the total photon yield would equal 2.5 photons/m--the sum of the numbers in the far right column of Table 3.1. For viewing air showers, then, one might conservatively estimate a yield corresponding to one photon per meter if allowance is made for atmospheric obscuration at reasonable distances under typical (not optimum) conditions, say with a moderate amount of haze present.

As a concluding remark we might touch upon a subject which is a vital consideration for our cosmic ray detection experiment--namely the rapidity of decay in time for the atmospheric scintillation. The importance of this factor may be realized if we visualize the appearance of the shower as it moves across the sky. If the decay is quite rapid, say on the order of

nanoseconds, the geometrical form of the emitting region would be practically identical to the shape of the shower front at any instant. On the other hand, if the decay time were much longer (on the order of a microsecond or more) a tail would appear whose characteristic length would equal the velocity of light times the decay time. The shower would bring to mind the appearance of a meteor, and a definition of instantaneous shower position from the light signals would be vague. Assuming the de-excitation cross section not to differ much from commonly quoted values for molecular size ($\sim 3 \times 10^{-15}$ cm^2), the collision frequency at sea level would be roughly 5×10^9/sec, which would result in a nominally short decay time even for altitudes as high as thirty kilometers. Nonetheless there was some brief concern over the possibility that considerable decay could result if the light largely resulted from recombination of ions and electrons. Direct observations of the fall times have been made, and fortunately with some assurance it may be said that at least 90% of the light is emitted within half a microsecond. Oxygen plays an important role in eliminating the electron-nitrogen ion pairs by charge exchange processes.

IV. INSTRUMENTAL CAPABILITIES FOR DETECTION

Statistical Fluctuation Noise

Essential to the success of an experiment designed to extract useful information (as outlined in Chapter II) from energetic cosmic rays is the ability of the apparatus to detect air shower events at large enough distances and low enough energies to insure that within a reasonable running time one may have a good collection of well measured events. The ultimate limitation in sensitivity to the reception of scintillation light pulses arises from the fact that every signal pulse has superimposed a random noise signal produced by statistical fluctuations, within short time intervals, of electrons from the detector's photosensitive material. Depending upon the design of the detection system, the dominant source of noise may be generated by either the scintillation light from the event itself or by the ever present night sky background light from stars and the airglow. The following approximate analysis should give us some insight as to the relevance with regard to detection efficiency of different design parameters for a single observing station.

Within a short time interval Δt a photosensitive device, such as a photomultiplier tube, whose efficiency is ε photoelectrons/incident photon and whose surface area is A will, on the average, emit $FA\varepsilon\,\Delta t$ photoelectrons if it is illuminated by a nonvarying light flux of F photons per unit

area per unit time. The fluctuation of this number about the mean value would be Gaussian since the mean value is generally large, and one standard deviation would correspond to $(FA\varepsilon\,\Delta t)^{1/2}$. If an amplifier having a frequency cutoff of $1/\Delta t$ were monitoring the photomultiplier anode current, an AC noise signal would appear whose r.m.s. amplitude would be equivalent to a signal representing $(FA\varepsilon\Delta t)^{1/2}$ photoelectrons per unit time interval Δt (or simply $(\frac{FA\varepsilon}{\Delta t})^{1/2}$ photoelectrons per second). For simplicity we are neglecting additional fluctuations in numbers of electrons between the first few dynodes in the photomultiplier, and furthermore we assume that the amplifier acts as an integrator continuously sampling consecutive time blocks of width Δt. For our experiment, we may think of F as being composed of both the signal pulse from an air shower and the night sky background.

For the sake of generality we may discuss the properties of a photosensitive element without specifying its exact nature or arrangement in an experiment. Such a component would be one of many incorporated into a detection scheme designed to monitor a large portion or all of the night sky. In addition to the sensor's area A and efficiency ε, its viewing acceptance solid angle Ω must be specified. Furthermore it is advantageous to account for varying spectral sensitivities by designating ε in terms of ε_b and ε_s which respectively refer to the efficiencies of detecting background light and scintillation light. The sensor's effective area may, of course, be magnified (with a consequent reduction of Ω) by the use of either a lens or

focusing mirror. Within some optical focusing system one may specifically think of the individual light sensor as being either a small photomultiplier tube or a resolution limited area on the face of a time-gated image intensifier system.

The intensity of the night sky background light is roughly 1.5×10^{-7} erg $cm^{-2} sec^{-1} str^{-1} \mathring{A}^{-1}$ (32) which, after conversion of units and integration over a 2000 $\mathring{A}$ passband, gives 6×10^{5} photons/m^2str μs. The latter quantity may be designated as I_b. As an earlier discussion pointed out, the noise signal arising from this background would be $(I_b \Omega A \varepsilon_b / \Delta t)^{1/2}$. There exists some uncertainty in this number since I_b is very much dependent on local weather conditions, especially if within approximately 15 km of the observing station there are cities or towns producing artificial light which may be scattered by haze or off of clouds. The value quoted for I_b would, therefore, represent a lower limit for the background intensity.

Intensity of an Air Shower Signal

We shall now derive the signal intensity at a given instant for a shower resulting from a primary cosmic ray of a given energy. The simplest example to consider occurs when the shower front is moving perpendicular to the line of sight--that is, the shower is at its closest approach distance which we shall designate as r_o. Assuming the entire shower is contained within the field of view (whose size is Ω) of a particular detector, the signal expressed in terms of photoelectrons per unit time would be

$$S = NYc\frac{A}{4\pi r_o^2}\varepsilon_s \qquad (4.1)$$

where N is the number of electrons in the shower (which we shall assume, for now, to be at the maximum stage of development) and Y is the fluorescence yield of a single electron for a track length of one meter. Using a model derived by Greisen[33] for the electromagnetic cascade the quantity 7×10^{-10} E is a reasonable substitution for N where E is the primary energy expressed in electron volts.

It is worth mentioning at this point that the representation of shower intensity at the closest approach distance does not particularly bias S toward a value more favorable than the average signal obtained for the duration of the event. In actuality Equation (4.1) may be generalized for the non-perpendicular case by simply multiplying it by a factor of $(1 - \sin\theta)$ where θ is the angle of observation with respect to the perpendicular closest approach point (see Figure 4.1). The derivation of this more general relation, which in addition to accounting for an inverse square distance law must also allow for the fact that the light signal travels the same speed as the shower itself, will be discussed in Chapter VI where the time character of an event is treated in detail. For reasonable observing configurations the $(1 - \sin\theta)$ factor averages to one, thus making Equation (4.1) a good representation of an expected average signal pulse height.

The interpretation of Equation (4.1) for any shower whose "impact parameter" is r_o has its largest error attributable to

the uncertainty of the position of the shower maximum. Indeed, a small zenith angle shower whose primary energy exceeds 10^{20} ev may not reach its maximum before it hits the ground. It is difficult to incorporate in any simple manner the results of shower growth models into a general survey since the position and apparent angular extent of the region where N is comparable to the maximum value depends upon the zenith angle and energy as well as the details of the shower trajectory with respect to the observer. It should suffice to say that, on the average, the shower maximum occurs at or near the closest approach point.

Although the assumptions regarding the position and development of the shower may appear to be gross oversimplifications of a complex variety of possible configurations, a comparison with the more exacting study applicable to the actual pilot experiment demonstrates that results derived from Equation (4.1) yield an accurate enough representation for a broad survey of instrumental response capabilities and count rates. The implication from Equation (4.1) that r_o and E (or N_{max}) are suitable parameters for classifying events is also corroborated by the more specific analysis just mentioned.

A convenient means of visualizing the family of events having an impact parameter equal to or less than r_o is to think of all possible trajectories approaching the earth which either intersect or are tangent to a sphere surrounding the observing station. The intersection could occur below as well as above the ground.

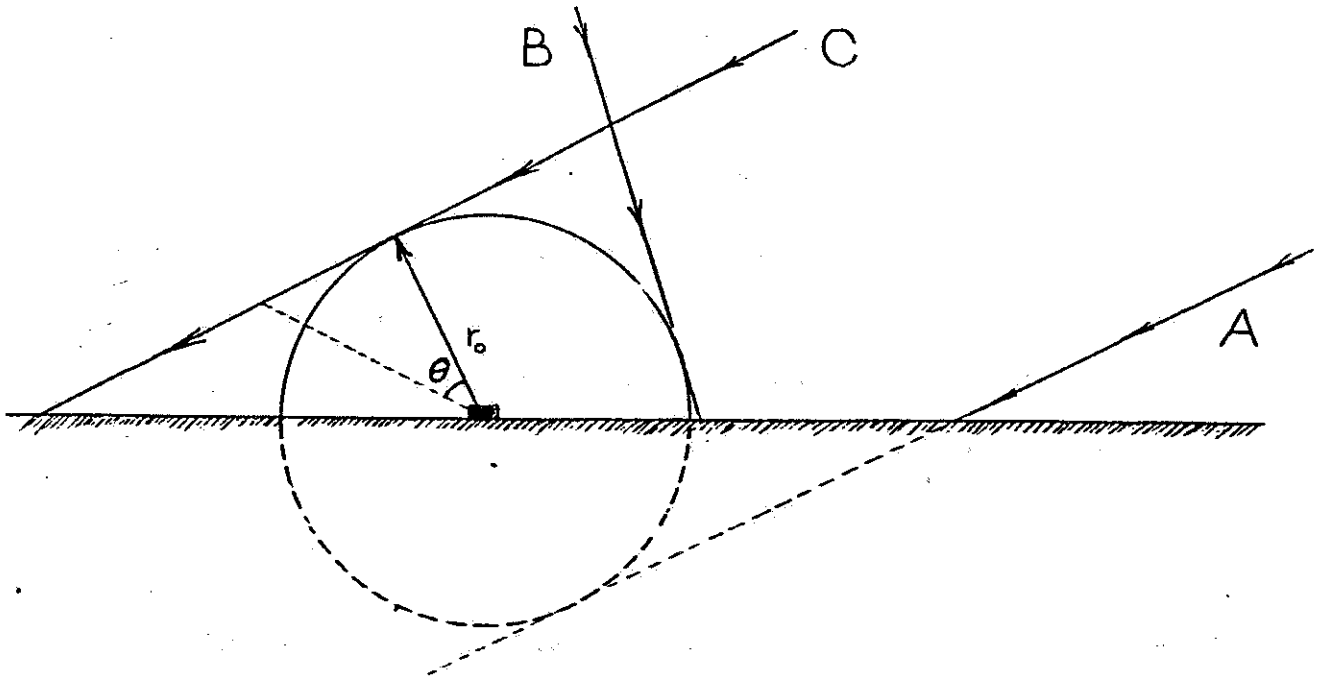

Figure 4.1

An interesting consequence of the earlier discussion regarding the $(1 - \sin\theta)$ factor is that if the maxima for comparable showers in the examples shown in Figure 4.1 are near the ground, the signal pulse height from event A will be larger than the signal from C even though event A on the average is farther from the observer. This is a result of the fact that as shower A progresses the light signal destined for the observer will pile up and be registered within a short time interval since it is emitted at a small angle away from the shower direction. Shower C on the other hand has trajectory elements of length which are observed over longer time intervals while the shower is receding from the observer.

Event Readability

The instantaneous signal to noise ratio

$$S/n = S\Delta t^{1/2}(S + I_b\Omega A\varepsilon_b)^{-1/2} \qquad (4.2)$$

by itself is not a good criterion for the detectability or interpretability of an event. One must in addition have a rough idea of how many independent readings at the given S/n ratio are available for simultaneous incorporation into the analysis. The number of readings accessible during the recorded pulse's brief duration is limited by the requirement that the time between readings must be as large as the rise time of the amplifier system to avoid correlation of noise errors from one measurement to the next. Following a usual statistical practice, one may loosely define the net relative error for a collection of readings as equal to the relative error of each reading divided by the root of the number of readings. We may therefore introduce an event quality criterion Q which is the reciprocal of the net error and is defined in the following manner:

$$Q = (\text{average S/n ratio})(\text{number of readings})^{1/2} \qquad (4.3)$$

The actual relationship between Q and the uncertainty of specific shower parameters to be determined is generally not clearly defined, outside of the fact that it is roughly an inverse relation. Nonetheless the use of Q as a basis for comparison of events facilitates the broad categorization to be presented shortly.

One should be aware of the fact that for a given event and detector the value of Q is independent of the amplifier response time. As Δt is increased by some factor x, for instance, the S/n ratio increases by $x^{1/2}$, however the number of readings available decreases by x making a zero net change in Q. Considerations of amplifier rise times in the design of an experiment are therefore governed only by the requirement that Δt be comparable to the shortest interval of time over which a nearby shower would exhibit an interesting change. The amplifier's frequency cutoff should not be so high as to yield a burdensome quantity of very noisy measurements. That is, to some degree the lack of sensitivity to high frequencies may be used to an advantage in smoothing the signals over short enough time intervals, a process which might otherwise be accomplished by some mathematical averaging process in the data reduction.

As shall be demonstrated in Chapter VI where the time dependence of the apparent shower direction is studied, the duration of the signal pulse is approximately equal to $\frac{r_o}{c}\Delta\theta$ (see Figure 6.2), provided θ is not much greater than zero. $\Delta\theta$ is the angular extent over which N is not much less than N_{max}. A majority of showers will have a $\Delta\theta$ not differing much from unity, exceptions being extreme versions of "A" labeled in Figure 4.1 (small $\Delta\theta$) or conversely type "C" events (large $\Delta\theta$ or possibly θ substantially greater than zero). It should be safe to conclude, therefore, that the characteristic pulse width is of the order of $\frac{r_o}{c}$ which provides $\frac{r_o}{c\Delta t}$ readings. The

would increase proportionally by x.

The applicability of Equations (4.5) and (4.6) should also be restricted by the condition that 1 km $\lesssim r_o \lesssim$ 15 km. Showers too near the station have a large Ω_m and, since $\frac{r_o}{c}$ is so small, are recorded as almost instantaneous pulses. The upper limit of 15 km corresponds to the restriction that the atmosphere is of limited thickness, and at large distances atmospheric absorption of the scintillation light becomes excessive.

Detection Equipment Design Considerations

Not covered by the foregoing analysis is an additional consideration which is of significance in assessing the relation of experimental design parameters to event measurability. In the situations discussed where Q is independent of Ω (i.e. either Equation (4.5b) or $\Omega < \Omega_m$ is valid) some advantage may still be obtained in making Ω as small as possible, as long as the total solid angle covered by a station remains unchanged (by increasing the number of detectors). The precision of directional measurements is directly related to the resolving power of the detector elements for a given Q value. That is to say, the subdivision of the incoming signal into smaller parts by some optical arrangement of known geometry provides in itself additional information over what could be obtained if a single detector were monitoring the same signal.

Optimization of detection instrument design may be accomplished by exploring the many possible combinations of A, ϵ_s, ϵ_b, and Ω in accordance with the requirements of minimizing equipment

cost and complexity. We shall not attempt to make a detailed survey of the many practical conclusions derivable from Equations (4.5) and (4.6) which would have relevance to specific proposals of equipment design. Instead, a few of the more interesting generalizations which may be made will be stated to give us some feeling for the more important guide-posts in engineering an experiment.

For instance, if a station is designed to detect primarily events where the inequality (4.6b) holds, it may prove advantageous to install filters in front of the detectors which absorb regions of the spectrum where there is a large amount of night sky light and relatively little scintillation light. The insertion of the filters in effect would change the ratio $\epsilon_s/\epsilon_b^{1/2}$ in Equation (4.6a) and naturally would be a desirable addition to the apparatus only if the relative absorption of background light exceeded the absorption of the scintillation light squared. If, on the other hand, the night sky light noise were not dominant it would be advisable not to include a filter since ϵ_s would undoubtedly be lower in Equation (4.5a).

The use of an image intensifier system, suggested earlier, has the advantage of a single instrument being equivalent to a large collection of photosensitive detectors each having a small Ω. In addition the data from an event could be presented in a manner which would be easily interpretable--as an actual picture. The time sequence of the shower could be indicated in the record by modulating the gate for the intensifier with

a high frequency square wave, for instance, thus making the event appear as a dotted line.

There are, nonetheless, important practical drawbacks which limit the effectiveness of an image intensifier and introduce design complications. First, the picture built up represents an integration of an image over a long time interval since the entire picture field of the intensifier must be turned on for the total duration of the event. This means the signal image, which appears within a small Ω for a short time, must compete with the buildup of background noise over the extended time period. Secondly, an additional system must be provided for triggering the apparatus since no electrical signal would be available, and the early stages of shower development may not be recorded before the gate is turned on. Amplified electrical signals from simple detectors, on the other hand, may be stored in pulse lines prior to triggering and may be examined within selected time intervals. Nonetheless, it is fair to say that the aforementioned difficulties could be moderated or overcome by some sophisticated and elaborate equipment engineering and by careful programming for event registration.

Returning to the more general discussion on detection stations, there are two principal factors which play an important role in determining the cost--as well as the effort in the construction--of an observing setup.

(a) The total photosensitive surface area needed which is equivalent to the product of the <u>effective</u> area (as defined

earlier) of each detection unit A, each unit's solid angle Ω, and the total number of units $\frac{2\pi}{\Omega}$ (assuming full coverage of the sky).

(b) The number of detection units $\frac{2\pi}{\Omega}$ which determines the extent to which one must duplicate the electronics for amplification, discrimination, and display of signal pulses.

For any particular shower size N, Equation (4.6) tells us that in the night sky background limited case the two price components (a) and (b) are each proportional to r_o^3 if Q, Y, ε_s, and ε_b remain fixed. Events closer to the station than r_o, which would be of better quality than some minimum tolerable Q occurring at r_o, will have a frequency proportional to r_o^2. The count rate of such events will then be proportional to both the area (a) and the number of units (b) to the two-thirds power. If Equation (4.5) is applicable, decreasing Ω will bring no advantage (outside of the considerations mentioned in a previous paragraph), and the count rate will be proportional to the square of the detector area. When the preceding relationships are considered we should bear in mind, of course, the earlier stated restrictions for the range of r_o. In particular, the r_o^2 dependence on count rate becomes inaccurate if r_o is not much larger than 1 km. If one were to include the fixed cost of building a station (exclusive of the items mentioned earlier) one might obtain a rough estimate of whether it may be better to build, widely separated, a few elaborate stations or conversely many simple stations for an

optimum counting rate of showers having a specific energy.

Estimation of Counting Rate

An assessment of the total counting rate for all energies at various distances is useful in determining the number of interesting events that are likely to occur within a given running time interval. Using the approximate integral spectrum I(E) given in Chapter I, an estimation of the counting rate for events above any specified Q value may be made by performing the following calculation. The more general expression for Q, namely Equation (4.4), may be rewritten in the form

$$Q = \frac{NY\epsilon_s}{4\pi r_o^2}\left[\frac{r_o A c}{\frac{NY\epsilon_s c}{4\pi r_o^2} + I_b \Omega \epsilon_b}\right]^{1/2} \qquad (4.7)$$

The value of N at a given r_o which will yield the desired Q may be evaluated by solving the quadratic equation

$$\frac{Y^2\epsilon_s^2 A c}{(4\pi)^2 r_o^3 Q^2} N^2 - \frac{Y\epsilon_s c}{4\pi r_o^2} N - I_b \Omega \epsilon_b = 0 \qquad (4.8)$$

which gives the result

$$N = \frac{2\pi r_o Q^2}{Y\epsilon_s A}\left(1 + \sqrt{1 + (4 I_b \epsilon_b r_o A / c Q^2)}\right) \qquad (4.9)$$

The number of events per unit time exceeding an energy E that one would expect to have an impact parameter falling within r_o and $r_o + dr_o$, assuming the flux to be isotropic, would be $2\pi I(E)$ times the annular area differential $2\pi r_o dr_o$. The total number of events falling within the one to fifteen kilometer range having a quality better than Q would be

$$\text{rate}_Q = \int_{1\text{ km}}^{15\text{ km}} 4\pi^2 I(N)\,dr_o \qquad (4.10)$$

where Equation (4.9) could be substituted for N (which, as stated earlier, equals roughly 7×10^{-10} E).

Experience with a large number of computer simulated events (to be described in a later chapter) indicates that roughly a quarter of all possible events tangent to the sphere of radius r_o have unfavorable enough trajectory configurations (usually of the variety labeled C in Figure 4.1) to give significantly lower Q values than Equation (4.7) would predict. Thus it would be wise to multiply the integral in Equation (4.10) by a factor of 0.75.

Table 4.1 lists some expected count rates for a variety of conditions obtained by numerically integrating Equation (4.10). The rates shown should be taken as very approximate; the largest uncertainty most likely results from the fact that I(E) is poorly known, although errors inherent in the nature of the approximations and assumptions made in deriving the count rate equation may introduce a comparable amount of uncertainty. The failure, in some instances, of the general relationships quoted earlier for specific shower sizes to agree with the results shown in the table arises from the fact that the greatest contribution to the integral comes from small showers near the lower limit of one kilometer where the frequency is not proportional to r_o^2.

Area (m^2) \ Solid Angle (str)	3.0	1.0	0.3	0.1	0.03	0.01	0.003
0.3	.047 .015 .0074 .0046 .0031 .0023	.12 .034 .017 .010 .0067 .0048	.38 .089 .040 .023 .015 .010				
0.1	.018 .0058 .0029 .0017 .0012 .00083	.044 .013 .0063 .0037 .0024 .0016	.12 .030 .014 .0075 .0046 .0031	.29 .061 .024 .013 .0073 .0046	.73 .11 .040 .019 .010 .0061	1.4 .17 .053 .023 .012 .0069	
0.03	.0066 .0021 .00098 .00057 .00037 .00025	.016 .0044 .0020 .0011 .0067 .00044	.036 .0089 .0038 .0019 .0011 .00069	.074 .016 .0058 .0027 .0015 .00088	.14 .024 .0079 .0034 .0017 .0010	.23 .030 .0091 .0038 .0019 .0011	
0.01				.022 .0040 .0013 .00058 .00030 .00017	.035 .0052 .0016 .00065 .00032 .00018	.046 .0059 .0017 .00067 .00033 .00019	.053 .0062 .0017 .00068 .00034 .00019

Table 4.1 Evaluation of the integral in Equatipn (4.10) times a factor of 0.75. The values $\varepsilon_s = 0.06$ and $\varepsilon_b = 0.0165$ were chosen to represent a 10% efficient photosensitive surface covered with a filter of the type used in the pilot experiment. The numbers shown within each box are in terms of events per hour running time for Q values exceeding 10, 20, 30, 40, 50, and 60, respectively.

So far no mention has been made in this chapter concerning an additional contribution of light which could result from the Čerenkov radiation of highly relativistic electrons passing through the atmosphere. Calculations performed by Brunner[8] (not to be confused with Bunner) indicate that the total quantity of Čerenkov light received from a nearby air shower should exceed the total yield of photons from the scintillation process. To be specific, he computes that a 10^{19} ev shower may produce within a 4,000 to 7500 Å passband 750 photons/cm^2 at a distance of 1 km from the shower axis and 32 photons/cm^2 at 2 km. By comparison, S (given by Equation 4.1) times $\frac{r_o}{c}$ gives corresponding values for scintillation yields of 110 and 55 photons/cm^2 for 1 and 2 km, respectively. Depending upon the spectral admittance of the apparatus, then, we see that for 10^{19} ev the Čerenkov light's intensity surpasses that of the scintillation light at a distance somewhere between one and two kilometers. This gives evidence, therefore, that in practice many of the numbers quoted in Table 4.1 may be somewhat pessimistic, although it must be remembered that the drop-off for Čerenkov light is quite rapid with increasing distance from the shower axis.

The estimation of the net counting rate obtainable in actual practice for an experiment must provide for the fact that a station is able to run during a comparatively small fraction of the time--only on clear, moonless nights. An upper limit to the attainable duty factor for an area whose climate is similar to that of Ithaca, N.Y., is roughly five percent. Almost three times this value might be obtained for a station located in a

region, such as a desert, having a more favorable climate. As a quick guide to the interpretation of Table 4.1 the following equivalence relationships are valid for a five percent running time:

$$0.83 \text{ events per hour run time} = 1 \text{ event/day}$$
$$0.027 \text{ events per hour run time} = 1 \text{ event/month} \quad (4.11\ a,b,c)$$
$$0.0023 \text{ events per hour run time} = 1 \text{ event/year}$$

In closing, it may be worthwhile to make a few brief subjective comments on the quantitative properties of Q. For a station having a relatively large Q for each unit, experience obtained from analyzing real and computer simulated events for the experiment actually carried out (described in the next chapter) suggests that Q must be at least ten or twenty to make even a tentative suggestion that an observed set of pulses indeed came from an air shower and was not spurious. Events having a Q value exceeding about twenty-five yield enough information to give meaningful, although inaccurate, data on shower size and direction. Any events having a Q greater than forty or fifty would be analyzable to a fair degree of precision. One should remember, however, that an experiment utilizing narrow angle detectors may in general be able to have lower Q values assigned to the descriptions just given.

V. DESCRIPTION OF THE PILOT EXPERIMENT

In an effort to gain experience in the experimental technique of detecting large air showers by observing the atmospheric scintillation light a detection station of modest scale and complexity was constructed in 1964 by Dr. Seinosuke Ozaki and Mr. Alan Bunner at Cornell. At the time it was hoped that the experiment would yield a handful of events which would add some useful information about the nature of cosmic rays in an energy region which as yet has been poorly explored. Initial calculations similar to the ones presented in the preceding chapter indicated that the detection station would be capable of detecting readable events with a frequency of approximately one per month assuming that the intensity spectrum shown in Chapter I were correct. Unfortunately, after the experiment had been constructed, it became apparent that the estimation of detection efficiency had to be revised downwards since the concurrent investigations made by Mr. Bunner and the others on the scintillation efficiency of air (described in Chapter III) showed that light yields quoted by a number of other investigators were too high.

In 1965 and 1966 two additional stations were constructed by Dr. Goro Tanahashi in an effort to increase the net count rate. All three stations were situated on hilltops in the countryside reasonably distant from towns. The original intention was to place the three stations roughly ten kilometers apart in a triangular configuration. A small fraction of the area of coverage for each station would be common to the other

stations giving some chance that a few events might be registered by more than one station. Prior to the construction of the third station, however, the decision was made to place it adjacent to the second station to serve as a verification that barely readable pulses received by one station were likewise recorded by the other station alongside. This procedure was used as a check on the credibility of interesting looking pulses received and as a method of determining the likelihood of receiving spurious pulses generated within the electronics which might erroneously be interpreted as an event.

Up to the time of this writing, the three stations have been operated continuously under the supervision of the author, Mr. Bunner, and Dr. Tanahashi. It is anticipated that the present experiment will continue to run until a more advanced version (to be described later) with much higher detection capability will replace it. The results gathered to date from the three stations will be discussed in a later section of this chapter. The following description applies to all three stations which are of identical design.

Photomultiplier Tube Units

Situated on top of the shack housing the electronics and the work area are, as shown in Figure 5.1, five photomultiplier assemblies--one facing vertically and the remaining four pointing 30° above the horizon toward north, south, east, and west. Each unit has a response function roughly equal to the

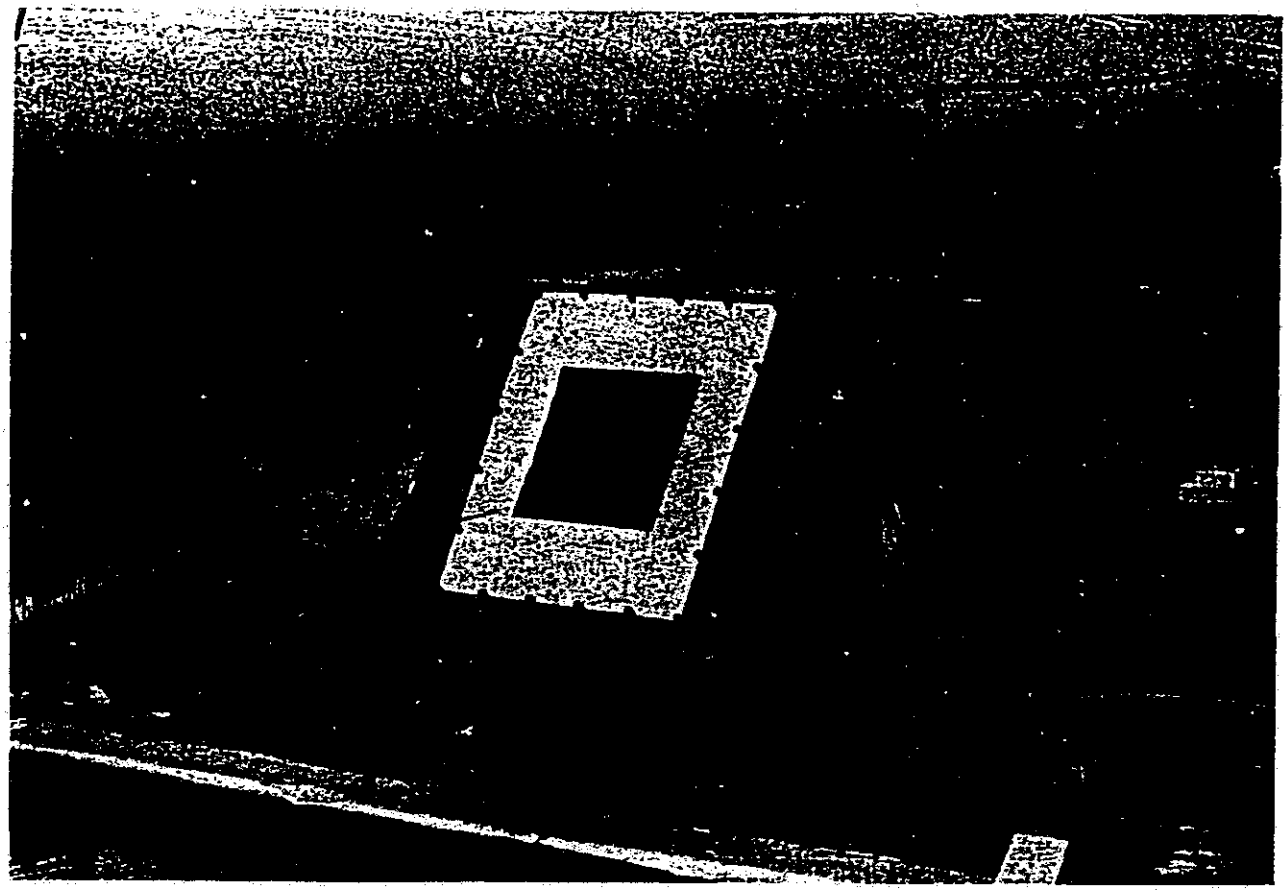

Figure 5.1

cosine of the incident angle and is capable of detecting light coming from anywhere in front of the plane of the unit's face. The direction the light signal is coming from at any moment may be evaluated by measuring the ratio of signal amplitudes from any three units. Tilting the horizontal units at the 30° angle helped reduce the waste of sensitive solid angle on areas below the horizon. It was felt that elevating the horizontal tube directions more than 30° would badly reduce the disparity of signals between units needed for directional information.

Figure 5.2 illustrates the basic design of each detection assembly. A fourteen-inch diameter Dumont K1328 photomultiplier tube is housed within a sheet metal can covered with a window of 1/2" thick ultraviolet transmitting (UVT) Plexiglas. In addition to protecting the tube from the elements and stray light, the housing serves as a mechanical support for the tube and the following accessory items:

(a) A glass filter which is highly absorbing in the visible part of the spectrum where there is an abundance of background light with practically no scintillation emission lines present. The filter transmits almost exclusively in a wavelength region where a large fraction of the fluorescence radiation may be found. The background flux is attenuated by a factor of six whereas the signal is calculated to suffer a reduction by a factor of only 1.65. The overall effect of the filter therefore is to enhance the signal-to-noise ratio by a factor of

Cross Section of
a Phototube Unit

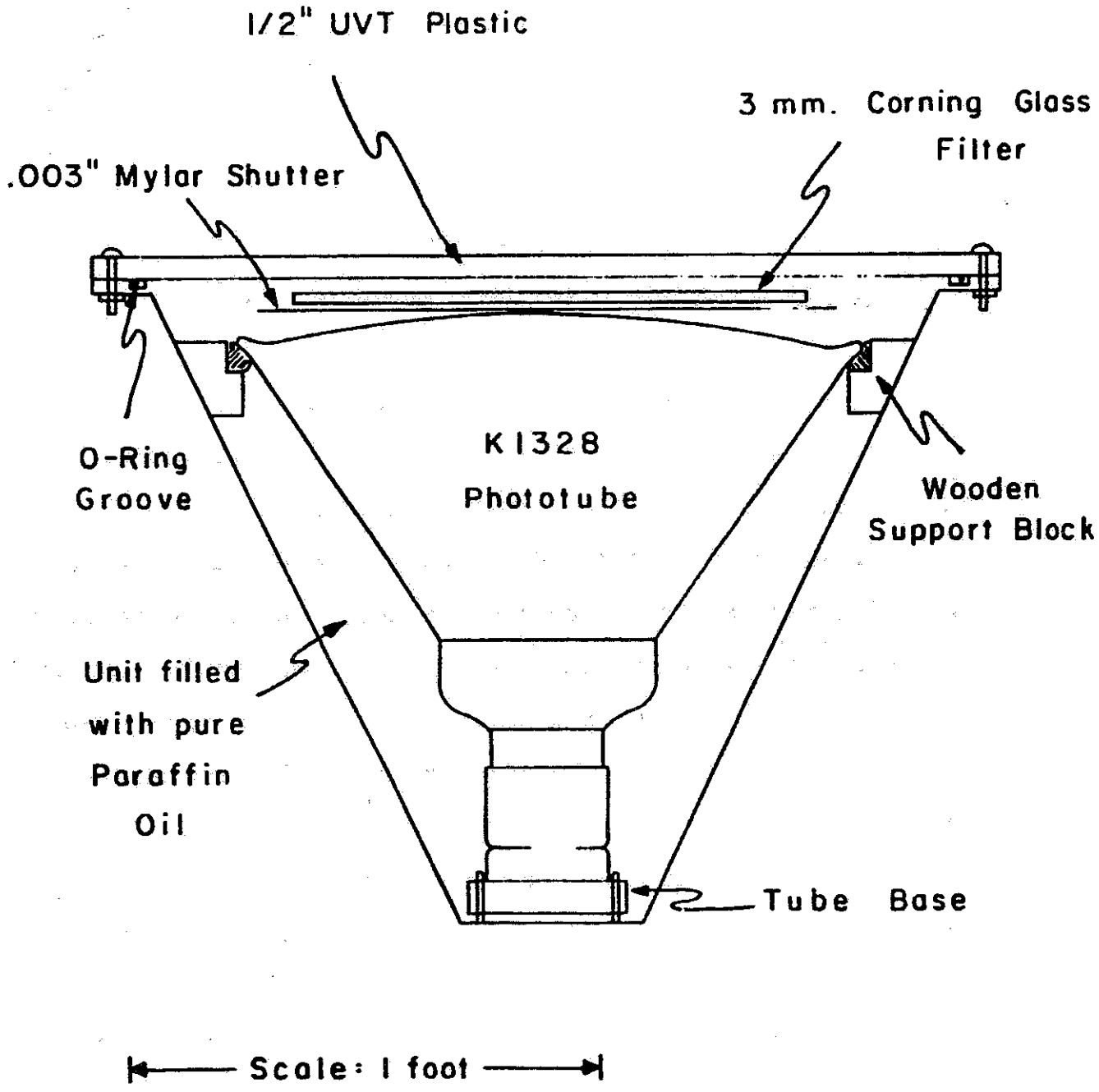

Figure 5.2

$\frac{\sqrt{6}}{1.65} = 1.5.$

(b) A shutter assembly, similar to a window shade, designed to protect the phototube from direct sunlight which, it was felt, could be detrimental to the photocathode surface over long periods of time. The shutter assembly consists of two motor driven rollers (not shown in the diagram) on either side of the tube face between which is strung an opaque plastic sheet fastened to a .003" thick transparent Mylar sheet. During the nighttime observation the clear sheet would be in front of the tube, and at other times the tube would be covered by the opaque sheet.

(c) A tube base assembly which, in addition to having a tube socket with high voltage dropping resistors, contains two transistor emitter follower preamplifiers.

The entire enclosure is filled with mineral oil which optically matches the phototube, filter, and Plexiglas cover. The advantage gained by such matching is substantial for the reception of light having a large angle of incidence. The increase in efficiency of the units by optical matching may have been badly offset by the fact that the mineral oil had a tendency to become discolored and murky, even when precautions were taken to insure everything inside the can was reasonably clean. Experience taught us that when the mineral oil had become discernably dirty to the eye, its transmission in the UV was very poor. Leakage problems and inconvenience in servicing the units also made the advisability of using mineral oil questionable.

Laboratory tests indicated that the gain of a large phototube is somewhat reduced by the presence of a relatively weak magnetic field. This is a consequence of the fact that the low energy photoelectrons may be deflected as they travel the large distance between the photocathode and the first dynode. In an effort to improve the operating efficiency of the five detection units, they were surrounded by square, single turn current carrying loops arranged as Helmholtz coils to cancel, or at least greatly reduce, the geomagnetic field. The effectiveness of the Helmholtz coil assembly was compromised, however, by the unwise choice of galvanized sheet iron for the unit cans which had a fair amount of permanent stray magnetization.

The 0.1 square meter photocathode of the K1328 photomultiplier has an S-11 spectral response. We have estimated that at the wavelength corresponding to maximum sensitivity the photocathode efficiency averaged over the entire photosurface is roughly 11%. This figure is lower than one is accustomed to finding with smaller phototubes and may probably be accounted for by the fact that the large geometry is not well suited for efficient acceleration and collection of photoelectrons. In practice, the overall dynode gain of different phototubes was found to vary considerably--sometimes by a factor of a thousand (at ~1300 volts)! Large differences in gain between the phototubes in a station were compensated for by varying the phototube high voltages and signal amplifier sensitivities thus facilitating a more rapid interpretation of the pulse displays from

different units.

Signal Amplification and Display

In addition to a series of linear (AC coupled) amplifiers, the amplification chain contains a logarithmic amplifier[34] which was included to allow the presentation of pulses over a wide dynamic range. For signal inputs much larger than the night sky noise the output of the logarithmic amplifier is closely proportional to the log of the input voltage, however the response characteristics for smaller voltages more resembles a linear relationship. A detailed survey of the response function for the entire amplifier system will be presented in conjunction with a description of the analysis program for events. After sufficient amplification, the photomultiplier signals for each direction are applied to the vertical deflection plates of five cathode ray tubes mounted in front of a camera for recording events.

Although at first glance it may seem unnecessary, the preservation of negative signal voltages for display is indeed important for the proper analysis of events. Excursions of the noise below the average zero baseline do convey useful information, of a negative character, on the probability of there being a weak signal present. The amplifiers and CRT display permit the registering of negative signal voltages in excess of three or four standard deviations of noise.

During the first months of observation carried out with the first station, we were aware of the existence of a strong

120 cycle AC ripple in the phototube signals produced by scattered light from man-made sources. It was suspected that the chief contribution came from mercury street lighting which was known to produce an abundance of UV light with a strong 120 cycle modulation. In many instances, the amplitude of the ripple exceeded the statistical fluctuation noise by a factor of five or six. Our amplifiers had been designed to accept low frequencies as well as high frequencies to minimize distortion of longer pulses. Although the 120 cycle ripple did not distort or interfere with the actual pulses we were interested in viewing since the time scale was much longer than tens of microseconds, there was much uncertainty in the position of the zero baseline within the short time interval of a CRT sweep during an event. In some cases the zero line was pushed below the negative signal response limits of the amplifiers during certain portions of the 120 cycle phase.

The low frequency ripple was virtually eliminated by installing in the amplifier chain a parallel T network[35] tuned to reject the undesired 120 cycle frequency component. Except for nights where there was a high overcast cloud layer efficiently reflecting city lights, the amplitude of the 120 cycle ripple and its harmonics was appreciably less than one standard deviation of noise after the installation of the filters. The frequency response function of the filter is in the shape of an inverted cusp centered on the rejection frequency. A circuit installed further down the amplifier chain compensated for losses, produced by the 120 cycle filter, occurring at higher

frequencies which made ten or twenty microsecond square pulses slope downwards slightly.

The rise time for the entire amplifier system is approximately 1.5 μs. At the time the amplifier system was being designed, prior to the construction of the first station, it was anticipated that most of the more interesting events would occur from five to fifteen kilometers away. Evaluation of the integrands (of Equation 4.10) at the end of the preceding chapter would have indicated to the contrary however: A majority of the detectable events consists of nearby, low energy showers. In retrospect, therefore, it would have been desirable to have faster amplifiers which would have given more detailed information on showers closer than a few kilometers. With some success efforts were made to speed up the response of certain systems within the amplifiers, but any improvement by a large factor would have been accomplished only with a major remodification of the circuitry, which used transistors and delay lines having a limited frequency cutoff.

Event Pulse Discrimination System

The electronics which trigger the apparatus to photograph the appearance of event pulses on the CRT screen must be sensitive to signals not much larger than the noise which is always present. At the same time the system, which effectively must sample a random noise signal about 10^6 times per second, must be capable of rejecting the many chance noise fluctuations to the point where the frequency of accidentals is reasonably low.

The prime requisite for a low counting rate is simply the economy of film and scanning time necessary for all of the pictures taken. There are a number of discrimination logic features incorporated into the apparatus which allow the detection of almost unreadable event pulses with a low net picture taking rate.

A simple discriminator set to trigger at a voltage level which is a factor of x higher than one standard deviation of a Gaussian noise signal will register extreme voltage excursions at an average rate

$$f = (2\pi)^{-1/2} f_s \int_x^\infty e^{-t^2/2}\, dt \qquad (5.1)$$

where f_s is the sampling rate (which is equivalent to the frequency cutoff of the noise signal). Since $x \gg 1$ for all cases we are interested in, the approximation

$$f = \frac{f_s}{x\sqrt{2\pi}}\ e^{-x^2/2} \qquad (5.2)$$

is valid. For f_s roughly equal to 10^6/sec an average counting rate of one count every thousand seconds would be obtained if the discriminator were set at an x value of six. The acceptance of a discriminator pulse from any of the five channels would mean that a picture would be taken once every two hundred seconds. The performance of the entire discrimination system could be improved, of course, by requiring the coincidence of two channels to determine at which time a picture should be taken.

If the coincidence electronics is set to fire on the overlap of any two pulses of length τ coming from the five channels, the net triggering rate would be

$$f_c = C_{5,2} \frac{\tau f_s^2}{\pi x^2} e^{-x^2} \qquad (5.3)$$

since $f_c = 2\tau f^2$ for any pair of channels, and $C_{5,2}$ (which equals ten) is the binomial coefficient representing the number of pairs capable of providing a coincidence. Therefore, if $\tau = 15$ μs, the counting rate for discriminators set at $x = 4$ would be one count every three seconds, and if $x = 5$ the rate would be slightly less than one count every ten hours. A reasonable picture taking rate would thus occur at some setting between four and five standard deviations of noise.

Further improvement in triggering sensitivity may be accomplished if, instead of monitoring the actual phototube signal voltage itself, the discriminator for each channel sees an integral of the signal over a period of time comparable to the average length of an event pulse. For instance, electronically integrating over 10 μs time intervals the mixture of some noise and a 10 μs square pulse improves the signal-to-noise ratio by a factor of $10^{1/2}$ if the pulse and noise originally had a frequency cut-off at one megacycle. The integration, in effect, increases the signal amplitude by a factor of 10 whereas the noise only increases by $10^{1/2}$.

For our experiment the integration is accomplished by passing the signal, at some intermediate stage of amplification, through a delay line which has a series of high impedance taps

at regular intervals. The signals from these taps are mixed and amplified (see Figure 5.3a) with the resulting output representing an integration interval of fixed length which advances continuously in time along the original phototube signal.

The taps which sample the signal along the delay line are spaced at intervals of 0.8 μs--slightly shorter than the minimum signal rise time of approximately 1 μs at the particular stage of amplification in question. As shown in Figure 5.3a, however, the mixed signals are split into two groups with an intervening gap of 1.6 μs. The purpose behind this division will be discussed shortly. The box labeled "add" has an output which represents an integration over 8 μs with the exclusion of the 1.6 μs gap in the middle. An additional 6 μs of delay line after the last tap serves to delay the signal for a time duration sufficient to insure, in most cases, that the entire signal appears on the CRT vertical plates after the sweep has been initiated.

In actuality the noise appearing on the signal channels is not truly Gaussian. With reasonable frequency additional large pulse spikes appear which, as an experiment measuring counting rate versus discrimination level has verified, raise the tail of the Gaussian noise spectrum in the region representing large positive signal excursions. These extra pulses may be attributable to Čerenkov light generated in the atmosphere[6] or in the glass, oil and plastic in front of the photocathode by small cosmic ray showers, or their source may

Circuit Diagrams for Recorder Trigger Logic

A. For each photomultiplier

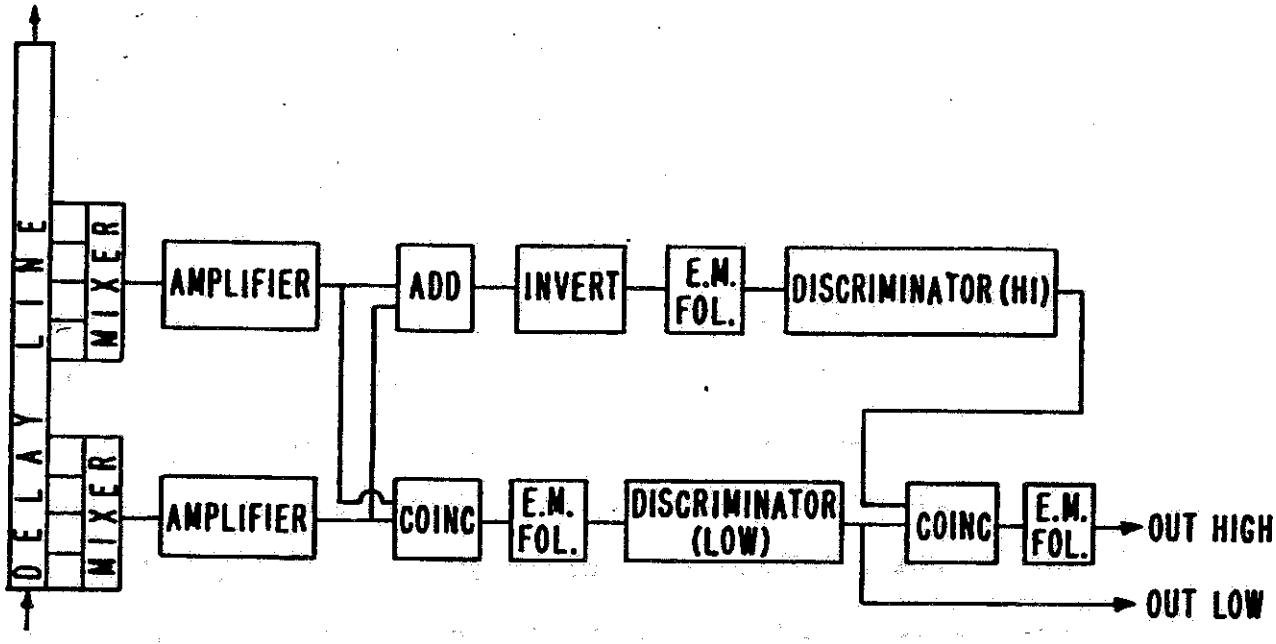

B. For all tubes

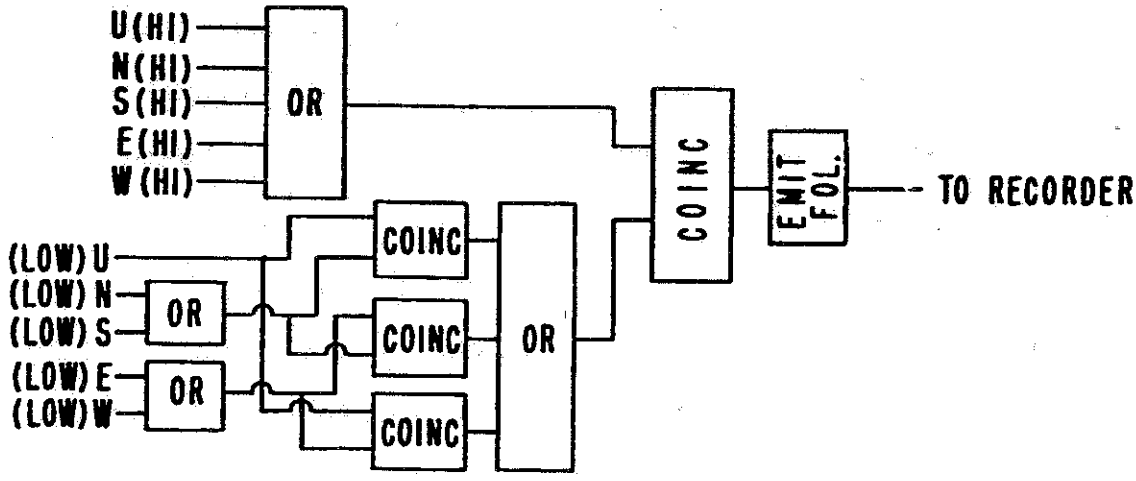

Figure 5.3

be from spurious electrical disturbances. In either case, the pulses are very likely to appear in more than one channel at any particular time, and some precautions are necessary to prevent many useless picture frames from being taken.

A pulse appearing as a delta function (i.e. whose length is much less than 1 μs) at the input of the signal amplifier system would travel along the delay line as a pulse of 1 μs length. Since this length is shorter than the 1.6 μs gap, the box labeled "coinc", which is designed to produce an output voltage proportional to the smaller of the two mixer outputs, fails to see a significant voltage from the two blocks simultaneously. Interesting pulses whose duration would be somewhat longer than the amplifier rise time, on the other hand, would span the gap and produce a noticeable output from the coincidence.

As an examination of Figure 5.3 will show, any signal whose amplitude after 1.6 μs compares favorably with 3.2 μs of noise will fire the "low" discriminator and produce a "low" output pulse. If, in addition, the signal pulse is large compared to the noise over the 8 μs time scale, a "high" output pulse is obtained.

As an additional refinement to the coincidence logic sampling discriminator pulses from the different channels, restrictions may be imposed with regard to specific types of discriminator output combinations allowed. For instance, a coincidence coming only from two opposed phototube units (i.e. north and south or east and west) without a discriminator

signal from another channel would not likely signify a true event. Although the circuitry in Figure 5.3b may at first seem complicated, its function is merely to respond to a "high" pulse from one channel and a "low" pulse from a channel representing an adjacent phototube. That is, to trigger the apparatus we require a significantly large pulse to be seen by one phototube simultaneously with a promising wiggle from any neighboring unit. In practice the "low" discriminator for each channel is set to give a higher accidental count rate than the "high" discriminator.

Although Equation (5.3) does not accurately apply to the actual logic system in use, it nonetheless demonstrates that the net counting rate depends very sensitively on the value of x, and hence slight variations in the night sky background level produce wide excursions in counting rate. This behavior poses a practical difficulty which has been encountered in the course of station operations since changes in the local weather produce significant fluctuations in the background flux. Fortunately, however, the design of the discrimination system is such that the ability of the electronics, while maintaining a reasonably low frequency of accidentals, to sense a weak event exceeds by a comfortable margin the ability for one to intelligently interpret said event in the noise present. That is, we may feel confident that if the discriminators are set such that a dozen or so pictures are taken during one evening, anything worth seeing will be recorded without difficulty. At the beginning

of an evening's run, therefore, it is permissible for one to set the discriminator levels conservatively high to allow for a possible brightening of the sky which could occur later at night and thus avoid the risk of a greatly increased counting rate which essentially saturates the recording system. We do have, however, an automatic high voltage cutout device which acts in the event the triggering rate becomes excessive.

Recognition and Suppression of Interference

In addition to the five separate phototube signal amplification and display systems, a sixth channel, electronically identical to the others, was incorporated into the experiment to serve as a dummy. This spare channel has proven exceedingly useful in signalizing events triggered by noise generated from within the apparatus itself. In addition, the absence of any disturbance recorded on the spare CRT has given us more confidence in the legitimacy of pulses we thought could be air showers. Care was taken to insure that the spare system was coupled to possible sources of noise as well as or better than the operational systems. For example, it was felt that simple capacitive coupling of the high voltage output to the front end of the first preamplifier would not adequately duplicate the sensitivity of the photomultiplier channels to voltage fluctuations from the high voltage power supply. A photomultiplier tube watching a steady source of light may be expected to act as an amplifier to small disturbances in the high voltage since the collective gain of the dynodes is very steeply dependent on

the value of the voltage. One therefore needs either additional amplification or an actual photomultiplier (having a photocurrent comparable to the other photomultipliers) connected in the usual manner to the first preamplifier.

The spare channel also served the purpose of combating a rather troublesome form of interference which was found to occasionally occur within the local area. High intensity stroboscopic approach lights (pulsed at regular, two second intervals) in use at an airport roughly five miles distant from one of the stations registered exceptionally large signal pulses with our apparatus, even though the airport was not directly visible from the station and the lights were directed 180° away from the station. The apparatus was sufficiently sensitive to readily detect the light back-scattered in the atmosphere. Although the lights were normally operated only during inclement weather conditions, from time to time they were in use during good observing nights. We therefore found it desirable to put the spare channel's phototube (a 5" diameter tube with a collimating cylinder attached) to use as a detector of the airport light with the intention of providing a signal to suppress the faulty recognition of the strobe signal by the logic circuitry as an event. Specifically, the signal from the phototube which monitored a small area of sky in the direction of the airport was fed to a discriminator which, in turn, relayed an anti-coincidence pulse to the picture-taking triggering logic. The triggering logic was thus deactivated for each short time interval corresponding to the reception of a spurious strobe

light signal. Since the spare channel was also sensitive to electrical transients within the apparatus, many of the larger unwanted disturbances were likewise vetoed.

Interference from lightning was found to be particularly troublesome during the summer months in the Ithaca area. As one would expect, lightning discharges produce a rich abundance of UV radiation within the spectral passband of our apparatus. Indeed the spectral character of the discharges should exhibit a predominance of nitrogen band emissions which, of course, the apparatus has been specifically designed to register. Quite distant storm activity, producing flashes near the horizon barely detectable to a dark-adapted human eye, provides enough interference to force us to discontinue observations (or suffer a considerable wastage of photographic film!). Much otherwise useful running time has been lost by the presence of far off thunderstorm activity. This would suggest the importance of ascertaining thunderstorm frequency in addition to the relative amount of cloud coverage for various localities in any future program of site selection for an optical air shower experiment.

The chances for misinterpreting a pulse generated by lightning seems remote. Lightning usually produces a rapid succession of large pulses, each lasting a millisecond or more, which are easily recognizable. One might envision the existence of occasional, weak, rapid discharges which could possibly have durations comparable to air shower events, but it would be highly unlikely that such discharges could simulate the linear

progression of a light source proceeding in a highly regular manner across the sky.

Additional Features

During the course of an evening's operation, sizable variations in phototube gains were noticed to occur. These fluctuations in sensitivity seemed for the most part to be caused by the sudden application of the high voltage to the phototubes at the beginning of a run. The time needed for the tubes to reach an equilibrium level of gain was typically an hour or so (the changes were not due to a warm up drift in the high voltage power supply since the supply was left running continuously--day and night). In addition to the short term variations considerable changes in average gain for the phototubes were observed over periods of weeks. At the time an event occurs even a small uncertainty in the relative gain of the phototubes, that is to say the gain of each tube as compared with the other four, cannot be tolerated since the outcome of the directional analysis depends on an accurate comparison of light fluxes arriving at each phototube unit. The proportional amount of error in the relative gains should be roughly less than the reciprocal of an event's Q value, if full advantage of the analysis technique's ability to minimize directional uncertainties is to be realized. A knowledge of the gains in terms of some absolute standard, however, need not be established with much precision since such information relates

only to the measurement of the overall intensity of the received light signal from the shower.

To keep track of the gains two neon calibration lamps were mounted on the ends of rods positioned near the five phototube units. The placement of the lamps was chosen such that each lamp would illuminate three units equally. Each horizontal unit was exposed to a single lamp while the vertically facing unit was illuminated by both lamps. These lamps, incidentally, are not shown in the photograph of the tube units (Figure 5.1) which unfortunately was taken before the installation of the calibration system. Shortly after the completion of the CRT trace for an event, the calibration lamps would turn on for several hundred microseconds while a second sweep was initiated to give a calibration reference line superimposed on the photographic record. The appearance of the calibration sweeps is shown in Figure 5.5 (in the form of wiggly lines above the pulses). As one would expect, the calibration traces show some noise arising from statistical fluctuations. The electronics which pulse the neon lamps carefully regulate the current flow to each lamp and experience has shown that the lamps reliably generate reproducible quantities of light.

A third CRT sweep is made with the amplifiers fully saturated in a negative direction to provide a baseline reference against which to measure the pulse heights in the film record. These baselines also contain time marker pips generated every eight microseconds by a single time reference

pulse generator whose signal is fed to each channel at an amplifier stage which comes before the storage pulse line. The suppressed baselines and the time markers may also be seen in Figure 5.5 (page 73).

Some thought had been devoted to the possibility of including an additional refinement to an observing station. It was suggested that a device capable of recording the sizes and positions of clouds would have been a desirable feature to have available in the event that a signal was interrupted by the momentary passage of the shower behind a cloud bank or some small cloud structures. It would be useful to have a means, based on a simultaneous recording of the cloud conditions, for explaining interrupted or irregular pulses. One method of accomplishing the cloud recognition would be to have an all-sky camera photograph the star field. A lack of time prevented us from pursuing the idea seriously--such a system was not incorporated into the station setup.

Detection Capability of the Pilot Experiment

It is of interest to state briefly conclusions based on results from Chapter IV which are applicable to the pilot experiment. Substituting $N = 7 \times 10^{-10} E$, $Y = 1$ photon/m, $A = 0.1\ m^2$, $c = 300$ m/μs and $\varepsilon_s = 0.06$ into Equation (4.1) gives a simplified expression for the typical number of photoelectrons per microsecond to be produced in a phototube directly facing the shower:

$$S = \frac{10^{-16}\, E(ev)}{\left(r_o(km)\right)^2} \qquad (5.4)$$

As an example, a 10^{20} ev event at 10 km would produce a signal strength representative of 100 photoelectrons/μs.

On a clear, dark night a shower signal must compete with a background noise equivalent to approximately 30 photoelectrons per microsecond. The latter quantity was computed from the following expression

$$n = \left[(.1\ m^2) \int_o^\infty \varepsilon(\lambda) I_b(\lambda) d\lambda \int_o^{\pi/2} 2\pi \cos^p\theta \sin\theta d\theta \right]^{1/2} \qquad (5.5)$$

where $\varepsilon(\lambda)$ is the product of the phototube efficiency and the filter transmission, both being a function of wavelength. $I_b(\lambda)$ is the background intensity expressed in terms of photons $\text{Å}^{-1}\mu s^{-1}\ str^{-1} m^{-2}$. The integral over wavelength, which was evaluated numerically, represents the net sensitivity to background light at normal incidence, and the θ integral represents an integration over solid angle. The expression $\cos^p\theta$ is the phototube unit's angular response function, which will be described in Chapter VIII. Experimental measurements of the noise in the phototube amplifier channels give satisfactory agreement with the calculated value.

Figure 5.4 gives, in diagrammatical form, an overall perspective of the relationships between variables of principal interest. All of the variables are plotted logarithmically with a change of one decade being represented by a line.

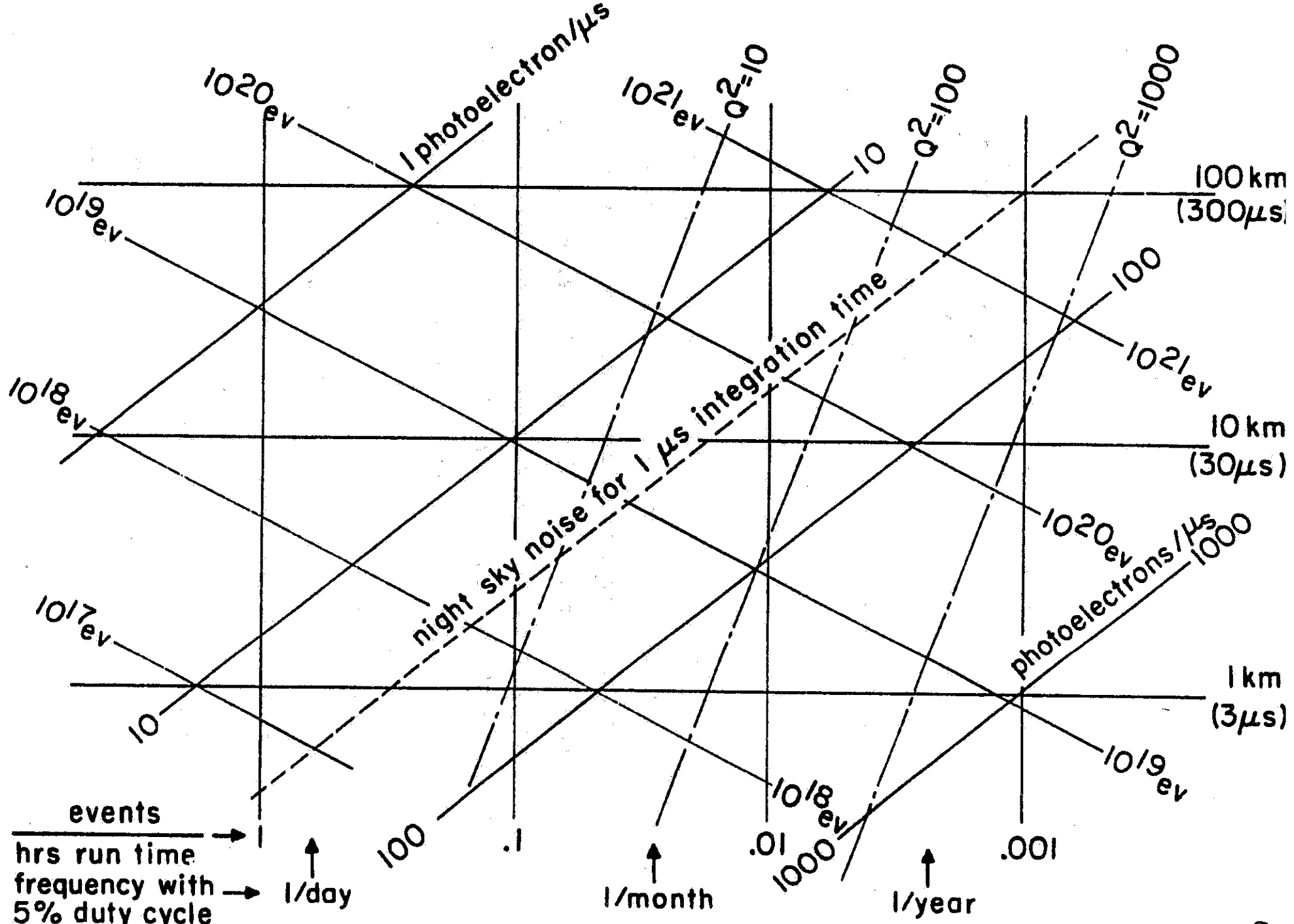

Figure 5-4 A logarithmic plot of E, r, and frequency for the plotted

Solutions for any of the three variables S, E, or r_o found in Equation (5.4) may be ascertained by locating the intersection of lines representing two known variables. For the example quoted in the text immediately following Equation (5.4) we see that the intersection of 10^{20} ev and 10 km lies on the 100 photoelectrons/μs line. Furthermore we may quickly recognize that the 10^{20} ev event at 10 km should give a pulse approximately 30 μs long whose amplitude is larger than one standard deviation of noise by roughly a factor of three (for an amplifier having a frequency cut-off around one megacycle). The square of the event quality Q would therefore be about 300.

Let us next turn our attention to the event frequency relationship expressed along the horizontal scale of the diagram. Assuming the integral energy spectrum shown in Figure 1.1 to be correct, we may assign an expectation for the frequency of events whose energy exceeds a given energy and whose closest approach falls within some specified radius. Such a frequency, equal to $2\pi^2 r_o^2 I(>E)$, is an approximate indication of the frequency of events we are certain will give better signals than an event of energy E and (closest approach) distance r_o. Returning to our previous example we note that we should expect events whose energy exceeds 10^{20} ev to hit within 10 km of a station roughly three times every thousand hours. For the reasons discussed in Chapter IV we would, of course, expect the frequency's proportionality to r_o^2 to become invalid under practical circumstances for r_o not

satisfying the restrictions 1 km $\lesssim r_o \lesssim$ 15 km. For convenience, the equivalence relations (4.11 a,b,c) are shown for a 5% run-time efficiency.

It should be stressed that Figure 5.4 is only designed to demonstrate the interrelation of different variables and to give the reader a quick reference with respect to orders of magnitude. The values shown for the quantities, particularly the frequency, are based on crude approximations.

Results from the Pilot Experiment

Over the three year period during which one or both detection stations were in operation we were able to accumulate a combined total of approximately one thousand hours of observing time. Included in this running time estimate are nights when the sky was partially obstructed by clouds or when the horizontal visibility was limited. For such occasions an estimation of the reduction in coverage of the apparatus was made, and the actual operation time was accordingly revised downwards to give an equivalent "effective running time". The choice of a value for the fractional number as a multiplier for the running time accumulated during unfavorable but nonetheless useful conditions is subject to large error in view of the fact that it is assigned on the basis of crude observations of visual conditions during the early evening and following morning. Nonetheless the consequences of the errors in the running time estimates are not relatively serious since our final conclusions

must be based on results having a large statistical uncertainty.

As a matter of interest, the overall duty factor was computed to be 3.94%, which is not far from the estimate of 5% quoted earlier. A 5% run time efficiency might have been attained if equipment breakdowns had been less frequent.

Out of approximately 110,000 pictures which were inspected over the three year period a small fraction of the frames could be classified according to the following categories:

(A) Pictures containing recognizable pulses whose origin may not be traced to some trivial spurious disturbances (such as lightning, electrical transients, etc.). Total number: 263

(B) Pictures judged as having a remote possibility that they may have resulted from cosmic rays. Total number: 124

(C) Pictures having pulses which strongly suggest the presence of an air shower, but which have too poor a signal-to-noise ratio to obtain intelligent results from the analysis program. Total number: 28

(D) Signals belonging to category (C) which have a high enough S/n ratio to seem worthy of analysis but which, after careful preliminary inspection or after execution of the analysis, lack some of the basic requirements of self-consistency or intelligibility. Total number: 10

(E) Events whose analyses give a favorable indication of credibility and yield some crude information on the shower parameters. Total number: 0

Events classified in a given category are included in the total for the number of events in the categories of lower merit.

In scanning for events belonging to category (C) (or better) one looks for pulses which appear in at least three channels and which show some variation in shape or time of onset, suggesting a movement of the light source. The pulse shapes should have an appearance not differing too markedly from the simulated pulses obtained from the computer program described in Chapter XII. For showers suspected of not being too far from the zenith the pulse height in up channel should be representative of a signal roughly twice as large as the pulses received from horizontal photomultiplier units.

From the lack of events within category (E) we may infer that no showers having $Q \gtrsim 30$ were observed in the thousand hours of running. According to the results given in Table 4.1 (for A = 0.1 m, Ω = 3.0 str) we should expect to have seen roughly three events if the presently accepted version of the energy spectrum shown in Figure 1.1 were correct. The absence of such data suggests that either our estimation of detection efficiency has been markedly optimistic, which we feel is unlikely, or that the true cosmic ray flux is certainly not higher than current estimates for showers having energies in excess of approximately one joule. Because of the uncertainties involved (both experimental and statistical) we feel hesitant to conclusively assert that the high energy spectrum is significantly in error (i.e., that it is an overestimate of the true spectrum).

It is more difficult to draw conclusions from the

Sketch of One Event as Recorded on Film

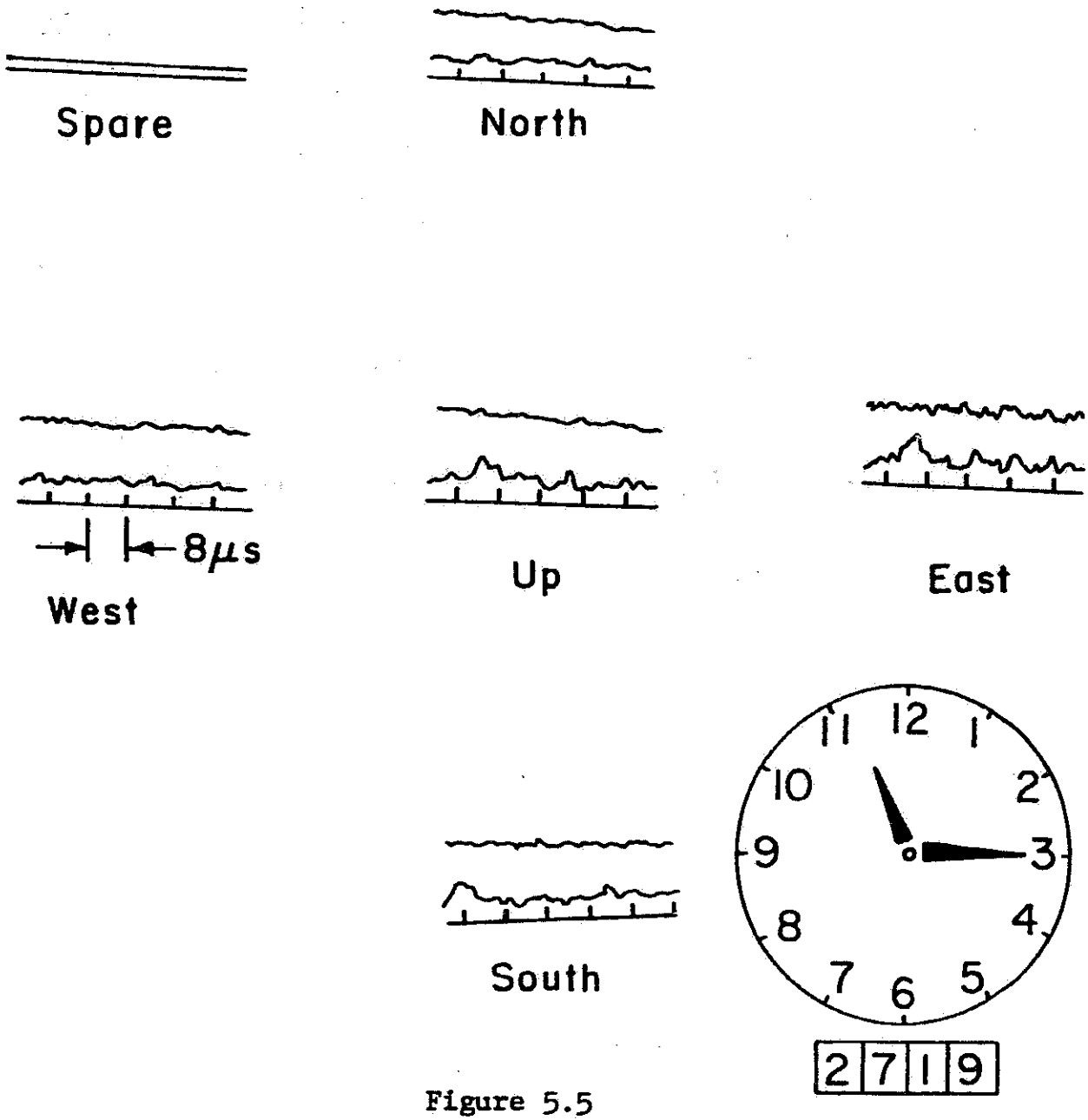

Figure 5.5

counting rate of pulses lacking positive identification in categories (C) or (D). The frequency of the occurrence of such marginal events agrees reasonably well with the expectation of events having a Q value greater than about ten. The tabulation of the number of events in categories (A) and (B) reveals no information of scientific significance outside of giving an indication of a background level for barely detectable pulses, generated by either air showers or other sources, which the apparatus was capable of recording. The authenticity of many of the more marginal events is subject to question since during the three months of running two stations alongside (both were in simultaneous operation for roughly 30 hours) no coincident pulses were seen--except for sharp spikes representative of Cerenkov light from small showers.

VI. INTRODUCTORY REMARKS ON DATA INTERPRETATION

In attempting to analyze the recording of a suspected event, it is first necessary to determine the direction of the shower axis and its position relative to the observing station. Not only is this information of interest in determining the possible origin of the primary particle, but it is essential to know the geometry of the event to gain information about the shower size and growth from the observed light intensity versus time. As discussed earlier, the scintillation light from an air shower would appear as a diffuse patch of illumination moving in a straight line at the velocity of light toward the earth.

Under ideal circumstances (accurately measured signals with no noise) one could determine the shower's geometrical parameters using only three separate measurements of direction at different times. The line joining the directions would define a plane on which lies the shower axis and the observing station. The position of the axis on this plane is determined by studying the angular separation of the observed directions with respect to time. A minimum of three measurements are necessary since one must determine both the apparent angular velocity and angular acceleration of the light source.

For simplicity in discussing the time dependence of the observed angle of incoming light along the plane joining the shower axis and the observer, we shall for the moment abandon

any reference to a specific fixed coordinate system and disregard spatial limitations imposed by the earth and the limited height of the atmosphere. Let us consider the idealized example of a source of light moving at velocity c past the observer from minus infinity to plus infinity with an "impact parameter" (distance of closest approach to the observer) r_o. The angle θ as shown in Figure 6.1 would progress from $-\frac{\pi}{2}$ to $+\frac{\pi}{2}$ during the entire history of the event.

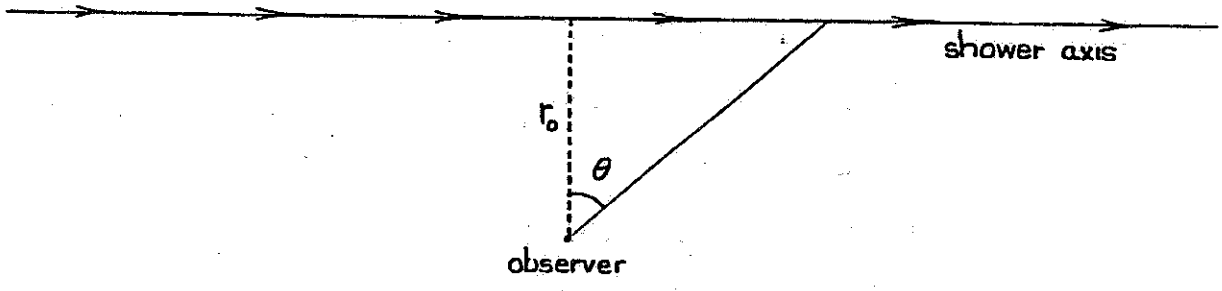

Figure 6.1

If we define t to be the time of reception of light in the direction specified by θ and t_o to be the time that the observer sees the light coming from the point of closest approach then

$$t - t_o = \frac{r_o}{c} (\tan\theta + \sec\theta - 1) \qquad (6.1)$$

The $\tan\theta$ term represents the time the light is emitted from a given point, and the $\sec\theta$ term may be ascribed to the transit time of the light signal to the observer. It should be emphasized, of course, that in this illustrative, hypothetical situation we are assuming that r_o and the origin for θ are

known. Needless to say, in practice our efforts will be directed toward the determination of the latter parameters.

For the observer the entire history of the event before closest approach is compressed into a time equal to r_o/c. As the angle θ increases the apparent angular velocity gradually decreases. Differentiating the preceding formula one finds

$$\frac{d\theta}{dt} = \frac{c}{r_o} (1 - \sin\theta) \tag{6.2}$$

A plot of θ and $\frac{d\theta}{dt}$ against time is shown in Figure 6.2.

Neglecting complications introduced by atmospheric absorption for distant showers or additional contributions from Čerenkov light produced by nearby showers, the strength of the light flux received by the observer would follow the relation

$$F = \frac{NY}{4\pi r^2} \frac{ds}{dt} \tag{6.3}$$

where r, which equals $r_o \sec\theta$, is the instantaneous distance to the shower. The quantity $\frac{ds}{dt}$ is the <u>apparent</u> velocity (given by the distance which appears to have been traveled within a given time interval recorded by the observer) of the shower front and is found by evaluating the differential

$$\frac{ds}{dt} = \frac{d(r_o \tan\theta)}{dt} = r_o \sec^2\theta \frac{d\theta}{dt} \tag{6.4}$$

Equation (6.3) reduces to

$$F = \frac{NY}{4\pi r_o} \frac{d\theta}{dt} \tag{6.5}$$

or, upon substituting Equation (6.2) for $\frac{d\theta}{dt}$,

$$F = \frac{NYc(1 - \sin\theta)}{4\pi r_o^2} \tag{6.6}$$

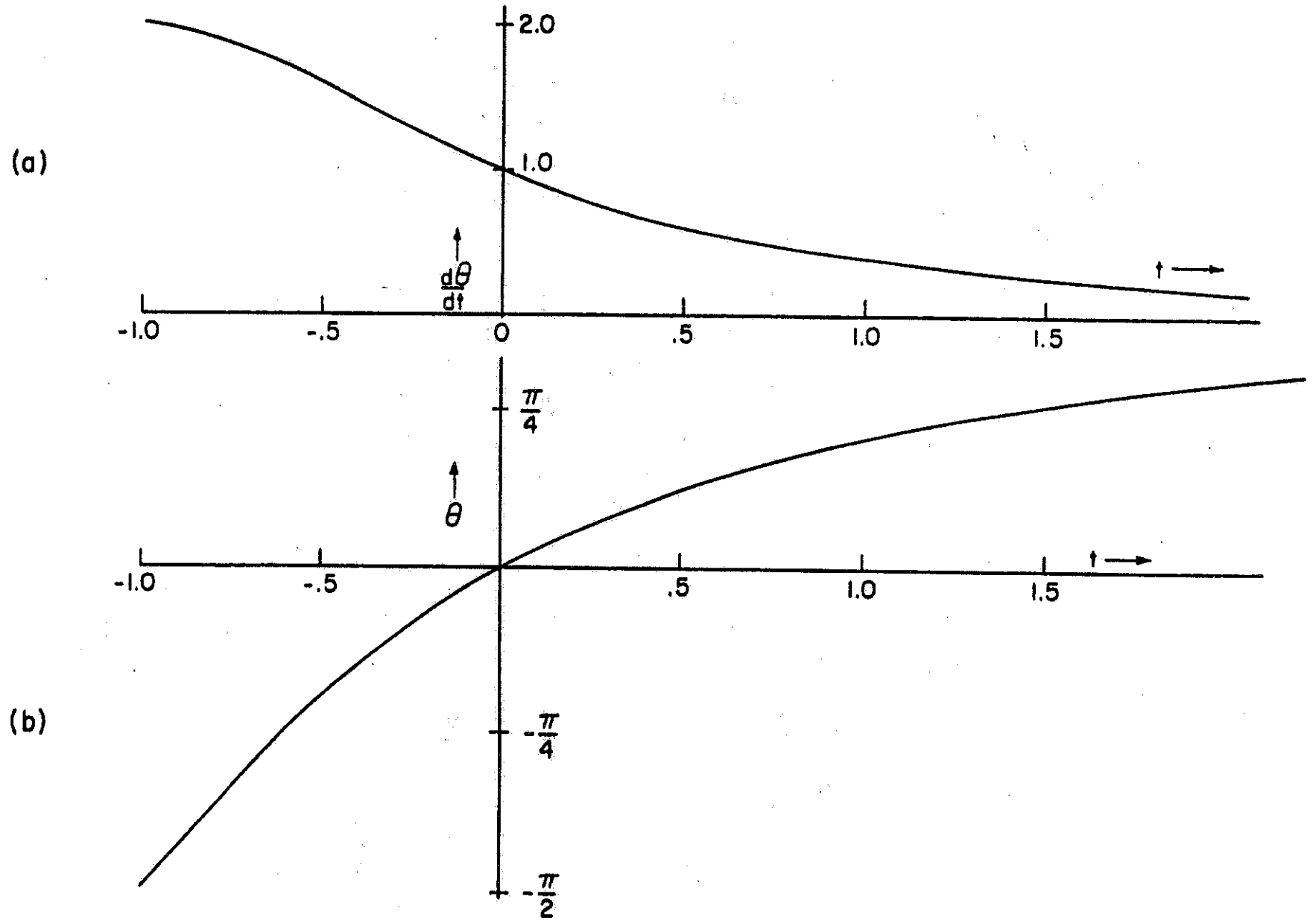

Figure 6.2 Observed (a) angular velocity and (b) angle of a shower as a function of time (expressed in units of r_o/c).

If NY were constant, then, the received intensity of light as a function of time would appear like the graph of $\frac{d\theta}{dt}$ vs. time, shown in Figure 6.2a.

Returning to the context of an actual cosmic ray air shower whose observable angular extent is usually quite limited, it is evident that for most events only a small portion of the curve shown in Figure 6.2b would be visible. Inspection of the curve should enable one to realize that the measurements must be reasonably accurate to give a good estimation of the direction and distance of closest approach since the curve does not have a rapid change of character for different t. For instance, there might be some difficulty in distinguishing a distant approaching shower from a receding shower that is near the observer if there is some uncertainty in the measurements. One must effectively be capable of accurately determining $\frac{d^2\theta}{dt^2}$ in addition to $\frac{d\theta}{dt}$ within some limited time duration.

We may define the orientation of the shower axis on the plane in terms of an angle θ_o which is shown with the other geometrical features in Figure 6.3.* We have seen that both θ_o and r_o are difficult to measure accurately; however, Equation (6.5) demonstrates that the functional dependence of NY as the event progresses is much easier to ascertain, outside of a constant factor whose error is proportional to the error

*The meaning associated with the orthogonal vector and θ_m shown in the figure will be discussed at the beginning of Chapter X.

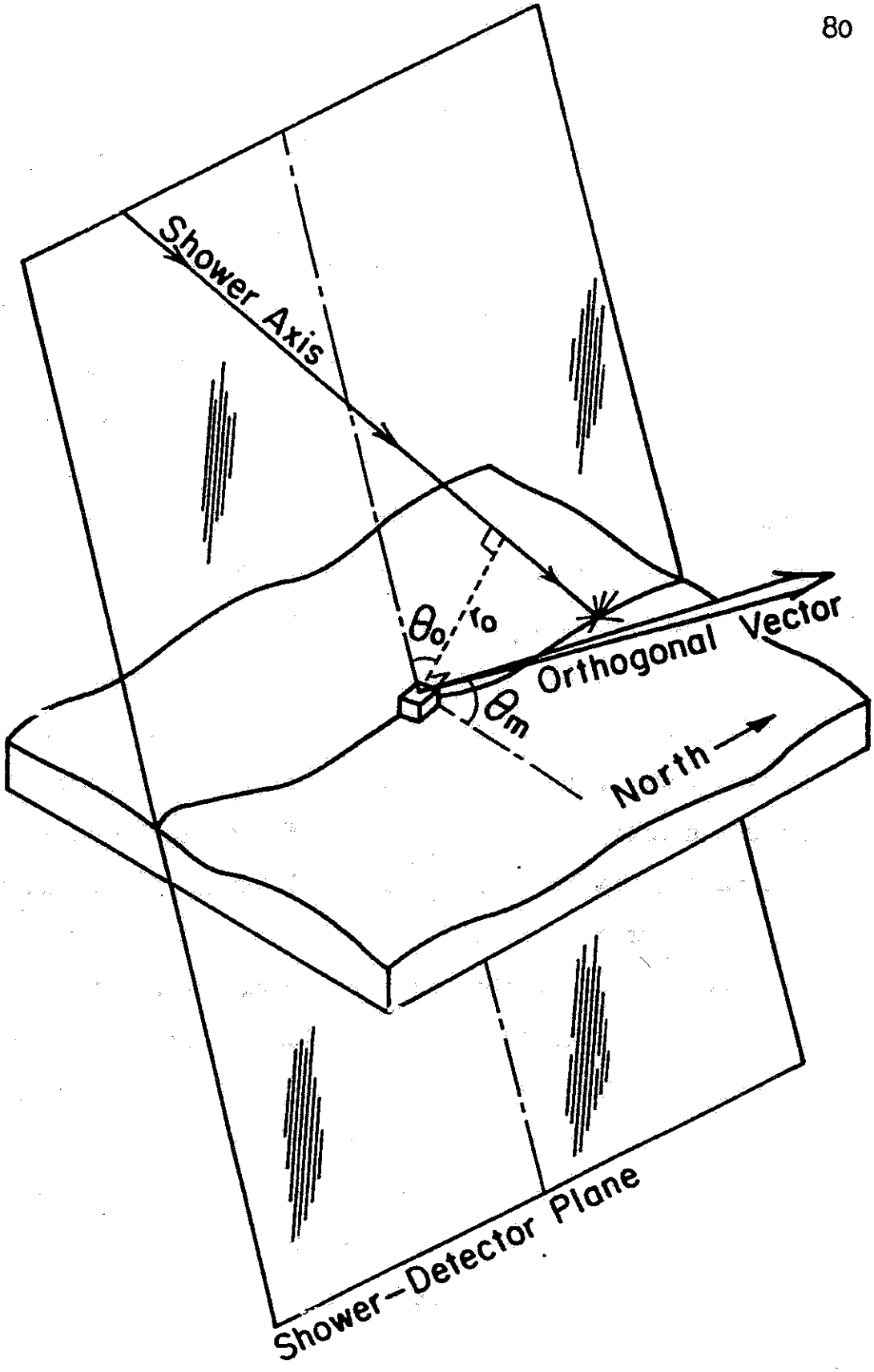
Shower Axis
θ_o
r_o
Orthogonal Vector
θ_m
North
Shower–Detector Plane

Figure 6.3

of r_o. Since $\frac{d\theta}{dt}$ and F are determined with some ease, the relative amount of shower growth and decay could be monitored with good precision in spite of our poor knowledge of the values for θ_o and r_o.

In the perspective of whatever conclusions might be drawn from an experiment it may be claimed that errors in measuring a peak value for N, which allows one to estimate the primary's energy E, are not of a serious consequence since one is essentially interested in establishing a cosmic ray energy spectrum which may extend over several orders of magnitude in energy. On the other hand, errors in θ_o, in addition to confusing the arrival direction of the primary, reflect seriously on any attempts to establish the depth within the atmosphere to which the shower has penetrated at various stages of growth. The knowledge of the latter relationship is useful in confirming any theoretical predictions on the nature of high energy interactions or processes which contribute to the shower development.

In the analysis of the five scope traces of a suspected event, we must concern ourselves with gathering as much information as possible from signals with low signal to noise ratio. With a reasonable number of independent readings along the pulses, however, the shower's geometrical parameters are overdetermined. Any directional measurements exceeding the minimum of three as the shower progresses help to confine the uncertainty of the shower's direction within narrower limits.

Each successive reading may, in itself, be overdetermined since a large portion of the sky is seen by more than three phototubes. It is to our advantage, therefore, to combine all of the measurements, together with our knowledge of anticipated errors, into an ensemble which would yield a joint probability function for each shower parameter. There are a total of five such parameters associated with an event observation which must be determined to describe the shower trajectory geometry: Two parameters--the direction coordinates of an orthogonal vector--describe the plane of the shower line and the observer; the remaining three are t_o, θ_o, and r_o.

Ideally, then, a five dimensional probability function should be determined on the basis of each measurement treated independently. Such an evaluation, however, would involve a prohibitive amount of computation. If we divided each dimension into n possible values between expected extremes, for instance, we would have to make n^5 computations each assessing the probability that a particular combination of parameter values could yield the signals (of the entire event) recorded. In addition, for each computation one would have to allow for a wide variety of observed light intensity versus time functions which possibly could have been representative of the true flux hitting the apparatus during the history of the shower.

The complexity of the rigorous approach just outlined forces us to compromise by dividing the analysis into separate stages, each considering only a few of the above parameters at a time. This approach may be justified only if we are

reasonably confident that the errors in one group of parameters are uncorrelated with the errors in the remaining parameters. Otherwise the answers obtained at one stage of the analysis may depend sensitively on the values assumed from the other. The schematic illustrations depicted in Figure 6.4 may help to clarify this point. Each successive reading of the five photomultiplier signals may be translated into an approximate direction in the sky that the light came from at any instant. The ellipses in the diagrams represent hypothetical examples of equal probability contours which enclose the regions of uncertainty in source directions. The two cases shown each have two nearly coinciding lines of good fit. The dots on each line represent the most probable angular positions for various times as the shower progresses (corresponding dots are connected by dotted lines). As in the actual analysis scheme which will be described later, we first find a line of best fit through the distributions, and later we study the angle versus time sequence along the line. The results of the time dependent study (i.e. the spacing between the dots) in Figure 6.4a are relatively insensitive to the choice of the best fit line, whereas the time dependence is markedly changed in Figure 6.4b for slight changes in position of the line. It will be evident later, when the analyses of computer simulated events produce diagrams resembling Figure 6.4a in character, rather than 6.4b, that the time dependence is relatively independent of the shower plane determination.

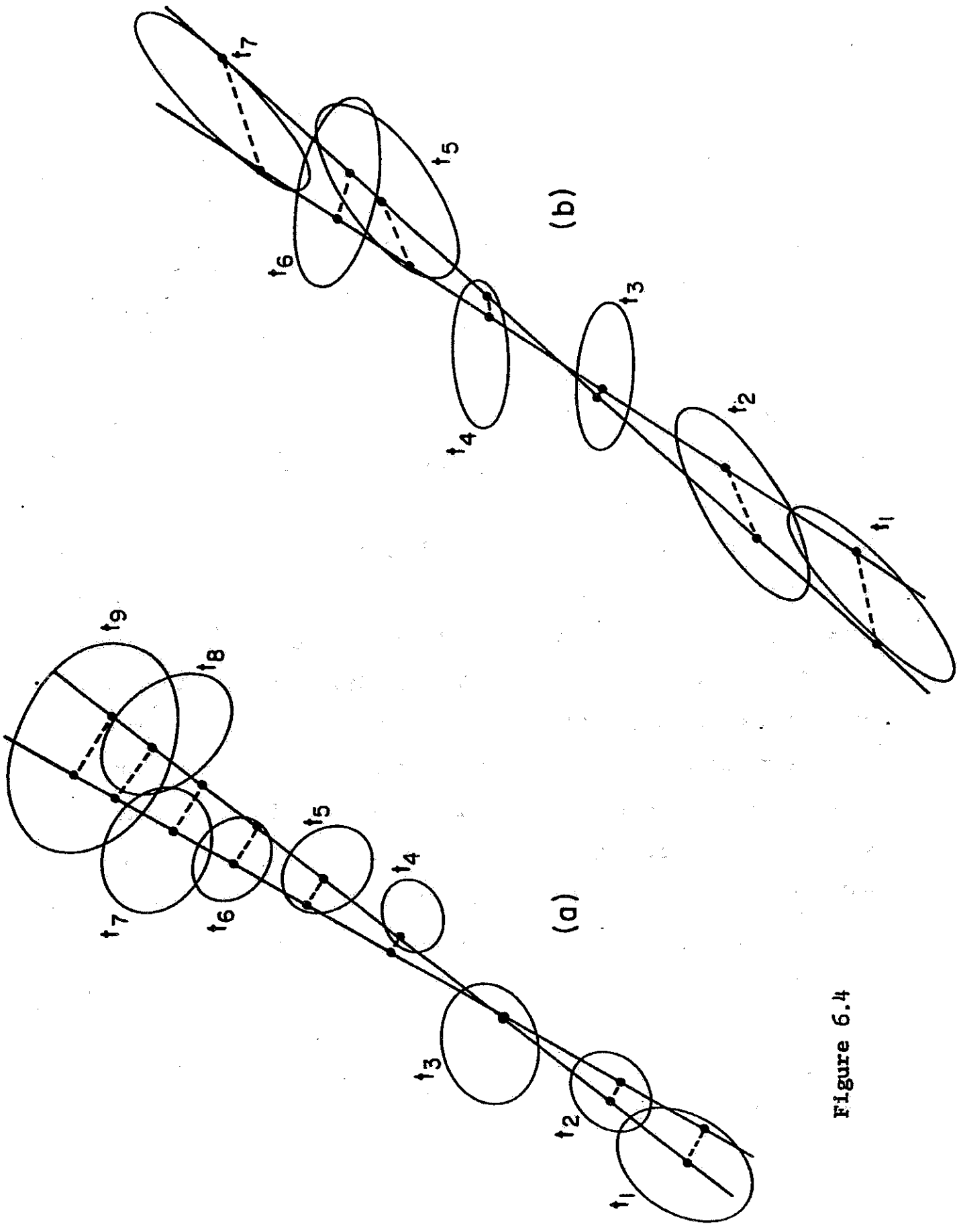

Figure 6.4

The next several chapters will be devoted to the considerations dealing with and the actual mechanics of the shower analysis techniques used for this experiment. Due to the mathematical complexity associated with the integrations and many transformations necessary for a careful interpretation of the data, it was felt desirable to devise a computer program to execute the operations. The program was designed to interpret raw data in the form of cathode ray scope deflections and in the end present an output assigning relative probabilities for various shower parameter combinations. The basic computational procedures used by the computer will be outlined, although no attempt will be made to describe the detailed program logic.

VII. AMPLIFIER RESPONSE FUNCTIONS

The value of the photomultiplier anode current at any instant is derived from the cathode ray trace deflection by means of an empirically derived conversion function based on the amplification characteristics of the entire amplifier system. Since the amplifier system employs a logarithmic amplifier for one of its stages, it was considered desirable to express the signal voltage in terms of the exponential of a polynomial in the variable x, which is the scope deflection above a negatively suppressed baseline:

$$S = \exp\left[\sum_{j=0}^{4} C_j x^j\right] - S_o \qquad (7.1)$$

The coefficients C_j and the baseline suppression $\exp(C_o) - S_o$ are measured separately for each amplifier system corresponding to any one of the five phototubes since electrical component nonuniformity produces a marked variation from one system to the next. The five coefficients are obtained from a least squares fit to calibration measurements at various signal levels. In practice anywhere from ten to forty such measurements were made at any one time for a particular amplifier system.

In deciding on the degree of polynomial to use in the exponent, the following considerations were noted. The use of too low an order results in obtaining a best fit curve which is smoother than measurable systematic irregularities in the calibration data. These irregularities are attributable to actual departures from evenness in the amplifier's response.

On the other hand, the use of a polynomial of too high a degree would introduce spurious wiggles in response to random errors in reading the deflections. It was found that as the degree of the polynomial was increased beyond four, the smooth, systematic character of the errors between the measurements and the best fit function became obscured by the random fluctuations. That is, any higher terms in the polynomial are of the same order of magnitude as the errors in reading the scope traces.

Generally, the amplifiers are logarithmic for large input voltages. As had been mentioned in an earlier section, there is a gradual transition toward a linear response as the signal level decreases. Figure 7.1 shows a typical amplifier response curve together with calibration points.

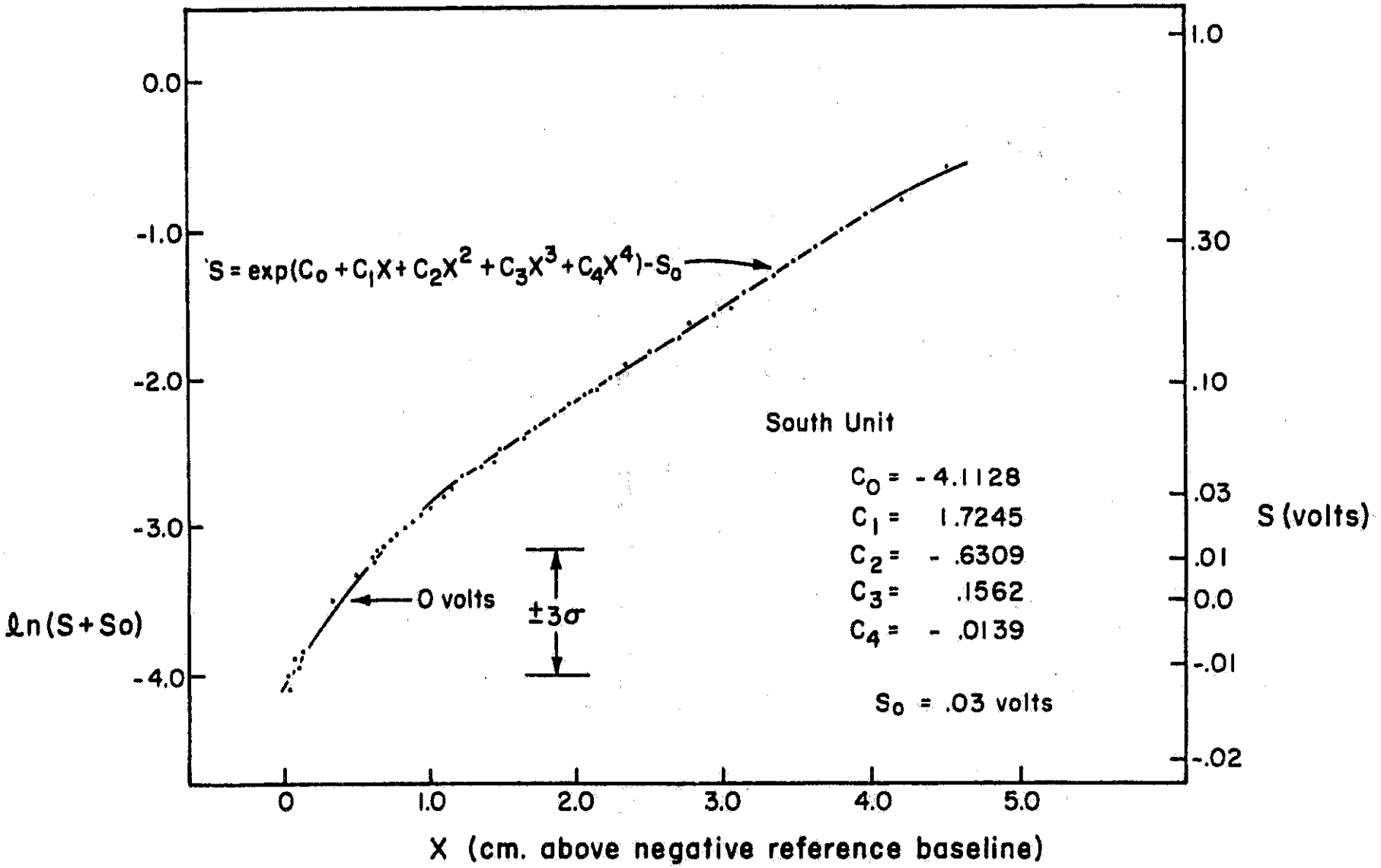

Figure 7.1 Example showing the conformity of actual calibration measurements (dots) to the best fit polynomial relation for S as indicated (solid line). The range $\pm 3\sigma$ indicates the voltage region over which most of the noise may be found.

VIII. ANGULAR RESPONSE OF PHOTOTUBE UNITS

Determination of Angular Response Function

In a rough sense, the phototube assembly would be expected to exhibit a $\cos\theta$ response, where θ is the angle of incidence of the incoming light with respect to the normal. There are, however, a few factors which would modify this response to a limited extent. First, some of the light is reflected as it hits the Plexiglas window surface according to Fresnel's laws of reflection.[36] Only one such reflection takes place since there is optical matching provided by the mineral oil between the Plexiglas surface, filter, and photomultiplier tube surface (see Figure 8.1). The net reflection from the surface (refractive index n = 1.5) is given by an average of the reflections for the two components of polarization. If r_s is the reflection of light polarized perpendicular to the plane of incidence, and r_p refers to the parallel component's reflection then

$$r_s^{1/2} = \frac{\sin(\theta - \theta')}{\sin(\theta + \theta')} \quad \text{and} \quad r_p^{1/2} = \frac{\tan(\theta - \theta')}{\tan(\theta + \theta')} \tag{8.1}$$

where θ' is determined by Snell's law of refraction,

$$\theta' = \sin^{-1}\left(\frac{\sin\theta}{n}\right) . \tag{8.2}$$

Combining the above equations we obtain the net reflection for unpolarized light

$$r = \frac{r_s + r_p}{2} = \frac{1}{2}\left(\frac{n^2-\sin^2\theta - \cos\theta}{n^2-\sin^2\theta + \cos\theta}\right)^2 \left[1 + \left(\frac{\cot\theta\ n^2-\sin^2\theta\ - \sin\theta}{\cot\theta\ n^2-\sin^2\theta\ + \sin\theta}\right)^2\right] \tag{8.3}$$

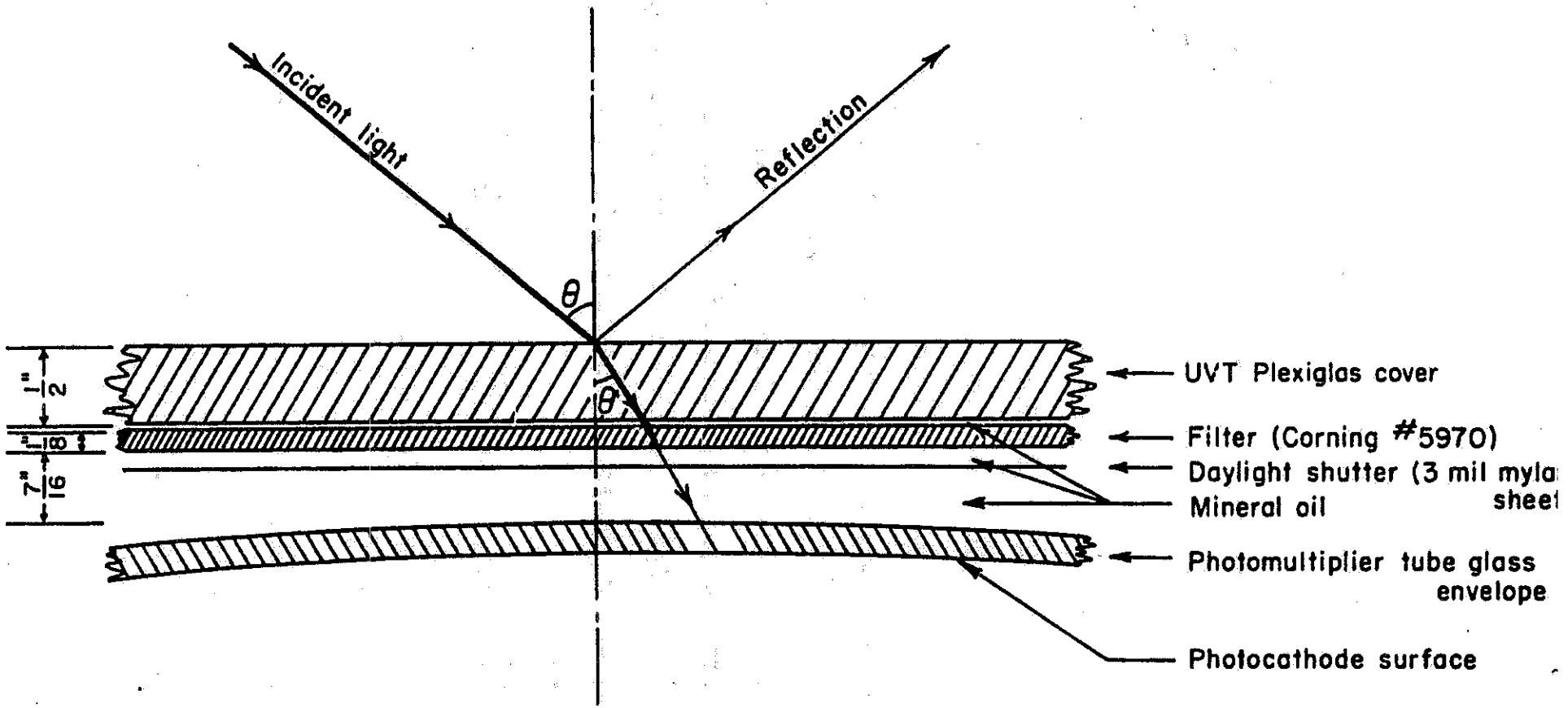

Figure 8.1 Cross section of phototube assembly front face.

One may recall that for nearly normal incidence roughly four percent of the light is reflected. The effect of the reflection seriously reduces the transmitted light intensity for angles greater than about 70°.

The second effect which alters the simple $\cos\theta$ dependence is the variation of path length for light rays passing through the Plexiglas cover, ultraviolet filter, Mylar sheet, mineral oil, and the glass envelope of the photomultiplier tube (see Figure 8.1). For a particular wavelength the amount of light transmitted should go as

$$I = I_o \exp\left[-\left(\alpha(\lambda) + s(\lambda)\right) \sec\theta'\right] = I_o \exp\left[\frac{-n\left(\alpha(\lambda) + s(\lambda)\right)}{(n^2 - \sin^2\theta)^{1/2}}\right] \quad (8.4)$$

where $\alpha(\lambda)$ refers to the opacity (neglecting surface reflection losses) expressed in terms of $\ln \frac{I_o}{I}$ for light passing at normal incidence through everything except the glass tube envelope. $\alpha(\lambda)$ was determined by measuring the absorption in a Cary 14 recording spectrophotometer of a sample consisting of appropriate thicknesses of the different items listed earlier.[28] The corresponding opacity $s(\lambda)$ of the glass in front of the photocathode was evaluated on the basis of measurements of the phototube sensitivity as a function of wavelength. If one compares the sensitivity curve for a quartz face tube with that of a glass face tube having an identical type of photocathode it is evident that the loss of sensitivity in the far ultraviolet may be attributed solely to absorption in the glass. Hence one may assume that the inherent photocathode sensitivity

is relatively flat for blue and ultraviolet light (far above the photocathode work function in energy) and that the transmission of the glass is directly related to the tube sensitivity. Furthermore, we assume that the glass is almost perfectly transmitting for blue light.

In calculating the varying absorption of atmospheric scintillation light as a function of the incident angle θ it is necessary, of course, to evaluate (using Equation 8.4) the transmitted light intensities for a number of wavelengths corresponding to various prominent emission lines and compute an average weighted according to the line strengths. The solid line curve in Figure 8.3 traces the expected angular response of the phototube unit derived from both the reflection loss computation and the net absorption based on the values shown in Table 8.1.

In addition to the previously outlined effects which are easy to calculate, other more subtle factors may influence the angular sensitivity function to a small degree. For instance, at large angles the edge of the filter aperture would cast a shadow on the recessed tube face. The photomultiplier tube itself might have a response somewhat different from a pure cosine dependence since the tube face has a slight curvature, and the cathode photoefficiency is likely to vary with the angle of incident light. It should be emphasized however that these effects are not very pronounced since the maximum value that θ' may attain for $n = 1.5$ is $41.7°$. Nonetheless the angular sensitivity of a photomultiplier tube unit should be

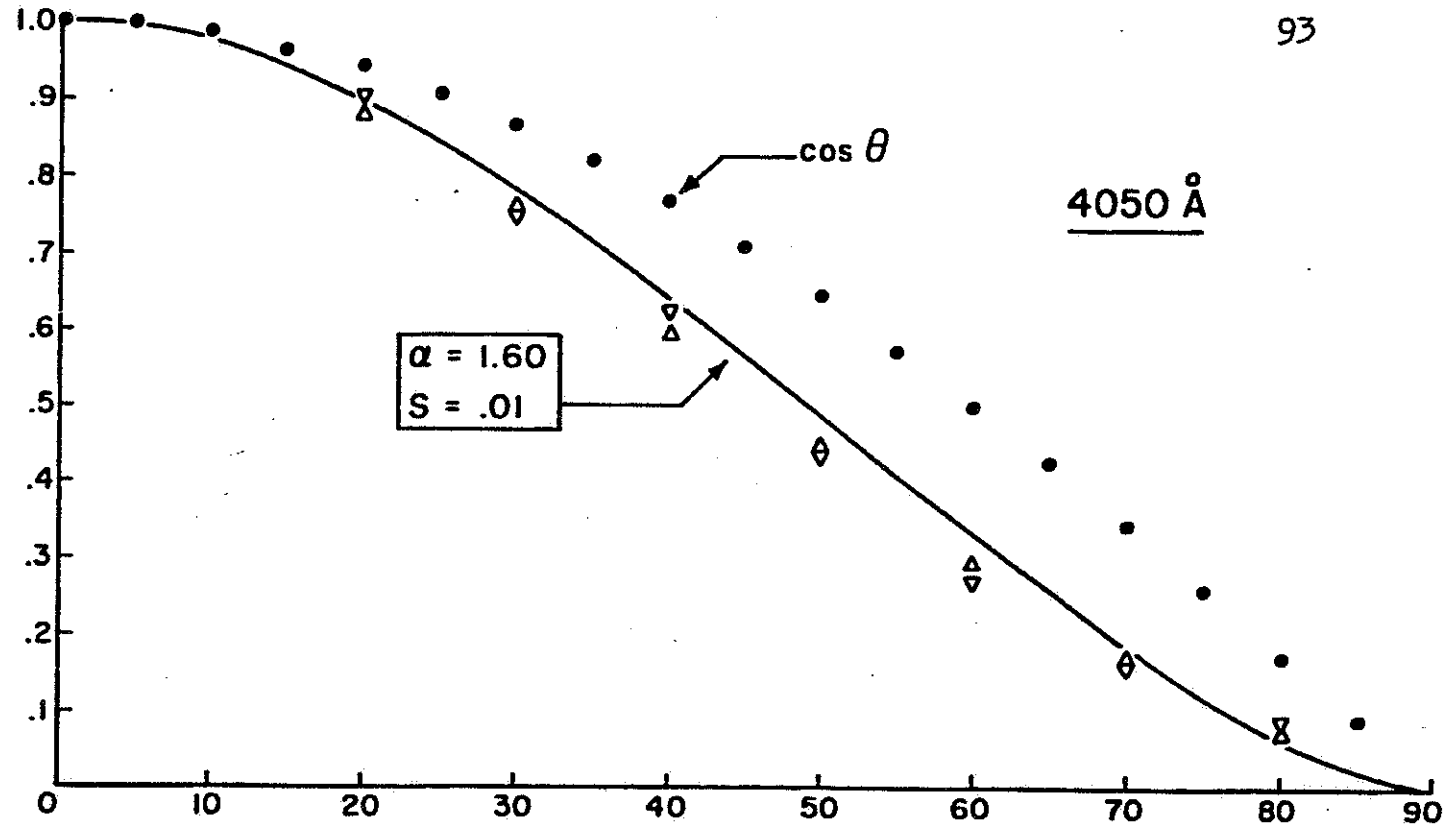

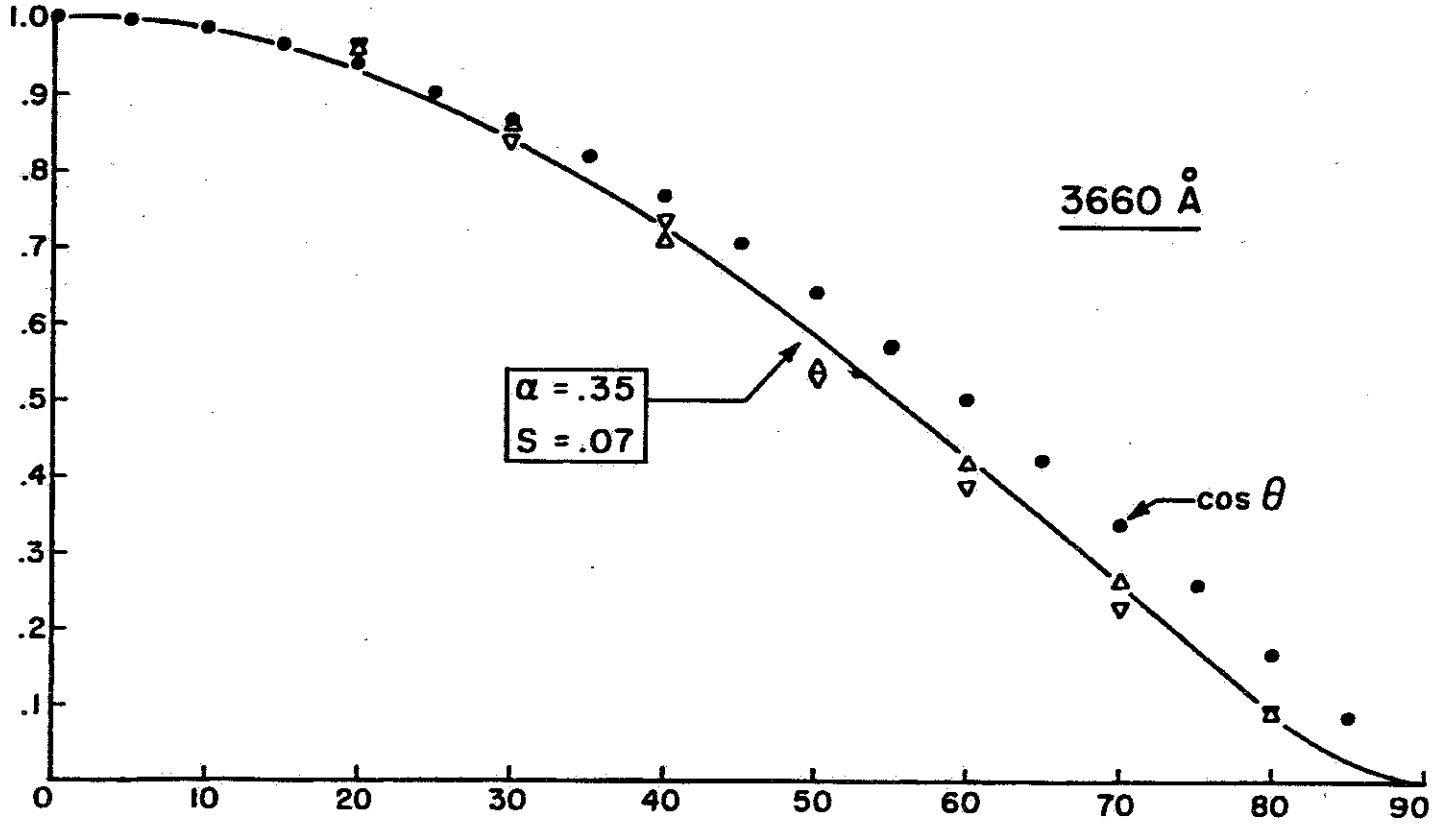

Figure 8.2 Comparison of theory of measurements of the angular response of the phototube units for monochromatic light at two wavelengths.

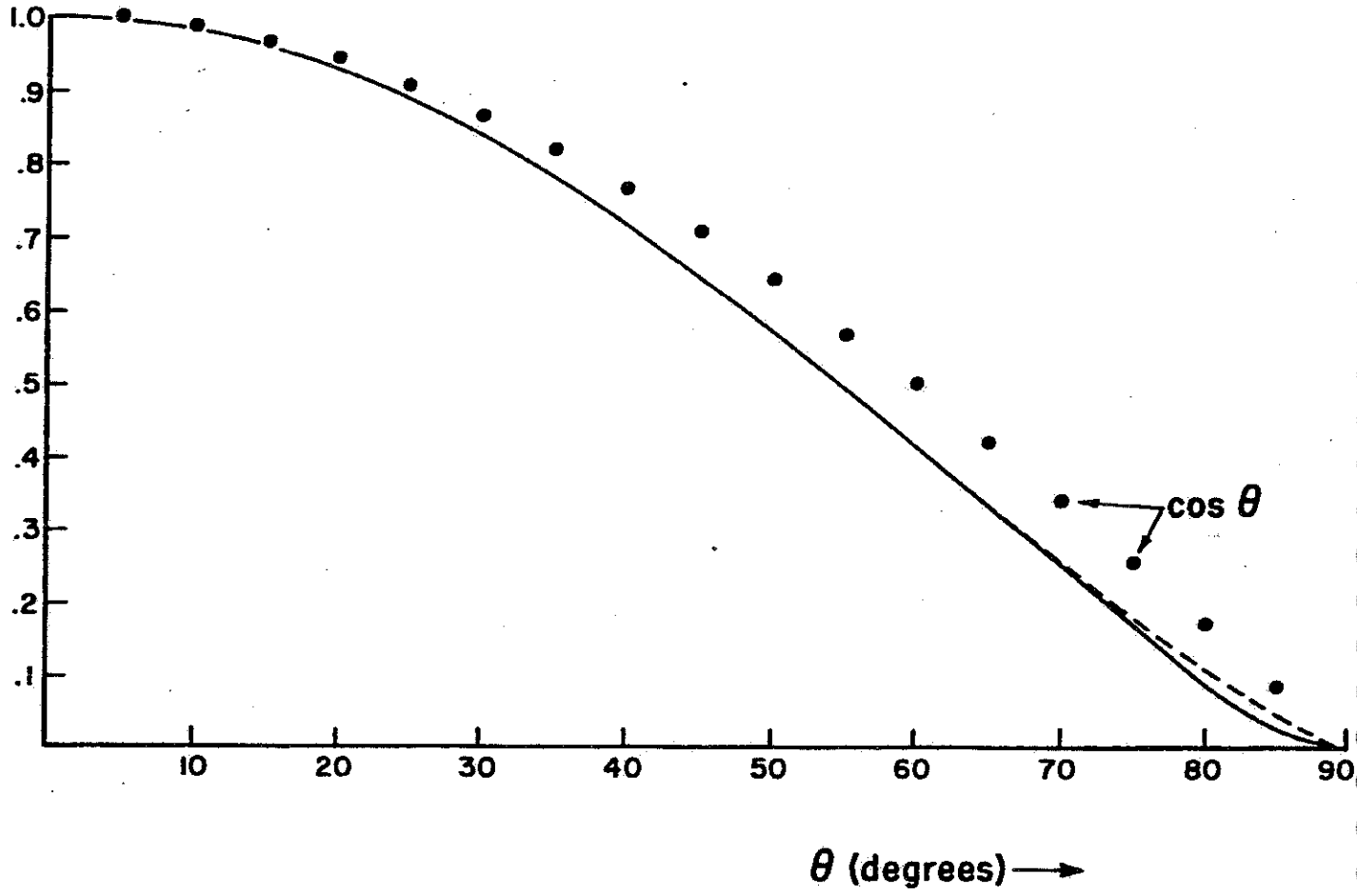

Figure 8.3 Comparison of the calculated angular response curve for scintillation light (solid line) to a $\cos^{1.265}\theta$ relation (dotted line). The two functions are nearly identical for angles less than 65°.

λ (Å)	Y (at sea level)	$s(\lambda)$	$\alpha(\lambda)_{3mm}$
3159	.300	3.00	4.42
3371	.517	1.08	.79
3469	.049	.53	.58
3500	.044	.34	.57
3537	.115	.26	.43
3577	.363	.16	.37
3711	.049	.03	.25
3756	.120	.02	.25
3805	.282	.01	.26
3914	.312	.02	.45
3998	.109	.02	.65
4059	.117	.02	1.60
4278	.159	.01	~3.0

Table 8.1 Tabulation of the more important atmospheric emission lines with quantities used in predicting the angular response function of a photomultiplier unit to scintillation light. The variable Y refers to the number of photons emitted by air for each meter of electron track length. $s(\lambda)$ and $\alpha(\lambda)$ are defined in the text.

checked experimentally at one or two definite wavelengths to ascertain whether or not effects other than surface reflection or filter absorption are important. Such monochromatic measurements have been made, and they are compared in Figure 8.2 to a cosine curve diminished by the losses represented in Equations (8.3) and (8.4). The agreement appears close enough to warrant the evaluation of the angular sensitivity function for scintillation light on the basis of the two effects calculated.

Incorporation of the Angular Response Function into the Analysis

Since the departure of the photomultiplier's angular sensitivity from a pure $\cos\theta$ relationship is not too large, the underlying approach to the problem in solving for the direction of incoming light at any instant may be based on simple vector analysis. That is, one may roughly solve for a flux intensity vector from photomultiplier signals using vector dot products. Nonetheless, some effort should be made to allow for the deviation of the response from a cosine law. Inspection of the angular response curve predicted for scintillation light would suggest that a $\cos^{p}\theta$ function, where p is an empirically determined number slightly greater than one, would be a satisfactory expression of the response for analytical purposes. The value of 1.265 was picked as a good choice for p: a plot of $\cos^{1.265}\theta$ compared with the predicted angular response is shown in Figure 8.3.

For any combination of signals S_i (evaluated from Equation 7.1 and divided by the measured phototube gains) from three different tubes we have three equations of the form

$$F\cos^p\theta_i = F(v_{i1}\alpha + v_{i2}\beta + v_{i3}\gamma)^p = S_i \qquad (8.5)$$

where the subscript i refers to the particular photomultiplier in question. α,β,γ and v_1,v_2,v_3 respectively represent the three direction cosines of the intensity vector $\vec{F}$ (pointing toward the source) and of a vector which is normal to the front surface of a photomultiplier unit. If we adopt a coordinate system where the x axis points east, the y axis points north, and the z axis is up, then the normal vectors respresenting up, north, east, south, and west phototubes are simply (0, 0, 1.00), (0, .866, .500), (.866, 0, .500), (0, -.866, .500), and (-.866, 0, .500). If we exponentiate both sides of each equation (8.5) by 1/p we have a set of linear equations which is easily solved to give α, β, and γ. In other words, exponentiation of all the S_i by 1/p, although altering the magnitude of the intensities, modifies the signals to make their ratios compatible with vector analysis.

A more general treatment of the directional analysis, which will be discussed later, involves the evaluation of probabilities and hence requires the conversion of error distributions arising from uncertainties due to noise instead of the conversion of discrete signal measurements. That is to say, a new probability function P(s') must be determined from a function of the form

$$P(s_i) = \frac{1}{\sqrt{2\pi}\,\sigma_i} \exp\left[- \frac{(S_i - s_i)^2}{2\sigma_i^2} \right] ds_i \qquad (8.6)$$

under the transformation $s' = s^{1/p}$. (σ_i is the amplitude of one standard deviation of the observed random noise associated with the signal.) One way this may be accomplished is to examine the binomial expansion of the expression (signal + noise) and note how the amplitude of the noise is changed.

$$(S+n)^{1/p} = S^{1/p} + \frac{1}{p} S^{(1/p-1)} n + \frac{1}{2p}\left(\frac{1}{p} - 1\right) S^{(1/p-2)} n^2 + \ldots \qquad (8.7)$$

This expansion in powers of n converges rapidly for large signal-to-noise ratios and for $p \approx 1$. Namely, the third term is smaller than the second by a factor of $\left(\frac{1}{p} - 1\right)\frac{n}{2S}$. To a first approximation, the effect of an angular response which is steeper than $\cos\theta$ (i.e. $p > 1$) may be said to enhance a large signal-to-noise ratio over that which would be assumed if the response were purely $\cos\theta$ (and hence would lower the directional uncertainty). Neglecting the n^2 and higher terms gives us a new distribution

$$P(s') = \frac{1}{\sqrt{2\pi}\,\sigma'} \exp\left[- \frac{(S^{1/p} - s')^2}{2\sigma'^2} \right] ds' \qquad (8.8)$$

where $\sigma' = \frac{1}{p} S^{(1/p-1)} \sigma$.

The aforementioned approximation, although it is instructive, has the serious shortcoming of failing for low signal-to-noise ratios. As low ratios are to be encountered frequently in this experiment, a more rigorous approach is

necessary. The actual transformation of the probability function from s to s' gives

$$P(s') = \frac{1}{\sqrt{2\pi}\,\sigma} \exp\left[- \frac{(S - s'^{p})^2}{2\sigma^2} \right] \left(\frac{ds}{ds'}\right) ds'$$

$$= \frac{1}{\sqrt{2\pi}\,\sigma} \exp\left[- \frac{(S - s'^{p})^2}{2\sigma^2} \right] ps'^{p-1} ds' \qquad (8.9)$$

This distribution would, of course, be expected to be somewhat non-Gaussian for low signal-to-noise ratios.

The more complicated (non-Gaussian) character of the true distribution for s' makes later analysis rather difficult, and thus it is desirable to substitute a Gaussian distribution which approximates the true distribution. The fit need be valid only for positive s' (although S may be negative) since the expected value of s' for any given direction may never be negative. Therefore, a new function

$$P'(s') = C \exp\left[- \frac{(S' - s')^2}{2\sigma'^2} \right] ds' \qquad (8.10)$$

may be introduced which should closely resemble the true distribution mentioned earlier (Equation 8.9). The method of fitting involves the evaluation of a binomial regression equation in terms of ln P(s') versus s' by the method of least squares. Solution of the normal equations gives constants which, in turn, determine the most probable value S', the standard deviation σ', and a normalizing constant C. Actual comparisons of P'(s') to P(s') show that the fit is quite satisfactory for various signal-to-noise ratios--even if S is negative.

IX. INSTANTANEOUS DIRECTIONAL PROBABILITY FUNCTION

Intensity Vector Distribution

As stated earlier, a description of the received light flux at the observing station may be made in terms of an intensity vector $\vec{F}$ which points toward the source of light and whose length equals the magnitude of the flux (now exponentiated by 1/p). For a given F, the probability of obtaining a signal S_i' from a particular phototube (designated by i) is

$$P'(S_i') = \frac{1}{\sqrt{2\pi}\,\sigma'} \exp\left[-\frac{(S_i' - \max(\vec{V}_i\cdot\vec{F},0))^2}{2\sigma_i'^2}\right] dS_i' \tag{9.1}$$

where $\max(\vec{V}\cdot\vec{F}, 0)$ equals zero or the vector dot product of the tube face normal and the intensity vector, whichever is greater. P'(s') may be rewritten as P'(F) by merely replacing ds' by $d(\vec{V}\cdot\vec{F})$, which is a differential in the $\vec{F}$ vector space along the direction of $\vec{V}_i$ ($|\vec{V}| = 1$). That is, ds' represents only a linear combination of the components of $\vec{F}$, and hence replacing ds' by dF multiplies the distribution by some constant. The combined probability for all five independent measurements is $\prod_{i=1}^{5} P'(S_i')$. For the moment we shall not concern ourselves with various constant factors needed to normalize the joint probability function. It is easier to normalize distributions which are derived later in the analysis. The question of normalization is of little importance in the analytical interpretation of the results anyhow.

The logarithm of the probability is given as

$$w(\vec{F}) = -\frac{1}{2}\sum_{i=1}^{5}\left(\frac{S_i' - \max(\sum_{j=1}^{3} v_{ij}f_j, 0)}{\sigma_i'}\right)^2 \qquad (9.2)$$

where the summation over j represents the three products of the x, y, and z vector components. The vector $\vec{F}_o$ whose position is at the maximum of $w(\vec{F})$ may be found by solving simultaneously the three equations

$$\frac{\partial w}{\partial f_k} = \sum_i v_{ij}\left(\frac{S_i' - \sum_{j=1}^{3} v_{ij}f_{oj}}{\sigma_i'^2}\right) \equiv 0 \qquad (9.3)$$

for k = 1, 2, 3. The summation over i in this case includes only the phototube units that can "see" the vector $\vec{F}$ (i.e. $\vec{V}_i \cdot \vec{F} \geq 0$). If the equations are rewritten in the form

$$\sum_{j=1}^{3}\sum_i \frac{v_{ik}v_{ij}}{\sigma_i'^2}f_{oj} = \sum_i \frac{v_{ik}S_i'}{\sigma_i'^2} \qquad (9.4)$$

it is clear that we have a system of simultaneous linear equations in f_1, f_2, and f_3. Furthermore the second derivatives of w give us the error matrix terms:

$$H_{k,\ell} \equiv \frac{\partial^2 w}{\partial f_k \partial f_\ell} = -\sum_i \frac{v_{ik}v_{i\ell}}{\sigma_i'^2} \qquad (9.5)$$

The fact that the latter terms are constants indicates that the probability function for $\vec{F}$ is purely a three-dimensional Gaussian distribution. The the probability may be expressed in the more simple form (again unnormalized).

$$P'(\vec{F}) = P'(f_1,f_2,f_3) = C \exp\left[-\frac{1}{2}\sum_{k=1}^{3}\sum_{\ell=1}^{3} H_{k,\ell}(f_{ok}-f_k)(f_{o\ell}-f_\ell)\right] \tag{9.6}$$

where C is a constant to be determined later.

Except for the phototube unit which points upward, various portions of the sky are invisible to different units. This fact was reflected in the selectiveness of the summation over i in Equations (9.3), (9.4) and (9.5). There exist nine distinct regions in the sky which have different combinations of i applicable to the differentiated expressions. These regions are shown in Figure 9.1 where the numbers refer to the values of i allowed in the sums.

It should be clear that, in general, each region will have a different value for $\vec{F}_o$ and a different error matrix H since Equations (9.4) and (9.5) will vary. The probability density $P'(\vec{F})$ in the <u>entire</u> F vector space, however, must be continuous since there are no abrupt discontinuities from one region to the next in the expected response from each phototube unit. Therefore, $P'(\vec{F})$ may be constructed for the entire sky by matching at the boundaries the solutions obtained from Equations (9.4) and (9.5) within each region. This matching is accomplished by adjusting the constant C in Equation (9.6) for each case. It follows from the continuity of P' that the two spatial derivatives of P' parallel to a boundary between regions must be equal on either side of the boundary, whereas the perpendicular spatial derivative may be discontinuous. The

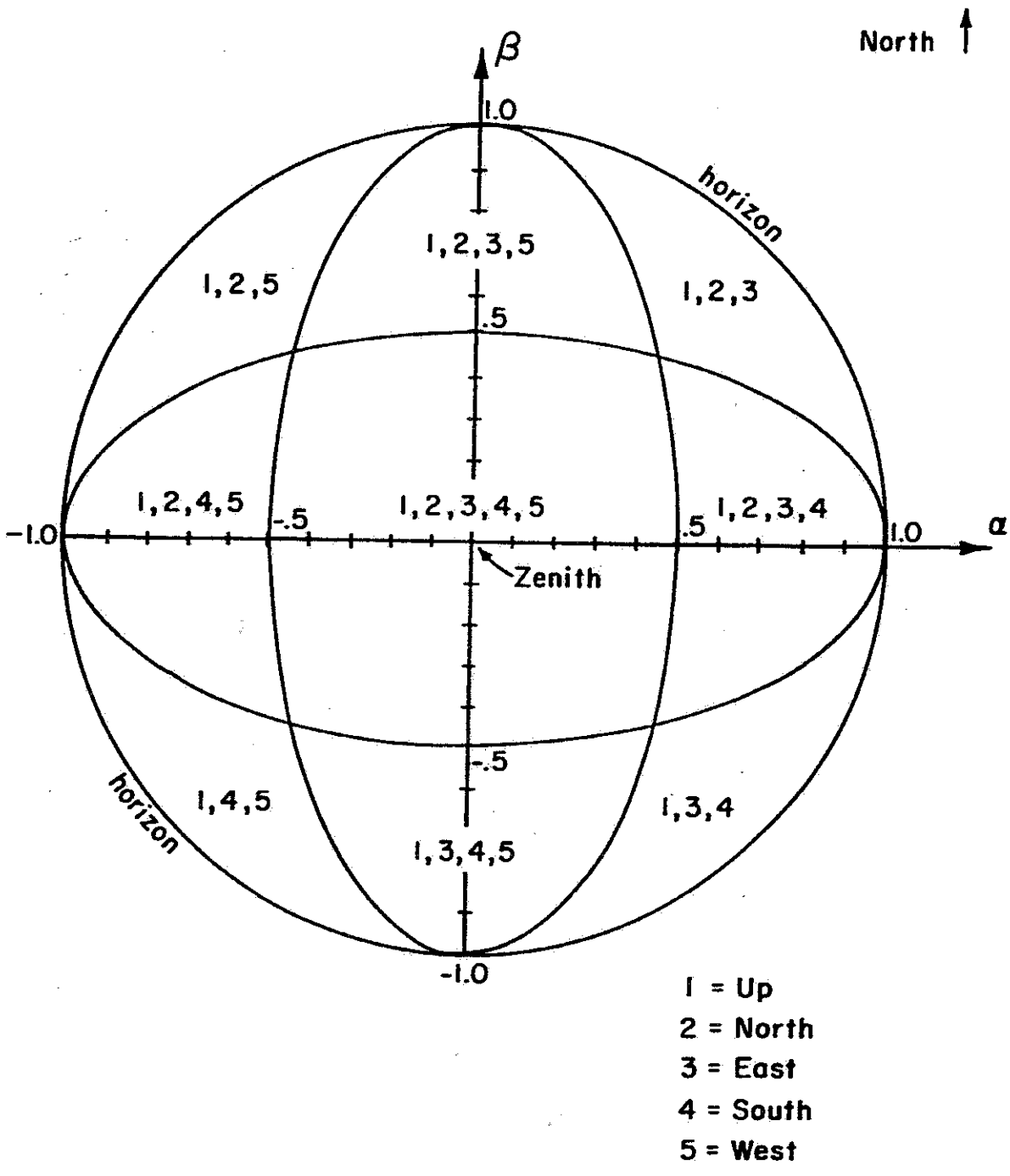

Figure 9.1 Nine regions having different phototube visibility configurations. The diagram is plotted in terms of α and β, which are the x and y direction cosines.

discontinuous property of one of the derivatives is evidenced by the kink in the contours sketched in Figure 9.3 (page 115).

Inspection of Equation (9.5) will show that the error matrix may be evaluated by simply multiplying the matrix

$$\begin{pmatrix} 0 & 0 & \frac{.866}{\sigma_3'} & 0 & -\frac{.866}{\sigma_5'} \\ 0 & \frac{.866}{\sigma_2'} & 0 & -\frac{.866}{\sigma_4'} & 0 \\ \frac{1}{\sigma_1'} & \frac{.5}{\sigma_2'} & \frac{.5}{\sigma_3'} & \frac{.5}{\sigma_4'} & \frac{.5}{\sigma_5'} \end{pmatrix}$$

by its transpose. One or two columns of the above matrix would be deleted if the matrix were to be evaluated for a region other than the central one which surrounds the zenith. The error matrix for the central region would be

$$H = \frac{1}{\sigma'^2}\begin{pmatrix} 1.5 & 0 & 0 \\ 0 & 1.5 & 0 \\ 0 & 0 & 2.0 \end{pmatrix} \qquad (9.7)$$

if the various σ_i' were the same for each of the five measurements.

The nature of the $P'(\vec{F})$ distribution (Equation 9.6) may be easily visualized by noting that the family of surfaces where the function is a constant consists of similar, concentric ellipsoids centered on $\vec{F}_o$. In particular, an ellipsoid for the distribution associated with the matrix given in Equation (9.7) would be an oblate spheroid whose axis pointed in the z direction. The surface where $P'(\vec{F})$ for the latter

matrix is down by a factor of $e^{1/2}$ from its maximum at $\bar{F}_o$ is characterized by a spheroid whose major diameter would be equal to $2(1.5)^{-1/2}\sigma'$ and whose minor axis would equal $2(2.0)^{-1/2}\sigma'$. A measurement of the uncertainty in $\bar{F}$ may be expressed in terms of the volume of the spheroid

$$V = \frac{4\pi}{3}(1.5^{-1/2}\sigma')^2(2.0^{-1/2}\sigma') = 1.97\sigma'^3 \qquad (9.8)$$

The volume just described may be evaluated for the general case (any H) by noting that after the matrix has been reduced to a diagonal form by a rotation operation, the volume is merely $\frac{4\pi}{3}\,|H|^{-1/2}$. Since the rotation operator matrix and its inverse are unitary, the determinant is unchanged by the operation, and hence it may be said that

$$V = \frac{4\pi}{3}\,|H|^{-1/2} \qquad (9.9)$$

for any error matrix H.

In contrast to H given in Equation (9.7) the error matrix for a region seen by only three phototube units would be of a form similar to

$$H = \frac{1}{\sigma'^2}\begin{pmatrix} .75 & 0 & .433 \\ 0 & .75 & .433 \\ .433 & .433 & 1.5 \end{pmatrix} \qquad (9.10)$$

(upper right region in Figure 9.1). Applying Equation (9.9) to this matrix gives a volume of $3.95\sigma'^3$ which is greater than the value obtained for the central region by a factor of two.

Reduction of P'(F) to a Two-Dimensional Direction Probability Function

The analysis of the geometrical parameters of an event makes use of only measurements in direction, for it is difficult to incorporate variations in observed intensity into the analysis since the shower size and growth curve and the atmospheric transmission coefficient are not known. The flux vector distribution $P'(\vec{F})$, however, describes the probability of having the incident light come from a certain direction with a particular intensity. It is necessary at this stage of the analysis, therefore, to reduce the intensity vector probability density to a two-dimensional distribution which describes the probability that the flux has a given direction regardless of its intensity. This is accomplished by integrating over all possible values of intensity, i.e. radially outward along a ray extending from the origin to infinity in the $\vec{F}$ vector space. To accomplish this $P'(\vec{F})$ must be re-expressed in terms of a scalar intensity and some suitable direction coordinate system.

Before formulating the integral over intensity it is necessary to digress and consider the choice of an appropriate two-dimensional coordinate system for expressing direction. It is convenient to use the terminology associated with global map projections (mapping a sphere onto a plane) when reference is made to a particular representation. If a point on a sphere were used to designate a direction, the direction would be

defined in terms of the x and y coordinates on a plane according to the particular method of mapping. Various projection schemes have different distortion characteristics or other undesirable features*, and it is necessary to reach a compromise system which avoids serious mathematical difficulties in the subsequent analysis.

Outside of the more transparent advantages of having a mapping projection which is easily interpretable and whose mathematical formulation is simple and without irregularities in the form of divergences or discontinuities, there are a few additional criteria which are appropriate to consider for the application to the analysis of shower events. For instance, the transformation of a small unit of solid angle to the plane should give roughly a constant area for any position above the horizon. That is, the Jacobian representing the conversion from $d\Omega$ to dxdy should approach neither zero nor infinity for any region that may be considered. If this requirement is not satisfied, then probability functions of a simple character covering large solid angles would become distorted under the mapping and hence would become more complex. For example, a distribution whose probability contours were elliptical and roughly Gaussian might become badly egg-shaped or asymmetric under a transformation which lacked the aforementioned property. We need not necessarily have an equal area projection in the strict sense however (i.e. the Jacobian equal to a constant

*A discussion of different projection properties may be found in ref. 37.

everywhere). It would also be desirable, although not essential, that the projection be orthomorphic to more accurately preserve the shape of small distribution functions in solid angle.

Another consideration for the mapping scheme arises from the fact that the straight trajectory representing the axis of the shower will conform to a great circle on the sphere. In subsequent stages of the analysis, therefore, the determination of the plane of best fit to the sequential readings in direction for an entire event would be facilitated if any great circle had a simple mathematical interpretation in the representation being employed. More specifically, any plane intersecting the center of the sphere should be expressible in terms of a two parameter family of geometrically simple arcs. Perhaps the most suitable mapping in this respect is the gnomonic projection, which maps great circles into straight lines. Unfortunately this projection seriously exaggerates the size of solid angles near the horizon.

Without going into detail over the reasons for eliminating various categories of mapping, it may be said that a zenithal (or azimuthal) projection seems most appropriate to our problem. The constructions of perspective zenithal projections are most easily visualized if one imagines a transparent sphere being illuminated by a point source of light which casts shadows of the sphere's surface features onto a tangent plane. If the light source an infinite distance away illuminates

the sphere we have the orthographic projection, where the x and y variables correspond simply to the direction cosines α and β (see, for example, Figure 9.1). The orthographic projection has the drawback of compressing regions near the horizon (at the horizon the Jacobian $\frac{\partial(F_1,F_2,F_3)}{\partial(\alpha,\beta,|\vec{F}|)}$ equals infinity). On the other hand, the gnomonic projection, which represents illumination from the center of the sphere and whose coordinates are α/γ, β/γ, does exactly the opposite: it elongates regions near the horizon (the Jacobian rapidly approaches zero).

A satisfactory compromise between the two undesirable effects just mentioned may be found with the stereographic projection. Here the illumination source is located on the surface of the sphere diametrically opposed to the tangent point of the plane (see Figure 9.2). The coordinates in this case are

$$x = \frac{2\alpha}{1+\gamma} \; ; \qquad y = \frac{2\beta}{1+\gamma} \qquad (9.11\ a,b)$$

for a sphere of unit radius. The horizon is represented by a circle of radius two, and the entire visible sky is contained within the circle with the zenith at the center. As will be demonstrated later, the Jacobian does not vary much above or even slightly below the horizon, and all great circles are easily representable. Hence the stereographic projection has been chosen to represent the formulation of direction into two dimensions.

Returning to the problem of expressing the integral over

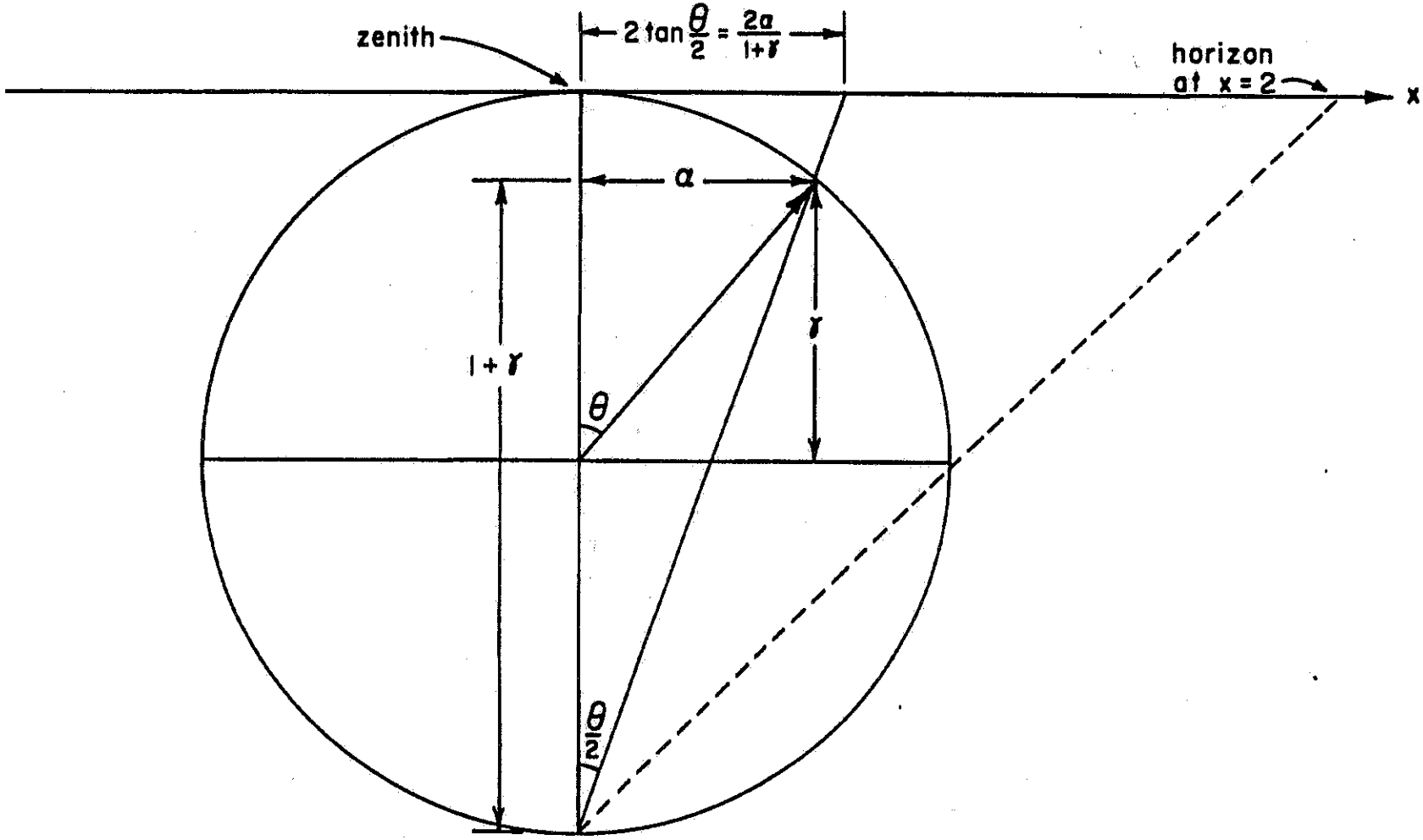

Figure 9.2 Illustration of the construction of the stereographic projection for a point in the sky east of the observer with zenith angle θ.

intensity, we must first reformulate $P'(\vec{F})$ in terms of the directions x, y, and the intensity $|\vec{F}|$ (hereafter referred to as F). The inverse relations derivable from Equations (9.11 a,b) are

$$\alpha = \frac{4x}{4+r^2} \quad ; \quad \beta = \frac{4y}{4+r^2} \quad ; \quad \gamma = \frac{4-r^2}{4+r^2} \qquad (9.12\ a,b,c)$$

where $r^2 = x^2 + y^2$. Equation (9.6) may be recast into the form

$$P'(\alpha,\beta,F) = C \exp\Big[-\tfrac{1}{2}(H_{11}\alpha^2 + H_{22}\beta^2 + H_{33}\gamma^2 + 2H_{13}\alpha\gamma + 2H_{23}\beta\gamma)F^2 + (H_{11}\alpha f_{01} + H_{22}\beta f_{02} + H_{33}\gamma f_{03} + H_{13}(\gamma f_{01} + \alpha f_{03}) + H_{23}(\beta f_{03} + \gamma f_{02})F - \tfrac{1}{2}(H_{11}f_{01}^2 + H_{22}f_{02}^2 + H_{33}f_{03}^2 + 2H_{13}f_{01}f_{03} + 2H_{23}f_{02}f_{03})\Big] \qquad (9.13)$$

by substituting $(F\alpha, F\beta, F\gamma)$ for the vector $(f_1,f_2,f_3) \equiv \vec{F}$. Making use of Equations (9.12) and regrouping terms by powers of F we get

$$P'(x,y,F) = C \exp\left[-\tfrac{1}{2} g_1 F^2 + g_2 F - \tfrac{1}{2} g_3 \right] df_1 df_2 df_3$$

where

$$g_1 = \frac{1}{(4+r^2)^2}\left\{16H_{11}x^2 + 16H_{22}y^2 + H_{33}(4-r^2)^2 + 8H_{13}x(4-r^2) + 8H_{23}y(4-r^2)\right\}$$

$$g_2 = \frac{1}{4+r^2}\left\{4H_{11}xf_{01} + 4H_{22}yf_{02} + H_{33}(4-r^2)f_{03} + H_{13}\left[4xf_{01} + (4-r^2)f_{03}\right] + H_{23}\left[4yf_{03} + (4-r^2)f_{02}\right]\right\}$$

$$g_3 = H_{11}f_{01}^2 + H_{22}f_{02}^2 + H_{33}f_{03}^2 + 2H_{13}f_{01}f_{03} + 2H_{23}f_{02}f_{03} \qquad (9.14)$$

The Jacobian for transforming a volume $df_1df_2df_3$ into the volume

dxdydF is given by

$$J = \frac{\partial(f_1,f_2,f_3)}{\partial(x,y,F)} = \begin{vmatrix} \frac{\partial f_1}{\partial x} & \frac{\partial f_2}{\partial x} & \frac{\partial f_3}{\partial x} \\ \frac{\partial f_1}{\partial y} & \frac{\partial f_2}{\partial y} & \frac{\partial f_3}{\partial y} \\ \frac{\partial f_1}{\partial F} & \frac{\partial f_2}{\partial F} & \frac{\partial f_3}{\partial F} \end{vmatrix}$$

$$= \begin{vmatrix} F\frac{4(4+r^2)-8x^2}{(4+r^2)^2} & -F\frac{8xy}{(4+r^2)^2} & -F\frac{16x}{(4+r^2)^2} \\ -F\frac{8xy}{(4+r^2)^2} & F\frac{4(4+r^2)-8y^2}{(4+r^2)^2} & -F\frac{16y}{(4+r^2)^2} \\ \frac{4x}{4+r^2} & \frac{4y}{4+r^2} & \frac{4-r^2}{4+r^2} \end{vmatrix}$$

which reduces to

$$J = \frac{16\,F^2}{(4+r^2)^2} \qquad (9.15)$$

For a given value of F the Jacobian changes by a factor of four between the zenith and the horizon.

The new probability function P(x,y) may now be expressed in terms of the integral over intensity

$$P(x,y) = dxdy\int_0^\infty P'(x,y,F)J\,dF$$

$$= \frac{16C}{(4+r^2)^2}\,dxdy\int_0^\infty F^2\,\exp\left[-\frac{1}{2}\,g_1F^2 + g_2F - \frac{1}{2}\,g_3\right]dF \qquad (9.16)$$

This integral may be solved without difficulty by using the substitution $F' = F - \frac{g_2}{g_1}$. Then

$$P = \frac{16C}{(4+r^2)^2}\,dxdy \int_{-\frac{g_2}{g_1}}^{\infty} \left(F'^2 + \frac{2g_2}{g_1}F' + \frac{g_2^2}{g_1^2}\right) \exp\left[-\frac{1}{2}g_1F'^2 + \frac{1}{2}\frac{g_2^2}{g_1} - \frac{1}{2}g_3\right] dF' \tag{9.17}$$

which, for convenience in discussion, may be broken down into the separate integrals,

$$P = \frac{16C}{(4+r^2)^2}\,dxdy \exp\left[\frac{1}{2}\left(\frac{g_2^2}{g_1} - g_3\right)\right] \left\{ \int_{-\frac{g_2}{g_1}}^{\infty} F'^2 \exp\left[-\frac{1}{2}g_1F'^2\right] dF' + \frac{2g_2}{g_1}\int_{-\frac{g_2}{g_1}}^{\infty} F' \exp\left[-\frac{1}{2}g_1F'^2\right] dF' + \frac{g_2^2}{g_1^2}\int_{-\frac{g_2}{g_1}}^{\infty} \exp\left[-\frac{1}{2}g_1F'^2\right] dF' \right\} \tag{9.18}$$

The first integral in (9.18) may be solved by integration by parts: Let $u = -\frac{\exp(-1/2\ g_1F'^2)}{g_1}$ and $v = F'$. Then according to the relation $\int v\,du = uv - \int u\,dv$ we get

$$\int_{-\frac{g_2}{g_1}}^{\infty} F'^2 \exp\left[-\frac{1}{2}g_1F'^2\right] dF' = -\frac{F' \exp\left[-\frac{1}{2}g_1F'^2\right]}{g_1}\Bigg|_{-\frac{g_2}{g_1}}^{\infty} + \frac{1}{g_1}\int_{-\frac{g_2}{g_1}}^{\infty} \exp\left[-\frac{1}{2}g_1F'^2\right] dF' \tag{9.19}$$

The integral on the right-hand side of Equation (9.19) is simply an error function and may be grouped with the third integral of Equation (9.18). The solution of the second integral is straightforward, and hence P may be reduced to an expression involving algebraic quantities and an error function. After the integration limits are substituted into the derived algebraic expressions we obtain

$$P = \frac{16C}{(4+r^2)^2}\,dxdy\,\exp\left[-\frac{g_3}{2}\right]\left\{\frac{g_2}{g_1^2} + \left(\frac{1}{g_1} + \frac{g_2^2}{g_1^2}\right)\sqrt{\frac{\pi}{2g_1}}\exp\left[\frac{g_2^2}{2g_1}\right]\left(1 - \operatorname{erf}\left[-\frac{g_2}{\sqrt{2g_1}}\right]\right)\right\} \qquad (9.20)$$

noting that

$$\int_{-\frac{g_2}{g_1}}^{\infty} \exp\left[-\frac{1}{2}g_1F'^2\right]dF' = \sqrt{\frac{\pi}{2g_1}}\left(1 - \operatorname{erf}\left[-\frac{g_2}{2g_1}\right]\right)$$

In the computer program performing the analysis the evaluation of the error function is accomplished by a numerical approximation procedure.(38)

Generally it has been found that P(x,y) closely resembles a two-dimensional Gaussian distribution in the region where the probability is significantly large. Occasionally when P is very broad or when the maximum of P is near the boundary between the tube visibility regions discussed earlier we may find a moderate amount of irregularity and departure from Gaussian form. Figure 9.3 is a contour sketch based on a grid of numbers printed by the computer* which represent the logarithm of P for a sample reading. The area shown is an enlargement of the neighborhood surrounding the peak of P in the x,y diagram. This presentation serves as an illustration of the deformation that takes place if the peak is centered

*Figure 9.3 was constructed from a special printout of ℓn P over a small region of sky. Such detail could not have been obtained from the routinely given form of output shown in Figure 9.4.

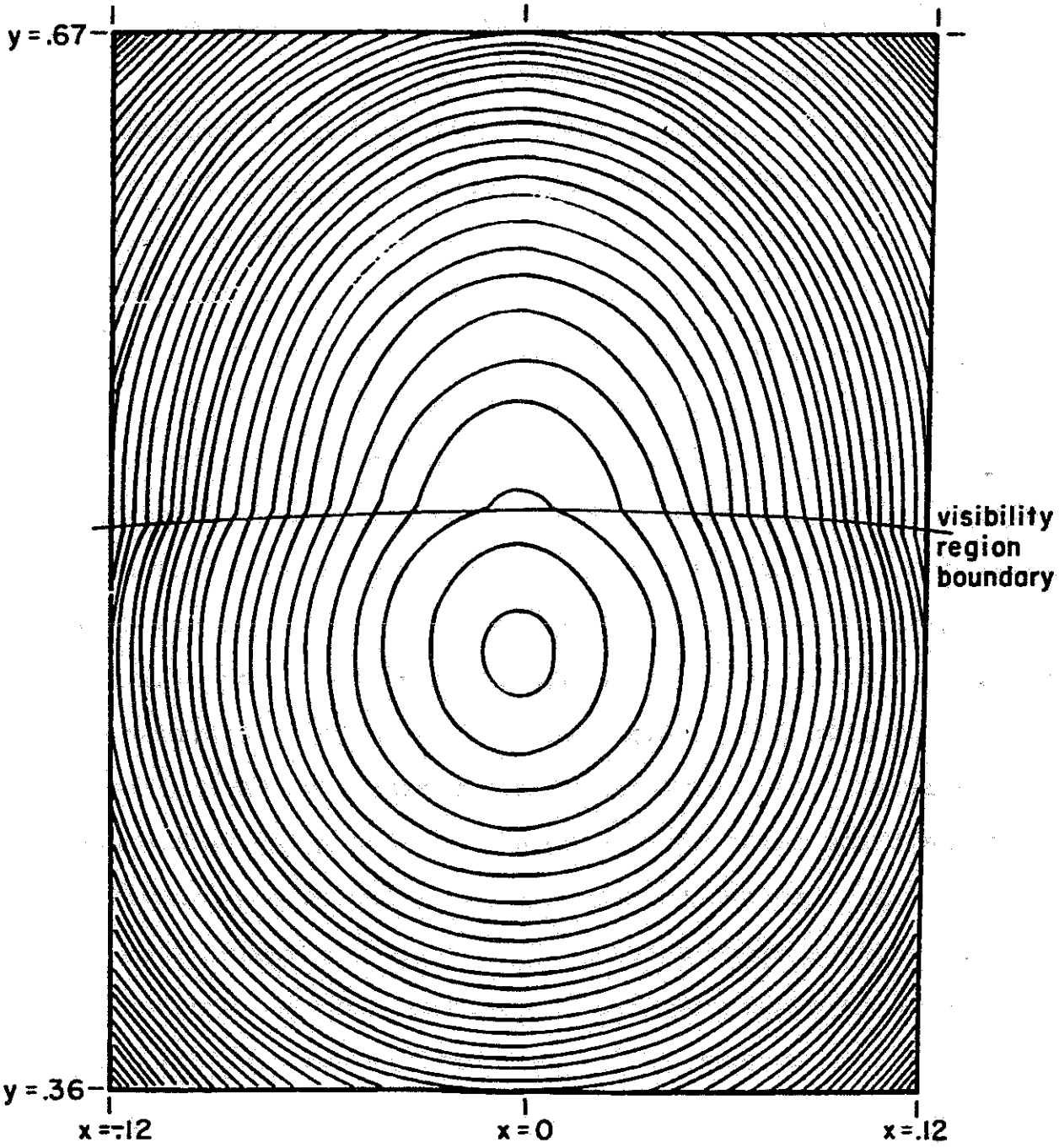

Figure 9.3 Contours of equal probability values for a sample reading. Each contour interval represents a change of 2.5% in relative probability. The symmetry of this peak (which facilitates drawing) results from the fact that the reading chosen had equal signals in west and east channels.

near a region boundary. As a rule the lack of conformity of the distribution to an elliptical Gaussian function rarely exceeds that shown in this example.

The computer program contains instructions to evaluate the logarithm of P for many combinations of x and y lying on a grid of points covering the entire sky above the horizon. An example of the standard printout of this information may be seen in Figure 9.4. The numbers shown represent ℓn P times ten. Each set of the five instantaneous CRT deflections (for a given time instant) fed to the computer produces a page of numbers of the type shown in the figure which, upon immediate inspection, conveys the impression of a blurred snapshot of the shower. If one views the pages in rapid succession, it is possible to perceive the sequential character of the readings taken at progressively later times. The latter inspection quickly reveals the character of the shower's movement, and if the probability hills were to move in an irregular fashion one would have good reason to regard the event with some suspicion.

The reading represented in Figure 9.4 was chosen from the analysis of an event simulated by another computer program (to be described in Chapter XII). We therefore had a priori information on the true position of the light source in the sky which has been designated by a cross (drawn in by hand) on the printout. The error in the position of the distribution's center (as compared with the true position) for the example shown in the figure is in excess of what is typically found. As a check on the performance of the analysis program's accuracy in

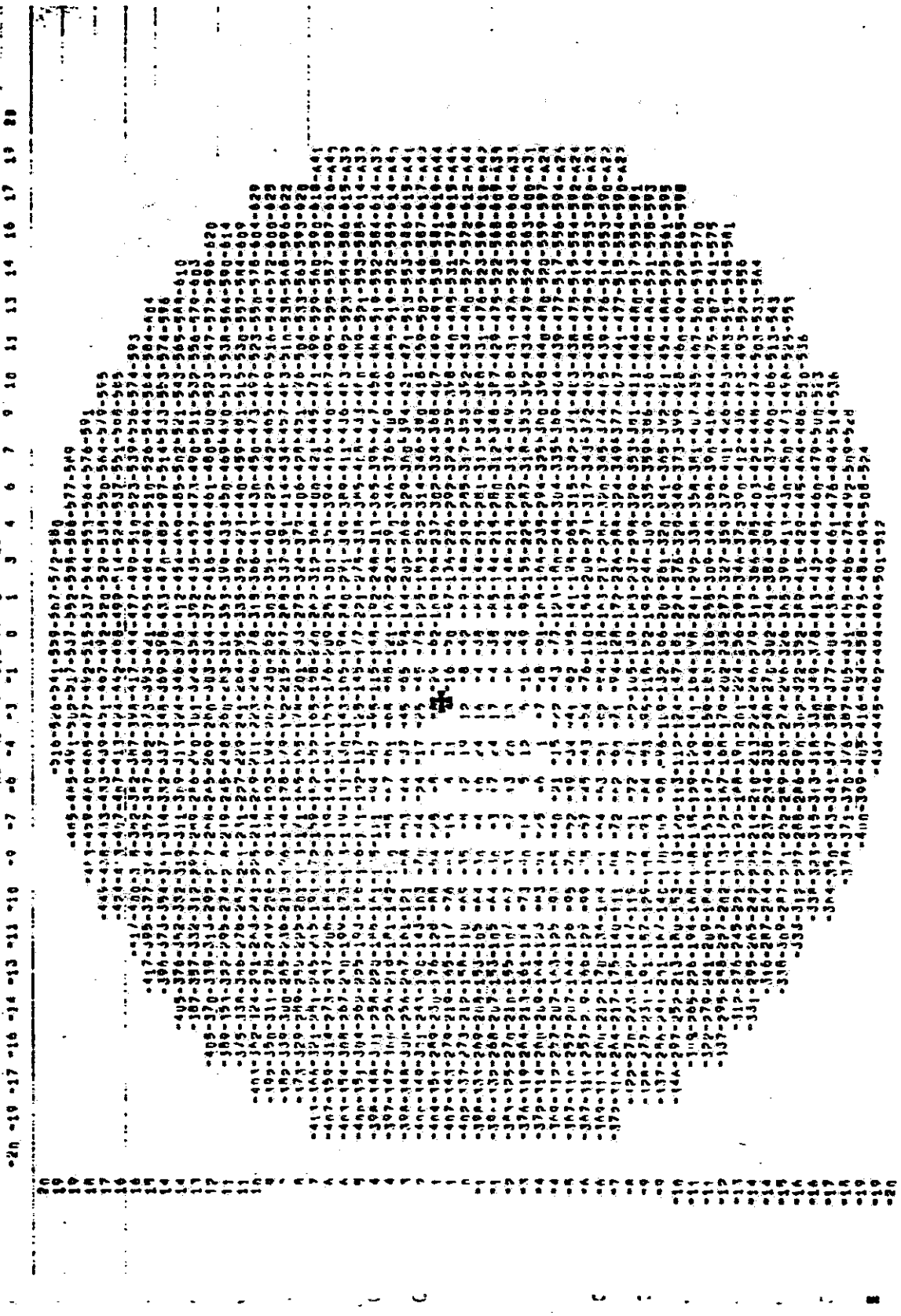

Figure 9.4

forecasting probabilities, a study was made on the frequency of occurrence for errors of different magnitude, the severity of the error being designated by the ratio of the probability assigned to the true position divided by the probability at the peak of the distribution. In Figure 9.4, for example, the error shown should occur with a relative frequency of about $e^{-2.4}$. A histogram showing the results of sixty-two analyses of simulated readings demonstrates a good agreement between the expected frequency curve and the actual distribution of errors (see Figure 9.6 below).

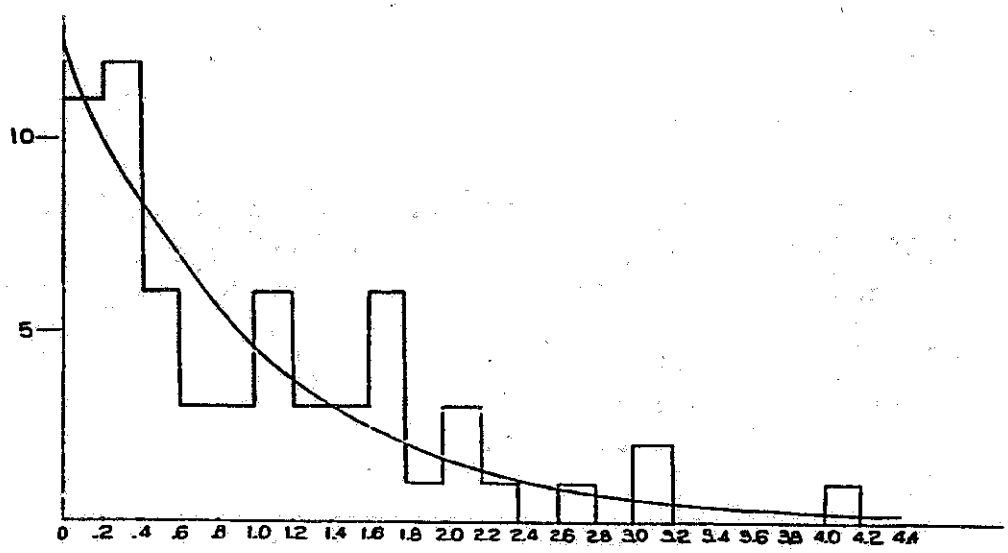

Figure 9.6

The expected frequency should equal the product of P (the probability per unit area in x and y) and the area enclosed by a differential ΔP. For a two-dimensional Gaussian distribution the occupied area is independent of the value for P.

Gaussian Approximation for the Directional Probability

To facilitate the later stages of the analysis of an event, it is helpful to approximate the results of the computations of P(x,y) by a pure Gaussian distribution which may be expressed in terms of a few parameters: x_o, y_o, a 2X2 error matrix, and a normalization constant. One may recall that this simplifying approach was used earlier in approximating the exponentiated noise distribution. The derived parameters may later be incorporated into a straightforward mathematical formalism for evaluating a joint probability function for shower paths based on a collection of observations.

The least squares fitting is accomplished by sampling, together with the appropriate x and y coordinates, the logarithm of P in areas where it is not a large negative value. This sampling is done over a grid corresponding to the printout from the computer; that is, as the computer calculates the values for ℓn P (hereafter referred to as U) to be printed out on the map of the sky, it saves these values for the fitting (e.g. all numbers above -100 in Figure 9.4). Some advantage may be gained in modifying the least squares calculation by including a weight factor proportional to P for the errors in W, the log of the new approximating function, which are to be minimized. Specifically we could require that if E_i represents the disagreement between W and a measurement of U, and P_i is the actual probability value, the extremum for the total error is found by setting

$$\frac{\partial \sum E_i^2 P_i}{\partial a_j} = 0 \quad \text{for } j = 1 \text{ to } 6 \tag{9.21}$$

where a_j is any one of six parameters describing W. The weight factor allows us to obtain a better fit to U in the region where P is significant. Naturally the more desirable fitting for large P is done at the expense of accuracy for regions where P is of negligible value. The weighting also helps to offset a tendency to overemphasize the measurements of low P since they are more numerous in the sampling grid. For the moment let W be expressed in the form

$$W = a_1x^2 + a_2y^2 + a_3xy + a_4x + a_5y + a_6 \tag{9.22}$$

Since $E_i = U_i - W(x_i,y_i)$, Equation (9.21) may be expressed as

$$\frac{\partial \sum (U_i - W)^2 P_i}{\partial a_j} = -2\sum P_i (U_i - W)\frac{\partial W}{\partial a_j} = 0$$

or

$$\sum P_i W \frac{\partial W}{\partial a_j} = \sum P_i U_i \frac{\partial W}{\partial a_j} \tag{9.23}$$

where W and its derivatives are evaluated at x_i,y_i in each case. The explicit forms of Equation (9.23) which are to be solved are given in Table 9.1.

After the coefficients a_1 to a_6 have been determined, the expression for W may be recast into the more meaningful form suggested earlier

$$W = k - \tfrac{1}{2} G_{11}(x-x_o)^2 - \tfrac{1}{2} G_{22}(y-y_o)^2 - G_{12}(x-x_o)(y-y_o) \tag{9.24}$$

similar to the manner in which Equation (9.6) was expressed.

$$a_1\Sigma P_i x_i^4 + a_2\Sigma P_i x_i^2 y_i^2 + a_3\Sigma P_i x_i^3 y_i + a_4\Sigma P_i x_i^3 + a_5\Sigma P_i x_i^2 y_i + a_6\Sigma P_i x_i^2 = \Sigma P_i U_i x_i^2$$

$$a_1\Sigma P_i x_i^2 y_i^2 + a_2\Sigma P_i y_i^4 + a_3\Sigma P_i x_i y_i^3 + a_4\Sigma P_i x_i y_i^2 + a_5\Sigma P_i y_i^3 + a_6\Sigma P_i y_i^2 = \Sigma P_i U_i y_i^2$$

$$a_1\Sigma P_i x_i^3 y_i + a_2\Sigma P_i x_i y_i^3 + a_3\Sigma P_i x_i^2 y_i^2 + a_4\Sigma P_i x_i^2 y_i + a_5\Sigma P_i x_i y_i^2 + a_6\Sigma P_i x_i y_i = \Sigma P_i U_i x_i y,$$

$$a_1\Sigma P_i x_i^3 + a_2\Sigma P_i x_i y_i^2 + a_3\Sigma P_i x_i^2 y_i + a_4\Sigma P_i x_i^2 + a_5\Sigma P_i x_i y_i + a_6\Sigma P_i x_i = \Sigma P_i U_i x_i$$

$$a_1\Sigma P_i x_i^2 y_i + a_2\Sigma P_i y_i^3 + a_3\Sigma P_i x_i y_i^2 + a_4\Sigma P_i x_i y_i + a_5\Sigma P_i y_i^2 + a_6\Sigma P_i y_i = \Sigma P_i U_i y_i$$

$$a_1\Sigma P_i x_i^2 + a_2\Sigma P_i y_i^2 + a_3\Sigma P_i x_i y_i + a_4\Sigma P_i x_i + a_5\Sigma P_i y_i + a_6\Sigma P_i n = \Sigma P_i U_i$$

Table 9.1. Six simultaneous equations represented by Equation (9.23) for j = 1 to 6. All summations are over the index i for n measurements.

Equation (9.24) is equivalent to Equation (9.22) if we specify that

$$G_{11} = -2a_1; \quad G_{22} = -2a_2; \quad G_{12} = -a_3 \qquad (9.25\ a,b,c)$$

and solve for x_o and y_o from the simultaneous equations

$$\begin{aligned} G_{11}x_o + G_{12}y_o &= a_4 \\ G_{12}x_o + G_{22}y_o &= a_5 \end{aligned} \qquad (9.26\ a,b)$$

Although it would follow that

$$k = a_6 + \frac{1}{2} G_{11}x_o^2 + \frac{1}{2} G_{22}y_o^2 + G_{12}x_o y_o \qquad (9.27)$$

one should recall that P has not been normalized, and hence the formulation of k shown above, which determines a multiplicative constant for the best fit probability function, is of no significance. At this point we may determine k on the basis of the requirement that

$$\int_{-\infty}^{\infty}\int_{-\infty}^{\infty} \exp(W)\,dxdy = 1. \qquad (9.28)$$

The integral is easily solved if it is carried out in a rotated coordinate system whose origin is at x_o, y_o. The rotation is such that the cross term G_{12} drops out under the transformation. The integral is then separable into the product of two error functions integrated from $-\infty$ to $+\infty$

$$\begin{aligned} \int_{-\infty}^{\infty}\int_{-\infty}^{\infty} \exp(W)\,dxdy &= k \int_{-\infty}^{\infty} \exp\left[-\frac{1}{2} G'_{11}x'\right] dx' \int_{-\infty}^{\infty} \exp\left[-\frac{1}{2} G'_{22}y'\right] dy' \\ &= 2\pi k\, G'_{11}{}^{-1/2}\, G'_{22}{}^{-1/2} \end{aligned} \qquad (9.29)$$

where the primes refer to the transformed variables. Following an argument presented earlier (associated with Equation 9.9) we may say

$$k = \frac{|G|^{1/2}}{2\pi} \tag{9.30}$$

The new probability function exp(W)dydx may be visualized as an elliptical Gaussian hill of height k centered on x_o, y_o. The G terms give us an interpretation of the size and shape of the hill. More precisely, the semiaxes of an elliptical contour representing one standard deviation are

$$r_1, r_2 = \frac{1}{2}(G_{11} + G_{22}) \pm \sqrt{\frac{1}{4}(G_{11} + G_{22})^2 - G_{11}G_{22} + G_{12}^2} \tag{9.31}$$

The angle of an axis of the ellipse with respect to the x axis is determined by

$$\tan 2\theta = 2G_{12}/(G_{11} - G_{22}) \tag{9.32}$$

For the probability treatment which will follow, the new probability function shall be referred to as P(x,y) with the understanding that it is an approximation to the actual P(x,y) derived earlier.

Before we explore the next stage of the shower analysis, brief mention should be made concerning a circumstance under which the directional accuracy of a reading may be higher than usual. Occasionally one would be fortunate enough to have an event where the shower impact on the earth is observable --that is, the intensity has not appreciably decreased before there is an abrupt cessation of the signal (an example of this situation may be seen by looking ahead to Figure 12.3c: north

channel). In such a case one may categorically state that at the precise instant the signal dropped off the light was coming from the horizon. It is therefore possible to eliminate the uncertainty in direction perpendicular to the horizon, and in effect one is left with a thin, one-dimensional probability distribution extending along the horizon instead of the usual nearly circular two-dimensional distribution.

X. PLANE OF BEST FIT DETERMINATION (TIME INDEPENDENT ANALYSIS)

We may recall that any rectilinear shower trajectory will trace a great circle on the sphere describing apparent directions for an observer at the center. This great circle represents the intersection of the sphere with a plane containing the shower line and the observing station. Before formulating a method of resolving the plane for a shower event, we must first acquaint ourselves with the nature of the family of arcs representing all great circles in the coordinate system we have adopted.

It is an interesting property of the stereographic projection that all circles on the surface of the sphere map into circles on the plane, although there may be considerable misrepresentation of size, and concentric circles need not remain concentric after the mapping. This rule of course applies to great circles as well, and it is necessary at this point to ascertain what properties distinguish the delineations of great circles from those of ordinary circles.

It is appropriate to depict a plane in terms of a unit vector which is perpendicular to the plane. Suppose, for the moment, that such an orthogonal vector were pointing east at an angle θ_m above the horizon (see Figure 6.3). The great circle would trace an ellipse in α,β space which would obey the parametric equations

$$\alpha = \sin\theta_m \cos\psi$$
$$\beta = \sin\psi \qquad (10.1\ a,b,c)$$
$$(\gamma = -\cos\theta_m \cos\psi)$$

where ψ is the angle with respect to the α axis of a point on the surface of the ellipse. Substituting Equations (10.1 a,b,c) into Equations (9.1i a,b) we obtain for the stereographic projection

$$x = \frac{2\sin\theta_m \cos\psi}{1 - \cos\theta_m \cos\psi} \quad ; \quad y = \frac{2\sin\psi}{1 - \cos\theta_m \cos\psi} \qquad (10.2\ a,b)$$

which should satisfy the equation of a circle:

$$(x - x_o)^2 + y^2 = k^2 \qquad (10.3)$$

The quantities k and x_o respectively refer to the circle's radius and the position of its center. The north-south symmetry makes it evident that the center of the circle must lie on the x axis, and hence there is no term in y_o. Combining Equations (10.2 a,b) with Equation (10.3) we get

$$\left(\frac{2\sin\theta_m \cos\psi}{1 - \cos\theta_m \cos\psi} - x_o\right)^2 + \left(\frac{2\sin\psi}{1 - \cos\theta_m \cos\psi}\right)^2 = k^2 \qquad (10.4)$$

which, after multiplying by $(1 - \cos\theta_m\cos\psi)^2$ and squaring the terms, reduces to

$$\begin{aligned} &4\sin^2\theta_m\cos^2\psi + x_o^2 + x_o^2\cos^2\theta_m\cos^2\psi - 4x_o\sin\theta_m\cos\psi \\ &+ 4x_o\sin\theta_m\cos\theta_m\cos^2\psi - 2x_o^2\cos\theta_m\cos\psi + 4\sin^2\psi - k^2 \\ &+ 2k^2\cos\theta_m\cos\psi - k^2\cos^2\theta_m\cos^2\psi = 0 \end{aligned} \qquad (10.5)$$

Since the above equation must hold for any value of ψ, we separate the terms according to their dependence on $\cos\psi$ and

require the following equalities to hold:

$$\cos^2\psi: \quad 4\sin^2\theta_m + x_o^2\cos^2\theta_m + 4x_o\sin\theta_m\cos\theta_m - 4 - k^2\cos^2\theta_m = 0$$

$$\text{or} \quad (2\sin\theta_m + x_o\cos\theta_m)^2 - 4 - k^2\cos^2\theta_m = 0$$

$$\cos\psi: \quad -4x_o\sin\theta_m - 2x_o^2\cos\theta_m + 2k^2\cos\theta_m = 0$$

$$\psi \text{ independent:} \quad x_o^2 + 4 - k^2 = 0 \qquad (10.6\ a,b,c)$$

Any two equations from (10.6) establish that

$$x_o = 2\cot\theta_m \ ; \quad x_o^2 + 4 = k^2 \qquad (10.7\ a,b)$$

The third equation is redundant and serves as a check. The geometrical interpretation of the foregoing relations is depicted by the first two examples given in Figure 10.1. The argument just presented may be generalized for an arc representing an orthogonal vector pointing in a direction other than east by considering a rotation in azimuth about the origin of the type of curve obtained above. Figure 10.1c shows the case for an orthogonal vector pointing north of east.

Any point on the x,y diagram may be expressed in terms of a coordinate system based on an interpretation of position on a particular great circle. If we adopt a coordinate system as shown in Figure 10.1c then for ϕ equal to zero any point on the arc is given by

$$x' = 2\cot\theta_m - 2\csc\theta_m\cos\theta$$

$$y' = 2\csc\theta_m\sin\theta \qquad (10.8\ a,b)$$

The rotation by an angle ϕ of the point (x',y') gives the new

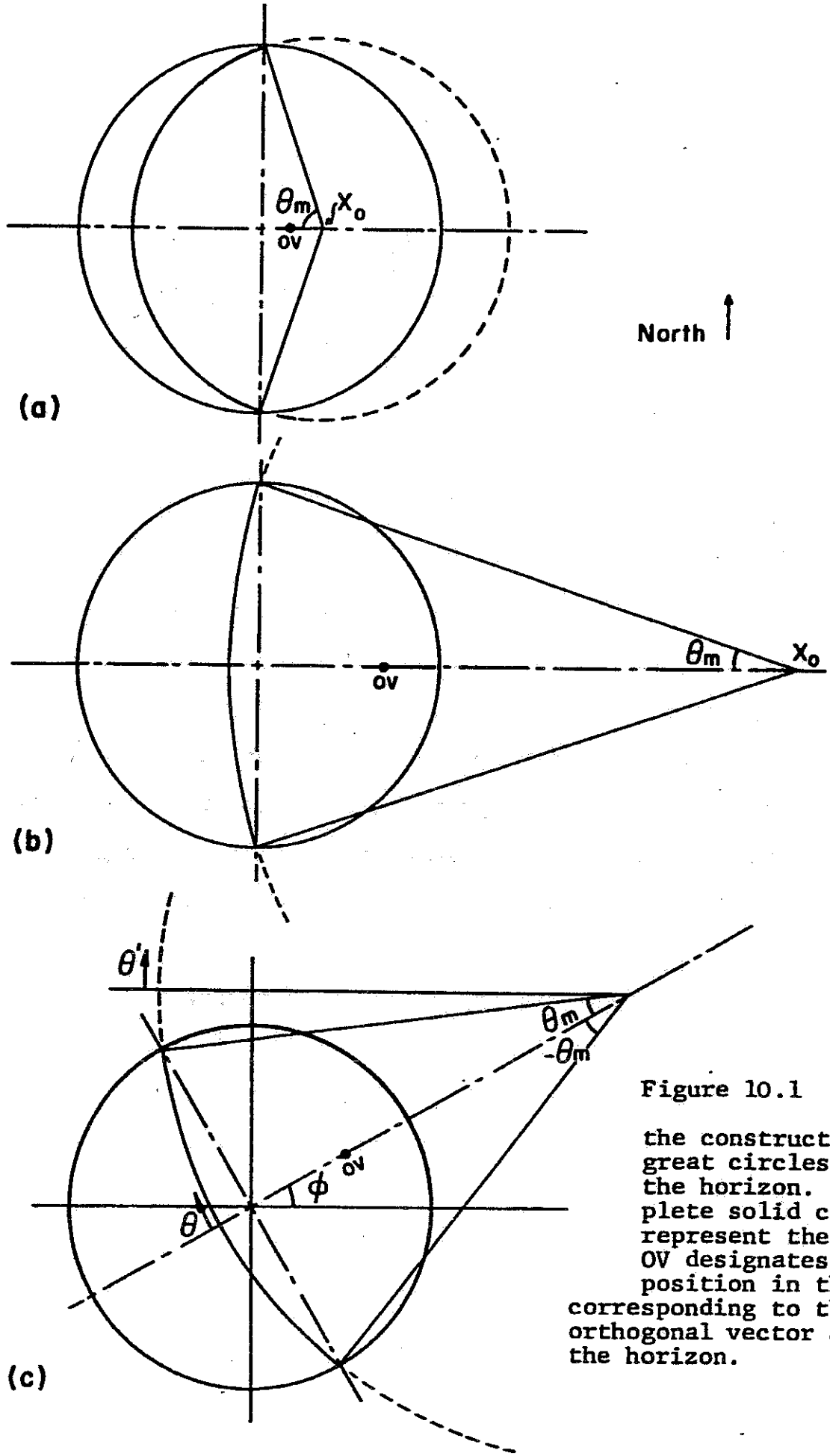

Figure 10.1 Examples showing the construction of great circles above the horizon. The complete solid circles represent the horizon. OV designates the position in the sky corresponding to the orthogonal vector above the horizon.

coordinates

$$x = x'\cos\phi - y'\sin\phi$$

$$y = x'\sin\phi + y'\cos\phi \qquad (10.9\ a,b)$$

Combining Equations (10.8) and (10.9) yields for the general case

$$x = 2\cot\theta_m\cos\phi - 2\csc\theta_m\cos\phi\cos\theta - 2\csc\theta_m\sin\phi\sin\theta$$

$$y = 2\cot\theta_m\sin\phi - 2\csc\theta_m\sin\phi\cos\theta + 2\csc\theta_m\cos\phi\sin\theta$$

$$0 \leq \theta_m \leq \frac{\pi}{2} \qquad (10.10\ a,b)$$

Varying the angle θ allows one to select the x,y coordinates of any point on the plane specified by θ_m and ϕ.

Now that the basic character of the arcs corresponding to great circles has been identified, it is necessary to derive a method of determining some measure of the probability that, at the time a particular reading was made, the light was coming from a direction arbitrarily close to a given plane. The probability for such a plane may be assigned on the basis of a summation over a sampling of the probability function P at many points (different θ) along the arc. This summation may, of course, be expressed as an integral over θ for a fixed value of θ_m and ϕ. Inasmuch as we have the <u>a priori</u> information that the source direction is never below the horizon we may establish the limits of integration to be from $-\theta_m$ to $+\theta_m$. Since it is desired to construct a new probability function describing the relative chance that the orthogonal vector is contained within some small solid angle $d\Omega$ centered on θ_m and ϕ, for each sample at a given θ we must multiply P by the

Jacobian $\frac{\partial(x,y)}{\partial\Omega} = \frac{\partial(x,y)}{\partial(\sin\theta_m,\phi)}$.

In formulating the Jacobian it is wise to define a new angle θ' which is equal to $\theta - \phi$ since the interpretation of both θ and ϕ becomes ambiguous as θ_m approaches $\frac{\pi}{2}$, whereas the difference of these angles is always clearly defined (see Figure 10.1). In terms of θ' the variables x and y may be expressed in the form

$$x = 2\cot\theta_m\cos\phi - 2\csc\theta_m\cos\theta'$$
$$y = 2\cot\theta_m\sin\phi + 2\csc\theta_m\sin\theta' \qquad (10.11\ a,b)$$

Using the relationships

$$\frac{d\ \cot\theta_m}{d\ \sin\theta_m} = -\csc^2\theta_m\sec\theta_m \ ; \quad \frac{d\ \csc\theta_m}{d\ \sin\theta_m} = -\csc^2\theta_m \qquad (10.12\ a,b)$$

we find

$$J = \left| \frac{\partial x}{\partial\sin\theta_m}\frac{\partial y}{\partial\phi} - \frac{\partial y}{\partial\sin\theta_m}\frac{\partial x}{\partial\phi} \right|$$

$$J = \left| -4\csc^2\theta_m\left\{(\sec\theta_m\cos\phi-\cos\theta')(\cot\theta_m\cos\phi) - (\sec\theta_m\sin\phi+\sin\theta')(-\cot\theta_m\sin\phi)\right\}\right|$$

$$J = \left|-4\csc^2\theta_m\left\{\sec\theta_m\cot\theta_m - \cot\theta_m\cos(\theta'+\phi)\right\}\right|$$

$$J = 4\csc^3\theta_m(1 - \cos\theta_m\cos\theta) \qquad (10.13)$$

Hence the integral has the form

$$\ell = 4\csc^3\theta_m\int_{-\theta_m}^{\theta_m} P(\theta_m,\phi,\theta)(1-\cos\theta_m\cos\theta)\,d\theta \qquad (10.14)$$

The value of J approaches infinity in proportion to $\frac{1}{\theta_m}$ as θ_m approaches zero. This behavior is entirely reasonable since the limits of integration correspondingly approach zero with

the same rapidity.

As soon as the probability $\ell(\theta_m,\phi)$ has been evaluated for each reading it will be possible to assign a probability that the line of an entire event conforms to the plane. The latter probability may be interpreted as the joint probability that every reading was a measurement of a light signal emanating from some apparent direction on the plane in question. This composite probability may be expressed as the product for n readings

$$L = \prod_{i=1}^{n} \ell_i \qquad (10.15)$$

since the errors for the different readings are mutually independent (provided that the time between readings is longer than the amplifier rise time).

One should note that the probability interpretation just presented makes no use of information regarding consecutive angular positions on any plane. We are merely testing the conformity of the collection of readings to some straight line in the sky. The sequential character of the event will be investigated in a later phase of the analysis.

An interesting consequence of allowing the integration to be performed only above the horizon arises in the character of L for nearly horizontal showers. If we consider a limiting case of two orthogonal vectors whose ϕ values differ by 180° and whose θ_m is nearly 90°, we find that although the physical separation of the vectors is small the paths of integration go

through markedly different regions of the sky. This results in the possibility of there existing an abrupt discontinuity in L in the orthogonal vector space at the zenith--an idea which at first may seem physically untenable. This peculiar mathematical behavior results from the fact that the shielding effect of the earth (not permitting showers to be visible underground) exhibits a sharp cutoff in discriminating against certain trajectories. For instance, the observation of a nearly horizontal shower to the west may give an L distribution which is somewhat broad in a region slightly east of the zenith but which drops off precipitously at the zenith on the westward side.

Solution of the Line Integral Across the Sky

The logarithm of the approximate Gaussian formulation of the light source directional probability function $P(x,y)$ as expressed in Equation (9.24) must now be redefined in terms of θ_m, ϕ, and θ. With the aid of Equation (10.10) we obtain

$$\begin{aligned} -W = {} & \tfrac{1}{2} G_{11}(2\cot\theta_m\cos\phi - 2\csc\theta_m\cos\phi\cos\theta + 2\csc\theta_m\sin\phi\sin\theta - x_o)^2 \\ & + \tfrac{1}{2} G_{22}(2\cot\theta_m\sin\phi - 2\csc\theta_m\sin\phi\cos\theta + 2\csc\theta_m\cos\phi\sin\theta - y_o)^2 \\ & + G_{12}(2\cot\theta_m\cos\phi - 2\csc\theta_m\cos\phi\cos\theta - 2\csc\theta_m\sin\phi\sin\theta - x_o) \\ & (2\cot\theta_m\sin\phi - 2\csc\theta_m\sin\phi\cos\theta + 2\csc\theta_m\cos\phi\sin\theta - y_o) - k \end{aligned} \qquad (10.16)$$

After the above expressions have been multiplied out, the resulting terms may be grouped according to their dependence on θ (the following expressions have their θ dependent

functions factored out):

$$\underline{\text{independent of } \theta}: \quad 2G_{11}\left(\cot^2\theta_m\cos^2\phi + \frac{x_o^2}{4} - x_o\cot\theta_m\cos\phi\right)$$
$$+ 2G_{22}\left(\cot^2\theta_m\sin^2\phi + \frac{y_o^2}{4} - y_o\cot\theta_m\sin\phi\right)$$
$$+ 2G_{12}\left(2\cot^2\theta_m\sin\phi\cos\phi + \frac{1}{2}x_oy_o - x_o\cot\theta_m\sin\phi - y_o\cot\theta_m\cos\phi\right) - k \tag{10.17a}$$

$$\underline{\sin\theta}: \quad 2G_{11}\left(-2\cot\theta_m\csc\theta_m\sin\phi\cos\phi + x_o\csc\theta_m\sin\phi\right)$$
$$+ 2G_{22}\left(2\cot\theta_m\csc\theta_m\sin\phi\cos\phi - y_o\csc\theta_m\cos\phi\right)$$
$$+ 2G_{12}\left(2\csc\theta_m\cot\theta_m\cos^2\phi - 2\csc\theta_m\cot\theta_m\sin^2\phi - x_o\csc\theta_m\cos\phi\right.$$
$$\left. + y_o\csc\theta_m\sin\phi\right) \tag{10.17b}$$

$$\underline{\cos\theta}: \quad 2G_{11}\left(-2\cot\theta_m\csc\theta_m\cos^2\phi + x_o\csc\theta_m\cos\phi\right)$$
$$+ 2G_{22}\left(-2\cot\theta_m\csc\theta_m\sin^2\phi + y_o\csc\theta_m\sin\phi\right)$$
$$+ 2G_{12}\left(-2\csc\theta_m\cot\theta_m\sin\phi\cos\phi - 2\csc\theta_m\cot\theta_m\sin\phi\cos\phi\right.$$
$$\left. + x_o\csc\theta_m\sin\phi + y_o\csc\theta_m\cos\phi\right) \tag{10.17c}$$

$$\underline{\sin\theta\cos\theta}: \quad 4G_{11}\csc^2\theta_m\sin\phi\cos\phi - 4G_{22}\csc^2\theta_m\sin\phi\cos\phi$$
$$+ 4G_{12}\left(-\csc^2\theta_m\cos^2\phi + \csc^2\theta_m\sin^2\phi\right) \tag{10.17d}$$

$$\underline{\cos^2\theta}: \quad 2G_{11}\csc^2\theta_m\cos^2\phi + 2G_{22}\csc^2\theta_m\sin^2\phi$$
$$+ 4G_{12}\csc^2\theta_m\sin\phi\cos\phi \tag{10.17e}$$

$$\underline{\sin^2\theta}: \quad 2G_{11}\csc^2\theta_m\sin^2\phi + 2G_{22}\csc^2\theta_m\cos^2\phi$$
$$- 4G_{12}\csc^2\theta_m\sin\phi\cos\phi \tag{10.17f}$$

To facilitate a series expansion of W it is desirable to re-express the (10.17 d,e,f) terms according to their dependence

on 2θ. Since $\cos^2\theta = \frac{\cos2\theta + 1}{2}$ and $\sin^2\theta = \frac{1 - \cos2\theta}{2}$ we may add $\frac{1}{2}\cos^2\theta$ term + $\frac{1}{2}\sin^2\theta$ term to the constant term (10.17a) and let the $\cos2\theta$ term equal $\frac{1}{2}\cos^2\theta$ term - $\frac{1}{2}\sin^2\theta$ term giving

<u>independent of θ</u>: (term 10.17a) + $(G_{11} + G_{22})\csc^2\theta_m$ (10.18a)

<u>$\cos2\theta$</u>: $(G_{11} - G_{22})\csc^2\theta_m(\cos^2\phi - \sin^2\phi)$

$$+ 4G_{12}\csc^2\theta_m\sin\phi\cos\phi \qquad (10.18b)$$

Likewise the $\sin\theta\cos\theta$ term may be replaced by

<u>$\sin2\theta$</u>: $2(G_{11} - G_{22})\csc^2\theta_m\sin\phi\cos\phi + 2G_{12}\csc^2\theta_m(\sin^2\phi - \cos^2\phi)$ (10.19)

because of the fact that $\sin\theta\cos\theta = \frac{\sin2\theta}{2}$.

In the interest of brevity the expressions related to the different functions of θ shall be designated by the letter F followed by a subscript designating the function involved. The following equivalence relationships hold:

$F_1 \equiv \theta$ independent term (10.18a)

$F_2 \equiv \sin\theta$ term (10.17b)

$F_3 \equiv \cos\theta$ term (10.17c)

$F_4 \equiv \sin2\theta$ term (10.19)

$F_5 \equiv \cos2\theta$ term (10.18b)

To expedite numerical computation and reveal more clearly the similarity of the different terms, the expressions referred to above may be simplified somewhat from the forms given in (10.17) to (10.19). If we let

$$C_x = 2\cot\theta_m\cos\phi - x_o \tag{10.20a}$$

$$C_y = 2\cot\theta_m\sin\phi - y_o \tag{10.20b}$$

$$C_s = \csc\theta_m\sin\phi \tag{10.20c}$$

$$C_c = \csc\theta_m\cos\phi \tag{10.20d}$$

then

$$F_1 = G_{11}\left(\frac{C_x^2}{2} + C_s^2 + C_c^2\right) + G_{22}\left(\frac{C_y^2}{2} + C_s^2 + C_c^2\right) + G_{12}C_xC_y - k \tag{10.21a}$$

$$F_2 = -2G_{11}C_sC_x + 2G_{22}C_cC_y + 2G_{12}(C_cC_x - C_sC_y) \tag{10.21b}$$

$$F_3 = -2G_{11}C_cC_x - 2G_{22}C_sC_y - 2G_{12}(C_sC_x + C_cC_y) \tag{10.21c}$$

$$F_4 = 2(G_{11} - G_{22})C_sC_c + 2G_{12}(C_s^2 - C_c^2) \tag{10.21d}$$

$$F_5 = (G_{11} - G_{22})(C_c^2 - C_s^2) + 4G_{12}C_sC_c \tag{10.21e}$$

The expression

$$\exp(W) = \exp(-F_1 - F_2\sin\theta - F_3\cos\theta - F_4\sin2\theta - F_5\cos2\theta) \tag{10.22}$$

may be expanded into a collection of power series in θ within an exponential

$$\begin{aligned}\exp(W + F_1) = \exp\Big(&-F_2\theta + \frac{F_2\theta^3}{3!} - \frac{F_2\theta^5}{5!} + \ldots \\ &- F_3 + \frac{F_3\theta^2}{2!} - \frac{F_3\theta^4}{4!} + \ldots \\ &- 2F_4\theta + 2^3\frac{F_4\theta^3}{3!} - 2^5\frac{F_4\theta^5}{5!} + \ldots \\ &- F_5 + 2^2\frac{F_5\theta^2}{2!} - 2^4\frac{F_5\theta^4}{4!} + \ldots\Big)\end{aligned} \tag{10.23}$$

which may be regrouped into the form

$$\exp(W + F_1) = \exp\left(- \frac{F_3+2^0F_5}{0!} - \frac{F_2+2^1F_4}{1!}\theta + \frac{F_3+2^2F_5}{2!}\theta^2 + \frac{F_2+2^3F_4}{3!}\theta^3 - \frac{F_3+2^4F_5}{4!}\theta^4 - \frac{F_2+2^5F_4}{5!}\theta^5 + \ldots \right) \qquad (10.24)$$

Again for convenience, we may further condense the notation by re-expressing Equation (10.24) in the form

$$\exp(W+F_1) = \exp(g_0 + g_1\theta + g_2\theta^2 + g_3\theta^3 + \ldots) \qquad (10.25)$$

The exponential in the right half of Equation (10.25) may be expanded in a Taylor series to give purely a power series in θ. The power series for the exponential may, in turn, be multiplied by the series representing $(1 - \cos\theta_m\cos\theta)$ to give a series in θ which may be integrated term by term. Under certain conditions however, the exponential series may be quite slow to converge, and the evaluation of high powers of the expression within the exponential may become exceedingly cumbersome. It was estimated that a prohibitive number of multiplications would have been necessary to determine the coefficients for the final series in θ giving a reasonable accuracy for the worst conditions of convergence which one might expect to encounter. The poor convergence may be generally expected to occur when the significant part of P is confined to a small portion of the entire arc from horizon to horizon. It was considered desirable, therefore, to split up the integral into a number of small ranges of integration to be carried out only within the region where P had a value which

was not negligible. This procedure is, in effect, a compromise between a one-shot integration over the entire range and a brute force numerical integration method which would also be burdensome for the computer.

The section of the computer program which evaluates the integral divides the significant portion of the arc (which could be as large as $2\theta_m$ in some cases) into ten equal intervals. Each small integral for an interval is evaluated in terms of a new variable of integration θ' where

$$\theta' = \theta - \theta_o \,. \tag{10.26}$$

θ_o is defined to be the value of θ at the center of the interval thus simplifying each small integral by making it dependent on only the even terms in the power series expansion in θ'. Equation (10.25) may be rewritten in terms of θ' by substituting the expression $(\theta' + \theta_o)$ for θ.

$$\exp(W) = \exp(g_0 - F_1)\exp\{g_1(\theta'+\theta_o) + g_2(\theta'+\theta_o)^2 + g_3(\theta'+\theta_o)^3 + \ldots + g_{max}(\theta'+\theta_o)^{max}) \tag{10.27}$$

The subscript max refers to the largest subscript necessary to insure a specific accuracy desired in the calculation. However since

$$(\theta'+\theta_o)^n = \theta'^n + C_{n,1}\theta'^{n-1}\theta_o + C_{n,2}\theta'^{n-2}\theta_o^2 + \ldots C_{n,n-1}\theta'\theta_o^{n-1} + \theta_o^n \tag{10.28}$$

($C_{n,m}$ is a binomial coefficient: $\frac{n!}{(n-m)!\,m!}$) we may alternately use the expression

$$\exp(W) = \exp(g_0' - F_1)\exp(g_1'\theta' + g_2'\theta'^2 + g_3'\theta'^3 + \ldots g_{max}\theta'^{max}) \tag{10.29}$$

where

$$g_m' = \sum_{n=m}^{max} C_{n,n-m} g_n \theta_o^{n-m} = \sum_{n=m}^{max} C_{n,m} g_n \theta_o^{n-m} \tag{10.30}$$

The first several terms in the Taylor series expansion about the center of each small integration interval are shown in Table 10.1. Each term is to be multiplied by the appropriate reciprocal factorial and power of θ' heading each row and column. To save computation time the computer program contains instructions to determine the minimum number of g' terms and the number of exponentiated Taylor series terms necessary to achieve a desired accuracy.

The expansion for the exponential is next multiplied by the series in θ' representing the expression $(1 - \cos\theta_m\cos\theta)$. The latter series is determined by transforming the series $(1 - \cos\theta_m) + \cos\theta_m(\frac{\theta^2}{2!} - \frac{\theta^4}{4!} + \frac{\theta^6}{6!} - \ldots)$ according to the scheme given in Equation (10.30).

If the final series (after multiplication) is of the form $G_o + G_1\theta' + G_2\theta'^2 + G_3\theta'^3 + \ldots$, the expression in Equation (10.14) integrated over the narrow interval of width $2\Delta\theta$ centered on θ_o is given by

$$4\csc^3\theta_m \int_{-\Delta\theta}^{\Delta\theta} \exp\left[W(\theta')\right](1-\cos\theta_m\cos\theta)\,d\theta' = 8\csc^3\theta_m \exp(g_o' - F_1) \sum_{i=0}^{i_{max}} \frac{G_{2i}}{2i+1}(\Delta\theta)^{2i+1} \tag{10.31}$$

	θ'^0	θ'^1	θ'^2	θ'^3	θ'^4	θ'^5	θ'^6	θ'^7	θ'^8, etc.
$\frac{1}{0!}$	1								
$+\frac{1}{1!}$		g_1'	g_2'	g_3'	g_4'	g_5'	g_6'	g_7'	...
$+\frac{1}{2!}$			$g_1'^2$	$2g_1'g_2'$	$2g_1'g_3' + g_2'^2$	$2g_1'g_4' + 2g_2'g_3'$	$2g_1'g_5' + 2g_2'g_4' + g_3'^2$	$2g_1'g_6' + 2g_2'g_5' + 2g_3'g_4'$	...
$+\frac{1}{3!}$				$g_1'^3$	$3g_1'^2g_2'$	$3g_1'^2g_3' + 3g_1'g_2'^2$	$3g_1'^2g_4' + 6g_1'g_2'g_3' + g_2'^3$	$2g_1'^2g_5' + 6g_1'g_2'g_4' + 3g_1'g_3'^2 + 3g_2'^2g_3'$	...
$+\frac{1}{4!}$					$g_1'^4$	$4g_1'^3g_2'$	$3g_1'^3g_3' + 6g_1'^2g_2'^2$	$3g_1'^3g_4' + 12g_1'^2g_2'g_3' + 4g_1'g_2'^3$	...
$+\frac{1}{5!}$						$g_1'^5$	$5g_1'^4g_2'$	$3g_1'^4g_3' + 10g_1'^3g_2'^2 + g_1'^4g_3'$	...
$+\frac{1}{6!}$							$g_1'^6$	$6g_1'^5g_2'$	...
$+\frac{1}{7!}$								$g_1'^7$	...

Table 10.1

Note that the odd powers of θ' give no contribution to the integral (and hence need not be computed) since the limits are symmetric with respect to θ_o.

The ten small integrals are added to give the integral over the entire arc, and this integral is, in turn, included in the product (Equation 10.15) which gives the net probability for all of the readings.

The computer is instructed to evaluate the probability for a variety of possible orthogonal vectors and print the values in a format identical to the output shown earlier for the instantaneous direction probabilities. An example of the appearance of a typical orthogonal vector distribution function may be seen in Figure 12.6 (page 176). We should recall from the nature of the Jacobian defined in Equation (10.13) that the numbers represent the logarithm (times ten) of the probability per unit solid angle, not per unit area in x and y.

XI. THE DETERMINATION OF POSITION ON A PLANE (TIME DEPENDENT ANALYSIS)

The discussion in Chapter VI outlined the fundamental relations between the observed angle versus time and the three unknowns θ_o, r_o, and t_o which define the geometrical configuration of a shower line along the plane of best fit. The discussion also pointed out the need for separating the analysis of these time dependent variables from the computations dealing with the evaluation of the best fit plane. We shall therefore restrict our attention to the changes in angle perpendicular to a particularly favorable orthogonal vector and assume that the results are sufficiently accurate for adjacent vectors.

In keeping with the spirit of the methods of interpretation which have been described up to now, it would be desirable to construct a probability distribution in the three parameters for a particular event. Naturally one would hope to be able to express the probability in terms of an error matrix describing the nature of the fall off for a three-dimensional Gaussian distribution centered on some most probable combination of θ_o, r_o, and t_o. This representation, unfortunately, proves to be inaccurate because the uncertainties in the quantities are large enough to invalidate any linear approximations for the errors in the trigonometric expression (Equation 6.1) describing the functional relationship of the variables. Upon actually evaluating the probability as a function of the three parameters we find that moments of higher order than the second moment play

a significant role in influencing the properties of the distribution.

On the other hand, since it is reasonable to assume that the sequential angular measurements have errors which are nearly Gaussian, it is permissible to represent in Gaussian form the probability's functional dependence on θ_o at fixed values of r_o and t_o. Loosely speaking, the quantity θ_o is directly related to an observable variable θ in Equation (6.1) whereas r_o and t_o are isolated from θ by the trigonometric functions. The probability may therefore be expressed in the simplified form

$$P(\theta_o, r_o, t_o) = \exp\left[k(r_o, t_o) - \frac{\left(\theta_o - \bar{\theta}_o(r_o, t_o)\right)^2}{2\sigma^2}\right] d\theta_o dr_o dt_o \tag{11.1}$$

We shall see later that the spread σ of θ_o about the most probable value $\bar{\theta}_o$ is independent of r_o and t_o.

In establishing a method of measuring the angle along a plane for each reading, let us first define a system of mutually orthogonal unit vectors $\vec{i}$, $\vec{j}$, and $\vec{k}$ such that $\vec{k}$ points along the plane's orthogonal vector, with the $\vec{i}$ and $\vec{j}$ vectors along the plane (see Figure 11.1). The vector $\vec{j}$ points upwards along the line of greatest elevation (the dot-dash line in Figure 6.3), and the $\vec{i}$ vector is horizontal. If α, β, and γ are the direction cosines of the orthogonal vector with respect to east, north, and up, then the unit vectors may be expressed in the form

$$\vec{i} = \left(\frac{-\beta}{\sqrt{1-\gamma^2}}, \frac{\alpha}{\sqrt{1-\gamma^2}}, 0 \right)$$

$$\vec{j} = \left(-\frac{\alpha\gamma}{\sqrt{1-\gamma^2}}, -\frac{\beta\gamma}{\sqrt{1-\gamma^2}}, \sqrt{1-\gamma^2} \right) \quad (11.2\ a,b,c)$$

$$\vec{k} = (\alpha, \beta, \gamma)$$

A rotation of $\vec{j}$ about $\vec{k}$ by an angle θ_z toward $\vec{i}$ is represented by

$$\vec{j}_{rot} = \vec{j} \cos\theta_z + \vec{i} \sin\theta_z$$

$$= \left(-\frac{\alpha\gamma\cos\theta_z + \beta\sin\theta_z}{\sqrt{1-\gamma^2}}, \frac{\alpha\sin\theta_z - \beta\gamma\cos\theta_z}{\sqrt{1-\gamma^2}}, \sqrt{1-\gamma^2}\cos\theta_z \right) \quad (11.3)$$

The coordinates for $\vec{j}_{rot}$ in the stereographic projection variables x and y are found by transforming according to formulas (9.11 a,b) the three components of Equation (11.3). We adopt θ_z, then, as a measure of angular displacement along the plane from the line closest to the zenith.

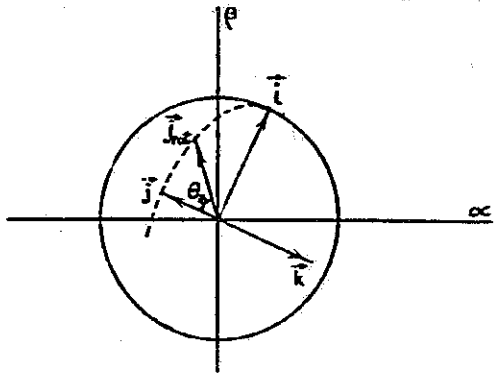

Figure 11.1

We have yet to resolve a two-fold ambiguity in the direction for the vector $\vec{i}$ which defines a direction for increasing θ_z. Instead of rigidly defining $\vec{i}$ to be either parellel or antiparallel to $\vec{j} \times \vec{k}$, the interpretation and description of the time dependent analysis is facilitated by specifying that $\vec{i}$ points toward the position of impact of the shower on the earth. It then follows that all showers are observed to have θ_z increase with time. This feature avoids confusion resulting from sign changes when Equation (6.1) is applied. Furthermore the requirement that no showers may travel upward may be translated into the restriction that the closest approach angle θ_o must have a θ_z value lying between zero and π.

The probability function P(x,y) defined in Equation (9.16) for a given reading may be sampled along a string of points in the sky representing small increments of θ_z between the limits $-\frac{\pi}{2}$ and $+\frac{\pi}{2}$. At each point we wish to find the probability that the reading is representative of a shower position which is confined within some infinitesimal angular band on either side of the plane and which is between θ_z and $\theta_z + d\theta_z$. This probability is equal to P(x,y) times the Jacobian $\frac{\partial(x,y)}{\partial()}$ which is defined in the following manner:

$$J = \frac{r\, dr\, d\phi}{\sin\theta d\theta d\phi} \qquad (11.4)$$

where θ^* in this case is the angle labeled as such in Figure

*Not to be confused with θ (appearing in Equation 6.1 and Equations 11.7 to 11.9) measured along the shower plane.

9.2, and $d\phi$ equals a differential rotation about the zenith. The construction in Figure 9.2 shows us that $\theta = 2\tan^{-1}\frac{r}{2}$ and hence

$$J = \frac{rdr}{\sin(2\tan^{-1}\frac{r}{2})\,d(2\tan^{-1}\frac{r}{2})} = \frac{rdr}{(\frac{4r}{4+r^2})(\frac{4dr}{4+r^2})} \qquad (11.5)$$

$$J = \frac{(4+r^2)^2}{16}$$

A least squares fitting of the quantity $\ln\left(J\ P(x,y)\right)$ for the many choices of θ_z establishes values for k_i, θ_i, and σ_i (all for the i^{th} reading) in the logarithm of the best fit Gaussian distribution

$$\ln\left(P_i(\theta_z)\right) \equiv w_i(\theta_z) = -\frac{1}{2}\left(\frac{\theta_i - \theta_z}{\sigma_i}\right)^2 + k_i \qquad (11.6)$$

As in the two-dimensional fitting of P(x,y) described earlier, better results are obtained if the squares of the errors to be minimized are weighted by $\left(J\ P(x,y)\right)$ (see Equation 9.21). Since, on the basis of past experience, we have had success in obtaining a satisfactory fit for the two-dimensional Gaussian approximation, it is reasonable to assume that $w_i(\theta_z)$ should be an accurate representation of the probability.

The net probability that all of the readings conform to a specific combination of θ_o, r_o, and t_o is equal to the product $\prod_i P_i(\theta_z)$, where each case designated by the subscript i has substituted for θ_z the expected angle which would be assumed if θ_o, r_o, and t_o were correct. It should be evident that θ_z equals the sum of θ_o and the angle $\theta(t_i,t_o,r_o)$ about the line

of closest approach (we shall solve for $\theta(t,t_o,r_o)$ in the next paragraph). The logarithm W of the combined probability shown in Equation (11.1) would therefore be given as

$$W = -\frac{1}{2}\sum_i \left(\frac{\theta_i - \theta_o - \theta(t_i,t_o,r_o)}{\sigma_i} \right)^2 + \sum_i k_i \qquad (11.7)$$

The most probable value $\bar{\theta}_o$ may be found by solving the equation

$$\frac{\partial W}{\partial \theta_o} = \sum \frac{\theta_i - \bar{\theta}_o - \theta(t_i,t_o,r_o)}{\sigma_i^2} \equiv 0 \qquad (11.8)$$

which yields

$$\bar{\theta}_o = \frac{\sum \frac{\theta_i - \theta(t_i,t_o,r_o)}{\sigma_i^2}}{\sum \frac{1}{\sigma_i^2}} \qquad (11.9)$$

Differentiating W again gives us the uncertainty σ in θ_o:

$$\sigma = \left(-\frac{\partial^2 W}{\partial \theta_o} \right)^{-1/2} = \left(\sum \frac{1}{\sigma_i} \right)^{-1/2} \qquad (11.10)$$

It is important to emphasize that σ represents the error in θ_o for fixed values of t_o and r_o. Since t_o and r_o are unknown, in actuality the uncertainty of θ_o is much larger than σ due to the fact that the value of $\bar{\theta}_o$ is strongly dependent on t_o and r_o. The height of the distribution's peak $k(r_o,t_o)$ is determined by evaluating Equation (11.7) at $\bar{\theta}_o$.

The solution for $\theta(t,t_o,r_o)$ may be obtained by finding the inverse of Equation (6.1). For convenience let us express the quantities independent of θ by the letter A. The slightly altered form of Equation (6.1)

$$A \equiv \frac{c(t - t_o)}{r_o} + 1 = \tan\theta + \sec\theta \qquad (11.11)$$

which is equivalent to

$$A \cos\theta = \sin\theta + 1 \qquad (11.12)$$

may be squared to give, after substituting $1 - \sin^2\theta$ for $\cos^2\theta$, a quadratic equation in $\sin\theta$.

$$(1 + A^2) \sin^2\theta + 2\sin\theta + 1 - A^2 = 0 \qquad (11.13)$$

The roots of the equation give

$$\sin\theta = \frac{-1 \pm A^2}{1 + A^2} \qquad (11.14)$$

where the plus sign is clearly the correct choice. It naturally follows that

$$\cos\theta = \frac{4A}{A^2 + 1} \qquad (11.15)$$

We should recall that A is never negative during an event since showers are not visible at times earlier than $\frac{r_o}{c}$ prior to the observed closest approach.

XII. SHOWER PULSE SIMULATION PROGRAM

At the time the pilot experiment was in the initial phase of operation, it was felt desirable to investigate in some detail the character of the signals which might be expected to register on the apparatus from showers with various specified energies and trajectories. Such an effort, it was felt, would aid in visually identifying pulses likely to be events. Initial rough estimates of pulse heights and lengths were calculated for a few shower combinations. It became increasingly clear however, as the computations were being worked out, that it was difficult to obtain by simple hand calculations an accurate picture of the pulse shapes to be expected to appear in each phototube signal channel since there were a large number of independent effects influencing in a complicated manner the instantaneous signal intensity. Any attempt to study in detail the pulse appearances would have to be accomplished by the use of a computer. The availability of a computer program, moreover, would encourage one to explore in greater depth the wide variety of event configurations which might be recorded.

In addition to performing a comprehensive survey of expected pulse forms for an assortment of shower conditions, the computer program was especially useful in producing mock events which could check on the performance and accuracy of the data reduction and analysis techniques described earlier. Successive readings from the simulated pulses, after having Gaussian distributed random numbers (representing the noise)

added, were used as input data to the reduction program for testing and evaluation purposes. After the method of analysis had been devised and checked out, a number of the computer simulated events were analyzed in an effort to gain some idea of how badly degraded the extracted information became as signals from small or distant showers became weaker. Together with the portrayal of a few examples of the simulated events which were run, the results of this study shall be discussed in a later section of this chapter.

The synthesis of the pulse forms is accomplished by first evaluating the number of photons received by each phototube from contiguous short elements of length Δs along the shower line. The light signal from each Δs segment is received within a small time interval whose limits are, say, t_1 and t_2. We may express the reception of the signal in terms of an intensity equal to the number of photons divided by $t_2 - t_1$ occurring at a time $(t_1 + t_2)/2$. The quantities t_1 and t_2 are evaluated at the end points of Δs according to the relation

$$t = \frac{r - s}{c} = \frac{(x^2 + y^2 + z^2)^{1/2} - s}{c} \qquad (12.1)$$

where x, y, and z are the coordinates (shown in Figure 12.1) of the point in question, and s is the distance above the ground along the shower axis. The choice governing the time at which t equals zero is arbitrary of course, and for Equation (12.1) the zero point in time corresponds to the instant the shower actually hits the earth (not when it is observed to hit).

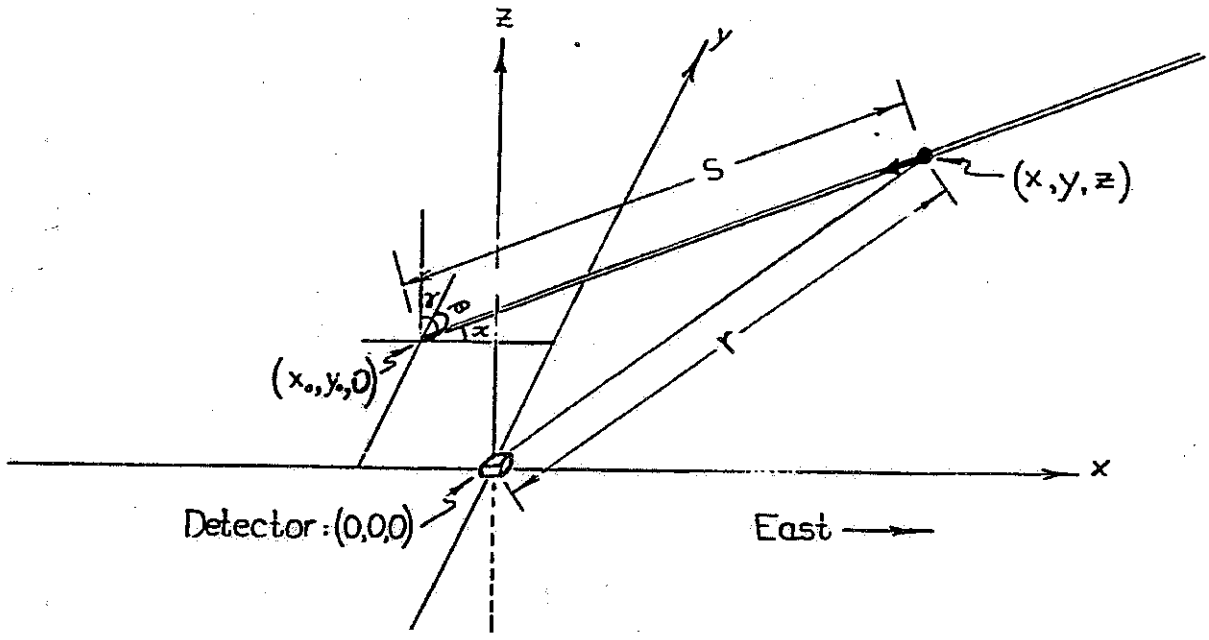

Figure 12.1

The variables which we may assign to a given shower are the following:

(a) Energy of the incoming primary.

(b) Direction cosines α, β of the shower axis with respect to the x and y axes (the z direction cosine γ equals the quantity $(1 - \alpha^2 - \beta^2)^{1/2}$).

(c) The location (x_o, y_o) of impact on the earth (at $z = 0$).

The instantaneous position of the shower front is related to s in the following manner (see Figure 12.1):

$$x = x_o + \alpha s$$
$$y = y_o + \beta s \qquad (12.2\ a,b,c)$$
$$z = \gamma s$$

The actual computational procedure starts by evaluating the pulse height for a Δs segment just above the impact point. The position s is then successively incremented by Δs, and new intensity values are calculated for the correspondingly earlier times. The rationale for constructing the pulses backwards in time is based on the fact that it is difficult to predict in advance at what height in the atmosphere the shower becomes visible to the detector. It is thus easiest to start from the ground, increase the altitude each time, and instruct the computer to discontinue calculating when the signal is completely lost in the noise.

Many of the effects governing the signal intensity registered by each phototube unit are strongly wavelength dependent. It is therefore necessary that a significant part of the computations be carried out for different λ separately and be included within a summation over each of the thirteen prominent spectrum lines listed in Table 3.1. The output signal voltage from the anode of a particular photomultiplier is given by the relation:

$$S = \frac{q\rho(z')N\Delta sAG\epsilon eR[1 - r(\theta)]\cos\theta}{4\pi(x^2+y^2+z^2)(t_2 - t_1)} \times \sum_{\lambda} \frac{D(\lambda)}{1 + \frac{p(z')}{p_o(\lambda)}\sqrt{\frac{293^\circ K}{T(z')}}} \exp\left[-a(\lambda)\ell(x,y,z)\right]\tau(\theta,\lambda) \tag{12.3}$$

where the different symbols are defined as follows:

q: The energy loss of a relativistic electron penetrating a given thickness of air; $q = \frac{2.24 \text{ Mev}}{\text{g/cm}^2}$.

$\rho(z')$: The density of the atmosphere as a function of altitude above sea level ($\rho = 0.1205 \frac{\text{g/cm}^2}{\text{m}}$ at STP). The altitude z' equals z plus the detection station's altitude H (1750 feet above sea level for the two stations).

N: The number of electrons present at the particular stage of shower growth.

A: The phototube area, 0.1 m^2.

G: The overall dynode gain for the phototube. Since there are twelve dynodes within the type of phototube being used, it may be said that the gain of each dynode is, on the average, $G^{.0833}$. As stated earlier, phototube gains have been known to vary considerably; a representative value of 9×10^4 has been chosen for the calculations.

ε: The peak phototube cathode efficiency which would be expected in the absence of any absorption in front of the photocathode (i.e. if I were equal to I_o in Equation 8.4), 11%.

e: The charge of an electron, 1.6×10^{-19} coul.

R: The value of the resistor between the last dynode and the anode of the phototube, 3.3 KΩ.

$r(\theta)$: The relative fraction of light reflected from the surface of the phototube unit. Equation (8.3) is the analytical expression for r in terms of θ.

θ: The incident angle of the light flux on the phototube unit face (i.e. the angle between the vectors $\vec{V}$ and $\vec{F}$ described earlier).

$D(\lambda)$: The transition excitation probability as defined in Equation (3.4).

$p_o(\lambda)$: The quenching pressure value as defined in Equation (3.3).

$p(z')$: The atmospheric pressure as a function of altitude above sea level.

$T(z')$: The temperature (°K) as a function of altitude above sea level.

$a(\lambda)$: The atmospheric absorption coefficient.

$\ell(x,y,z)$: The thickness of atmosphere between the point (x,y,z) and the origin (where the detector is located).

$\tau(\theta,\lambda)$: The relative transmission of the refracted beam which is equivalent to the evaluation of $\frac{I}{I_o}$ in Equation (8.4).

The atmospheric pressure $p(z')$ may be computed to sufficient accuracy by assuming, within certain altitude regions, that the temperature $T(z')$ is a linear function of altitude z'. Using the perfect gas law $p = \frac{\rho RT}{M}$, where M is the molecular weight of air (28.966) and R is the universal gas constant, the barometric equation $dp = -g\rho(z')dz'$ may be expressed in the form

$$dp = - \frac{gM}{R\ T(z')}\ p\ dz' \qquad (12.4)$$

We may integrate Equation (12.4) and evaluate explicitly $p(z')$ if we know the pressure p_o and the temperature T_o at the base z_o' of the region where $\frac{dT(z')}{dz'}$ is assumed to be constant:

$$\int_{p_o}^{p(z')} \frac{dp}{p} = -\frac{gM}{R}\int_{z'_o}^{z'} \frac{dz'}{T_o + \frac{dT}{dz'}(z' - z_o)} \qquad (12.5)$$

which has the solutions

$$\ln\left[\frac{p(z')}{p_o}\right] = -\frac{gM}{R(\frac{dT}{dz'})} \ln\left[\frac{T_o + (\frac{dT}{dz'})(z' - z'_o)}{T_o}\right] \; ; \; \frac{dT}{dz'} \neq 0$$

$$\ln\left[\frac{p(z')}{p_o}\right] = -\frac{gM(z' - z'_o)}{R\,T_o} \; ; \; \frac{dT'}{dz'} = 0 \qquad (12.6\ a,b)$$

The quantity $\frac{gM}{R}$ equals 0.003146 °K/m, and thus the final form for p(z') is

$$p(z') = p_o\left[\frac{T_o}{T_o + \frac{dT}{dz'}(z' - z'_o)}\right]^{\frac{.003146}{(\frac{dT}{dz'})}} \; ; \; \frac{dT}{dz'} \neq 0$$

$$p(z') = p_o \exp\left[\frac{.003146(z'_o - z')}{T_o}\right]; \; \frac{dT}{dz'} = 0 \qquad (12.7\ a,b)$$

The temperature profile T(z') for altitudes of interest was divided into three regions to be represented by the following values[39] for p_o, T_o, z'_o, and $\frac{dT}{dz'}$:

region	p_o(mm Hg)	T_o(°K)	z'_o(m)	$\frac{dT}{dz'}$(°K/m)
0 km $\leq z' \leq$ 11 km	760.0	288.16	0	-0.0065
11 km $\leq z' \leq$ 25 km	169.7	216.66	11,000	0
$z' \geq$ 25 km	18.67	216.66	25,000	0.003

Table 12.1

Day to day changes in temperature and barometric pressure will alter the actual values for pressure, but the above quoted

quantities may be considered as representative of average conditions.

After p(z') has been calculated the other functions of z' are easily evaluated:

$$\rho(z') = \frac{Mp(z')}{RT(z')} = (4.645\text{x}10^{-4}\ \text{g °K cm}^{-3}\ \text{mm Hg}^{-1})\ \frac{p(z')}{T(z')}\ \text{g/cm}^3 \qquad (12.8)$$

$$\ell(x,y,z) = \frac{(x^2+y^2+z^2)^{1/2}\left(p(H) - p(z')\right)}{z\ (760\ \text{mm Hg/atm})}\ \text{atmospheres} \qquad (12.9)$$

In addition the shower penetration thickness within the atmosphere $\tau(z',\gamma)$, a quantity important in calculating the degree of shower development, may be expressed by the formula

$$\tau(z',\gamma) = \frac{p(H) - p(z')}{\gamma}\left(.03606\ \frac{\text{r.l.}}{\text{mm Hg}}\right)\ \text{rad. lengths} \qquad (12.10)$$

if we assume a value of 37.7 g/cm^2 per radiation length.

Table 12.2 presents a listing of exponential atmospheric absorption coefficients $a(\lambda)$ computed from published data[40] representative of normally clear conditions. $a(\lambda)$ is expressed in terms of inverse atmospheres; that is, $\exp[-a(\lambda)]$ represents the attenuation of light passing vertically through the entire atmosphere (to sea level). Such a vertical passage is equivalent to traversing a horizontal distance of 8.55 km at sea level. The principal absorption losses in the 3100 Å to 4300 Å spectral region are attributable to Rayleigh molecular scattering and absorption by dust. Naturally one should expect a reasonably large variability in the relative absorption under different

weather conditions. Frequently during nights which are clear enough to be considered useful (and hence included in running time estimates) the air is noticeably hazy, and on these occasions significantly lower atmospheric transmissions should be anticipated.*

λ(Å)	3150	3371	3450	3490	3537	3577	3710	3755
$a(\lambda)$	1.18	.85	.75	.73	.72	.68	.60	.57

λ(Å)	3805	3914	3965	4045	4277
$a(\lambda)$	.54	.50	.48	.45	.41

Table 12.2

To give the reader an overall perspective of the wavelength dependence for the different effects which have been mentioned up to now, Figure 12.2 displays a profile of the scintillation light spectrum together with graphs representing the exponentials of $-\alpha(\lambda)$, $-s(\lambda)$ and $-a(\lambda)$ ($\alpha(\lambda)$ and $s(\lambda)$ were defined in the text accompanying Equation 8.4).

The behavior of N as a function of τ has been treated in detail for a purely electromagnetic shower (i.e. involving only γ, e^- and e^+) by a number of investigators[42,43,44,45]. We chose to use a simplified expression presented later by Greisen[33] for evaluating N in the computations:

$$N = \frac{.31}{\beta_o^{1/2}} \exp[\tau(1 - \tfrac{3}{2} \ln s)] \qquad (12.11)$$

*See, for instance, the results shown in Ref. 41.

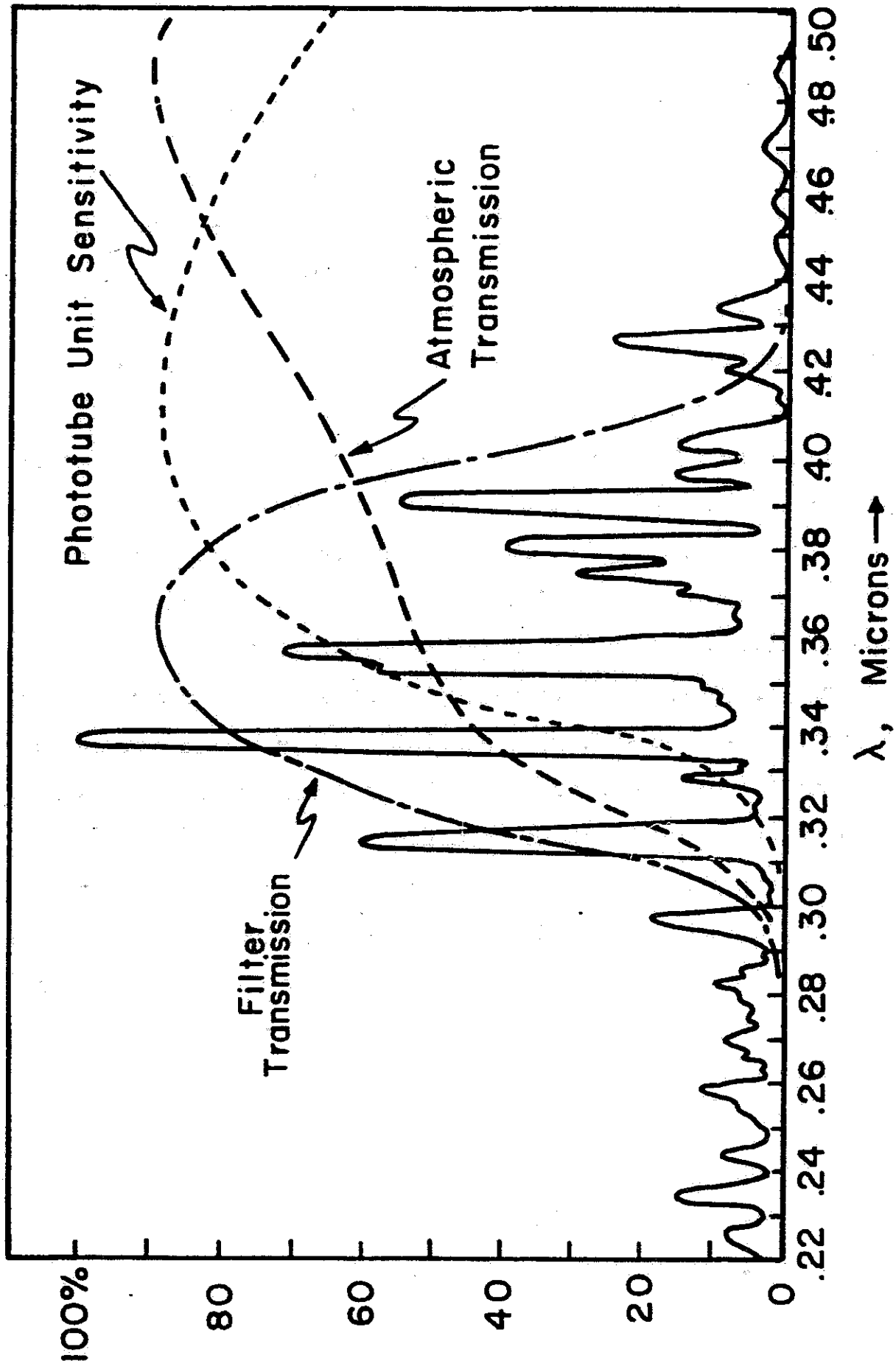
Phototube Unit Sensitivity
Atmospheric Transmission
Filter Transmission
100%
80
60
40
20
0
.22 .24 .26 .28 .30 .32 .34 .36 .38 .40 .42 .44 .46 .48 .50
λ, Microns

Figure 12.2

with

$$s = \frac{3\tau}{\tau + 2\beta_o} \qquad \text{and} \qquad \beta_o = \ln\left(\frac{W_o}{E_c}\right).$$

W_o represents the total energy of the shower produced by either an electron or gamma ray, the choice of which is unimportant at the stages of shower growth we are interested in. The critical energy E_c, which equals 84.2 Mev, is the energy loss due to ionization that an electron experiences traversing one radiation length (37.7 g/cm^2) of air. Formula (12.11) is based on solutions of the equations describing the loss and production of electrons, positrons, and gamma rays through a continuous range of energies by the processes of pair production and bremsstrahlung with the inclusion of a constant energy loss of the electrons by ionization (an original calculation, due to Greisen and Rossi, is frequently referred to as "Approximation B" in shower cascade theory). A brief summary is also given by Greisen[46] on the validity of the approximations and assumptions made in deriving the above result.

The problem of evaluating the number of electrons as a function of atmospheric depth produced by a shower initiated by a nucleon is far more complex, owing to the uncertainty in the nature of reactions involving strongly interacting particles at high energies. Vague predictions can be made about the origin and continuous modification of an electron shower which would occur in conjunction with the nucleon cascade. A large contribution comes from the production and decay of neutral pions continuously feeding the electromagnetic shower with γ-rays

(each new γ-ray would in turn initiate its own shower). Meaningful quantitative estimates on the nuclear cascade's growth and its subsequent transfer of energy to the electromagnetic component must be based on a good knowledge of the cross section, multiplicity, and overall inelasticity of high energy nuclear reactions. Tanahashi[47] has had some success in determining the latter parameters for lower energy showers ($E < 10^{15}$ ev). A summary of earlier studies on nuclear cascades may be found in reference 48. Indeed one of the objectives of our experiment would be to monitor N as a function of time to give needed information in this area. For the time being, however, we shall assume in our construction of the shower size as a function of depth that the shower was initiated by a single γ-ray of energy W_o. For the case of an incident nucleon we should bear in mind the fact that the computations for a shower of a given energy in reality are representative of the effect produced by an incident particle of slightly greater energy since some of the particle's original energy is retained in the nucleon cascade (in addition to muons and neutrinos which result from the nuclear cascade).

The quantity of noise associated with the received signal from an event was computed by finding the fluctuation expected for a light flux equal to the sum of the continuous background light and the signal pulse. Except for substantially large showers, the signal pulse has little effect in increasing the noise since the background level is roughly one thousand photoelectrons per microsecond. Shower signals having an intensity

this large, which would occur rather infrequently (see Figure 5.4), would raise the noise by a factor of only 1.4. Nonetheless the shower signal, albeit very likely insignificant, was added to the background flux since it was easy to program into the computational procedure. The evaluation of the noise intensity was derived in a discussion in the beginning of Chapter IV.

Additional signal fluctuations resulting from the uncertainty in statistics for the secondary electrons off the first few dynodes are, in effect, already accounted for in the computations since the value quoted for the cathode efficiency was based on an experiment measuring the noise on the signal from a steady light source of known intensity. That is, the maximum efficiency of 11% is likely to be slightly lower than what one would expect the true cathode efficiency by itself to be. An additional consequence of using the noise measurement as a basis for evaluating the cathode efficiency is the compensation for any errors introduced by the assumption that the amplifier rigidly samples and integrates consecutive, separate time blocks of 1.5 μs, which it does not: The R-C coupled amplifier system in fact continuously measures the signal within an exponential envelope moving forward in time.

The printer output from the computer listed for each Δs segment the following variables: t, x, y, z, r, N, the light flux value, and signals received in each channel. To obtain a better idea of the importance of the noise in relation to the size of the signal pulse, instead of just giving the value of

the signal itself, the output from each channel was listed as two numbers: the signal plus one standard deviation of noise and the signal minus one standard deviation of noise. In effect the listing gave the upper and lower error limits for $\pm$ 1σ (68% confidence limits). Provisions were also made for having the computer automatically plot the pulse forms for the five channels. The signal plus and minus the noise were over-plotted to give two traces representing the envelope of the error limits (see Figure 12.4, page 167). An increment Δs of fifty meters for each plot point proved to give a satisfactory smoothness and degree of accuracy to the plotted pulse forms. A printed output was given only for each fifth Δs calculation.

An additional feature of the program was to have a printed output of numbers representing the signal plus a random number, which varied from one reading to the next, to simulate the irregular output that would actually be received. The random numbers which were generated within the computer obeyed a Gaussian distribution centered on zero with a spread equal to the computed value of noise. As mentioned earlier, the noisy signal values were to be used as input to the analysis program.

In actuality both the printed and plotted outputs were expressed in terms of CRT trace deflections instead of voltage outputs from the emitter followers connected to the phototube anodes. The purpose in displaying the output in this form was to present the actual shapes that one would expect to see when reading the photographic record of event pulses, complete with

the distortions introduced after having passed through the logarithmic amplifiers. In addition, the analysis program was designed to accept raw data in the form of CRT deflections, and of course it was convenient to have the simulated data compatible with this requirement.

We may recall that the relationship of the phototube output voltage S to the CRT trace deflection x was defined earlier by Equation (7.1). Unfortunately the analytical form for the inverse of this equation is rather complicated since it involves the solution of a quartic equation in x. After evaluating S from Equation (12.3), therefore, the computer was instructed to determine x according to a precomputed tabulation (in fine steps) of S versus x for particular values of S_o and the four C_j specified for each channel.

Survey of Events

In attempting to conduct a reasonably comprehensive survey of expected results from an almost infinite variety of possible shower trajectories, as well as a number of energy ranges, one is faced with the problem of organizing a systematic program of sampling which will investigate a limited number of cases which are representative of the many broader categories of shower configurations. We should recall that in addition to the shower's energy, there are four independent geometrical parameters which may be varied (α, β, x_o, y_o). As suggested by the crude study in Chapter IV and later confirmed

by the analysis being described now, it is desirable to conceptually classify events according to energy and distance of closest approach. Within limits, changes in the radius r_o of the tangent sphere (see Figure 4.1 and the accompanying discussion) and changes in shower energy do not alter the basic character of the pulse shapes nor the relative instantaneous signal heights from one phototube channel to the next. In general, varying only r_o or E modifies in a predictable manner the scale of time and amplitude for the five pulses simultaneously. For a given r_o and E however, a change in the position or angle of contact on the sphere may drastically change the general appearance of the pulses among the different channels.

For the moment let us focus our attention on the different possibilities for trajectories tangent to a particular size sphere. First, it is important to recognize the fact that for each trajectory there are eight similar trajectories which would yield identical pulses except for a permutation of the signals among different horizontal channels. The similarity transformation consists of rotating all of the shower coordinates by a multiple of $\frac{\pi}{2}$ about the z axis and/or reflecting the trajectory about the x,z or y,z plane. Such a transformation is equivalent to switching the horizontal phototube units in a particular manner without moving the shower axis. Not all permutations of the four units are allowed however. The transposition of two adjacent units would yield signals which would no longer be self-consistent.

We may make the a priori assumption that the incoming primary cosmic rays are arriving isotropically, and therefore the likelihood that the contact point is contained within some small area on the sphere is independent of its position on the sphere, below as well as above the ground. Furthermore, there should be no preferential angular position for a shower's axis lying on the plane tangent to the sphere at the point of contact. If we restrict the choice of contact points to lie in a particular direction, say due north of the detection station, we see from Figure 12.3 that we may express a trajectory in terms of two angles: a zenith angle θ for the contact point and an angle ϕ describing the inclination of the trajectory to a horizontal line passing through the point.

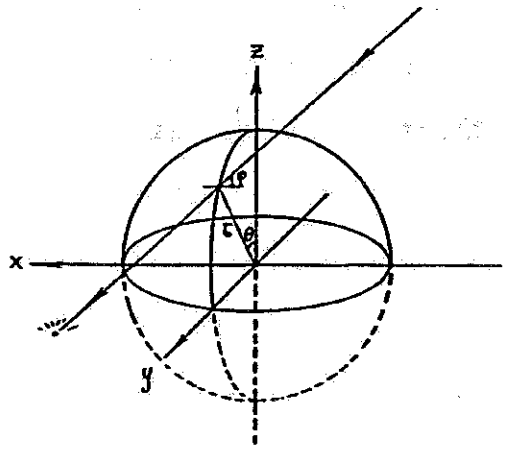

Figure 12.3

The previous statements made in this paragraph may be reworded to say that the frequency of events (per unit angle) is independent of ϕ and proportional to the sine of θ.

The similarity properties mentioned earlier allow us to restrict our attention to the angular ranges $0 \leq \phi \leq 90°$ and $0 \leq \theta \leq 180°$. Values outside these limits can be shown to be equivalent to those inside the ranges. To be sure, values of θ not far from 0° or 180°, and likewise ϕ approaching 0°, would correspond to showers arriving at small elevation angles. Such events would in practice be difficult to detect since the shower maxima would occur at extreme distances from the detector.

Naturally, in choosing the number of θ and ϕ values--as well as r_o and E combinations--to incorporate into the investigative regime one must balance, with the consideration of economy in the use of the computer, the need for an adequate sampling of intermediate intervals within the ranges of interest. The following parameters were selected for use in the systematic sampling program:

(A) (1) r_o = 3 km, E = 5×10^{19} ev

(2) r_o = 3 km, E = 1×10^{20} ev

(3) r_o = 5 km, E = 1×10^{20} ev

(4) r_o = 7 km, E = 2×10^{20} ev

(B) (1) The semicircle of contact points was to the north of the station.

(2) The semicircle of contact points was to the northwest of the station.

(C) (1) $\theta = 30°$

(2) $\theta = 60°$

(3) $\theta = 90°$

(4) $\theta = 120°$

(5) $\theta = 150°$

(D) (1) $\phi = 30°$

(2) $\phi = 60°$

(3) $\phi = 90°$

All combinations of the different choices within (A), (B), (C), and (D) were run, making a total of one hundred twenty shower simulations. Looking at the results of the investigations one can obtain an intuitive grasp of how parameter variations affect the appearances of the pulse signals. It is also easy to surmise what fraction of all the trajectories tangent to the sphere meet the requirements for signal readability specified in Chapter IV (we quoted a value of roughly 75%).

It would be difficult, of course, to document the results from all of the runs; however the four examples shown in Figure 12.4 illustrate the appearances of the graphical output for a few interesting cases which portray the following:

(a) $r_o = 3$ km, $E = 5 \times 10^{19}$ ev, $\theta = 60°$, $\phi = 60°$

(b) $r_o = 3$ km, $E = 5 \times 10^{19}$ ev, $\theta = 30°$, $\phi = 90°$

(c) $r_o = 3$ km, $E = 5 \times 10^{19}$ ev, $\theta = 90°$, $\phi = 90°$

(d) $r_o = 7$ km, $E = 2 \times 10^{20}$ ev, $\theta = 30°$, $\phi = 60°$

In all of the above cases the contact points were due north of the station. In examples (b) and (c) the equality of signals

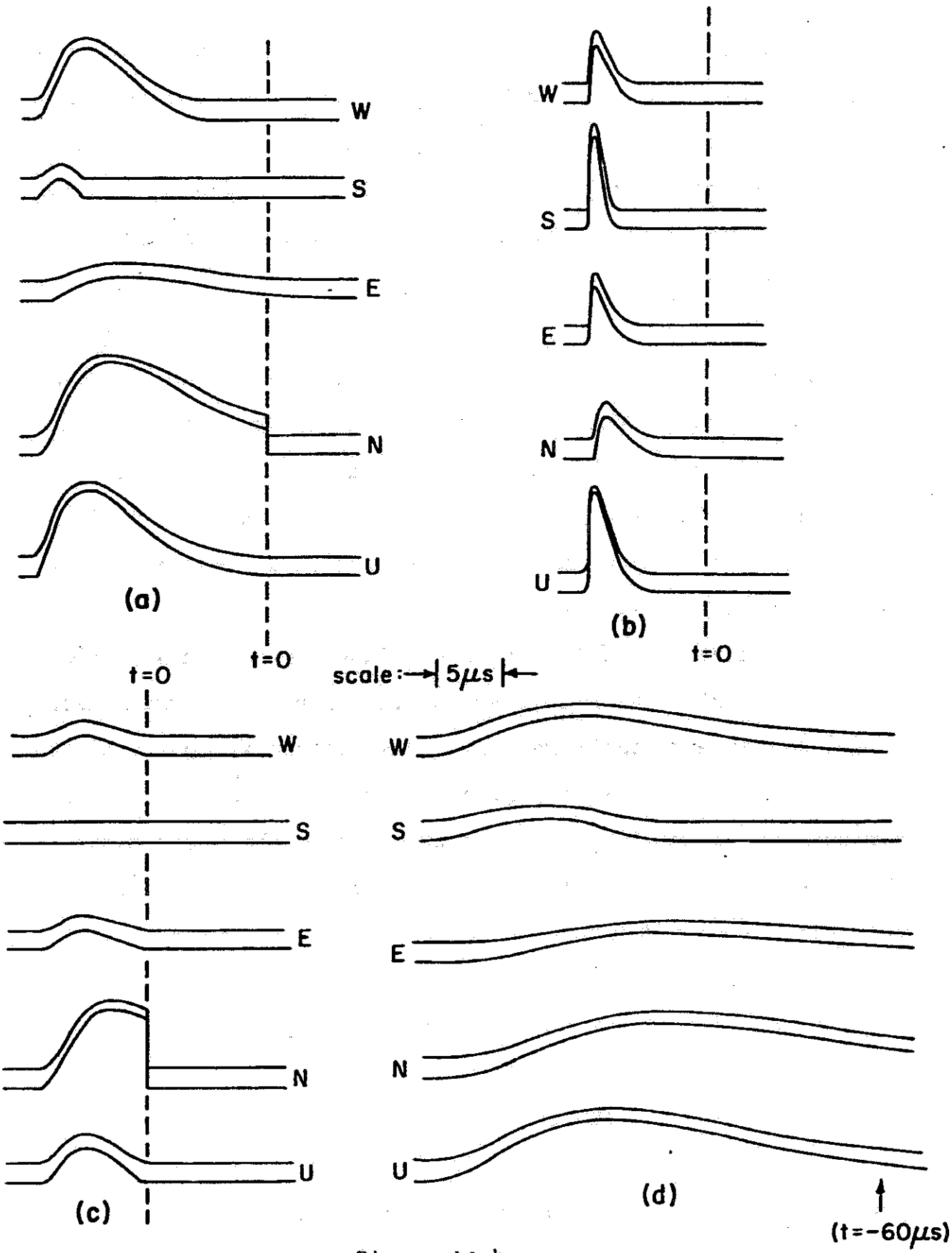

Figure 12.4

in west and east channels is due to the symmetry produced by having ϕ equal 90°. The dotted lines signify the apparent times of impact, which in some instances may be observed by an abrupt cessation of the signal. For example (d) the impact, if it were observable, would occur about sixty microseconds after the end of the portion displayed.

One feature of the plotted output which is misleading is the steepness in the rise or fall of some pulses. No allowances were made in the calculations for the smoothing effect on the signals arising from the limited amplifier rise times. The cut-off in the north channel of example (c), for instance, would be an exponential decay with a time constant of 1.5 μs rather than a step function as illustrated.

The narrowing of the noise envelopes on the pulses arises from two effects. First, it should be evident that the limits in (b) appear especially narrow because of the steepness of the pulses' upward and downward slopes. The second effect, which is perhaps not as trivial, may be attributed to the logarithmic character of the CRT display. On top of a large signal pulse, the noise is pushed into a region where the amplifier dynamic gain is less.

Except for the situations designated by

$\theta = 150°$; all values of ϕ

$\theta = 120°$; $\phi = 30°$

$\theta = 30°$; $\phi = 30°$

example (b) represents about the shortest of the pulse

durations found for the trials with r_o = 3 km. Marginal readability would be obtained with amplifiers having rise times equal to 1.5 μs for events as short as (b) since the profiles would be somewhat smoothed. Example (a) portrays one of the longer groups of pulses for the 3 km runs. In the light of remarks made in Chapter IV the variations exemplified by (a) and (b) from around two to fifteen microseconds may seem to be alarmingly large excursions from the expected value of nine microseconds $(\frac{r_o}{c})$. Nevertheless it should be noted that (a) and (b) were chosen to represent extremes in time differences (excluding the few θ and ϕ combinations specified), and also the event Q values are only proportional the square root of the pulse lengths.

In general it has been observed that nearly all of the shower configurations run for a constant r_o and E do indeed have maximum signal amplitudes which show surprisingly little variation for widely different angular configurations. This fact strengthens our confidence in the validity of the approximations made in deriving Equation (4.1). Table 12.3 summarizes the highest signal-to-noise value recorded in the channel which registered the largest pulse in each run under the category: r_o = 3 km, E = 5×10^{19} ev, contact points due north. Results similar to the ones given in the table were found for the other combinations of r_o and E.

On the other hand, significant variations are found in the number of channels displaying signals whose strength

θ	ϕ	max. S/n
30°	30°	8.7
30°	60°	13.0
30°	90°	14.7
60°	30°	14.8
60°	60°	11.6
60°	90°	9.7
90°	30°	13.9
90°	60°	12.5
90°	90°	10.0
120°	30°	10.4
120°	60°	13.8
120°	90°	14.2
150°	30°	3.9
150°	60°	8.5
150°	90°	11.7

Table 12.3 An illustration of the relatively mild variability in the peak signal strength received from widely different shower trajectories having a common value for r_o and E.

compare favorably with the best signal. This obviously is a consequence of having some events occur nearly overhead while other events are not far from the horizon. Such a fluctuation, together with the variability in pulse duration, leads to a mild uncertainty in estimating the readability Q for any event specified only in terms of r_o and E.

Analysis of Simulated Events

Altogether eleven computer simulated events were analyzed by the program described in Chapters VII to X. The properties of these events are listed in Table 12.4. Events (h) through

	r_o	E	Contact point position	θ	ϕ
(a)	3 km	5×10^{19} ev	north	60°	60°
(b)	3 km	5×10^{19} ev	north	60°	60°
(c)	3 km	5×10^{19} ev	northwest	60°	60°
(d)	3 km	5×10^{19} ev	north	60°	90°
(e)	3 km	1×10^{20} ev	north	30°	60°
(f)	7 km	2×10^{20} ev	north	60°	30°
(g)	7 km	2×10^{20} ev	north	30°	60°
(h)	3 km	5×10^{19} ev	north	90°	30°
(i)	3 km	5×10^{19} ev	north	90°	60°
(j)	5 km	1×10^{20} ev	north	30°	90°
(k)	5 km	1×10^{20} ev	north	60°	90°

Table 12.4

(i) had only the analysis of the probability distributions in x and y (the direction coordinates defined in Equations 9.11 a,b) for the different readings made without the subsequent evaluation of the orthogonal vector probability distribution. Event (b) was a rerun of event (a) with different random numbers used as noise. The comparison of these two events was of interest in determining the role the fluctuations played in altering the results (although in fact, we know that the probability distributions should indeed tell us the magnitude of the variations to be expected).

In general it was learned from the study of many events that as the signal-to-noise ratio in the channel having the strongest signal became less than about five, the probability distribution associated with an individual reading became so broad that the results were completely meaningless (i.e. the probability would be nearly the same over the entire sky). The subjective comments assigned to different event Q values presented at the end of Chapter IV and the data shown in Figure 9.6 were also derived from the survey.

The results from two of the analyses of simulated events shall be presented here to demonstrate the appearance of the output and illustrate the relative effectiveness of the analysis technique. In addition, we shall later have the opportunity to present a few methods of narrowing the uncertainty in the measured shower parameters using special arguments derivable from considerations of physical plausibility.

It is easier to show the application of such reasoning to specific situations than it is to discuss the ideas in a more formal, general fashion. The runs (a) and (g) are fairly typical of the examples we have to choose from, and yet they differ in character from one another in the following manner. Event (a) has a high signal-to-noise ratio and its duration is moderate, whereas (g) has a somewhat lower signal-to-noise ratio with a longer duration. Figures 12.5 and 12.8, respectively, show the noisy signals generated by the simulation program for events (g) and (a) to be analyzed. The corresponding signals without the random noise were shown in examples (d) and (a) of Figure 12.4. The horizontal and vertical scales for all of the drawings in Figures 12.4, 12.5, and 12.8 are identical with the exception of the horizontal scale of Figure 12.8 which is compressed by a factor of two. The events to be portrayed in Figures 12.5 and 12.8 were deliberately chosen to be the same as examples shown in Figure 12.4 to allow the reader to compare the appearance of the two modes of output from the simulator.

The short vertical lines on the baseline for each tracing of Figures 12.5 and 12.8 denote the times which correspond to the successive readings in the input data. The spacing between readings chosen from the simulator output is about 1.5 μs, which is the minimum allowable time we could expect the noise to be uncorrelated if we were to analyze an actual event. The expected signal appearance on either side of the more

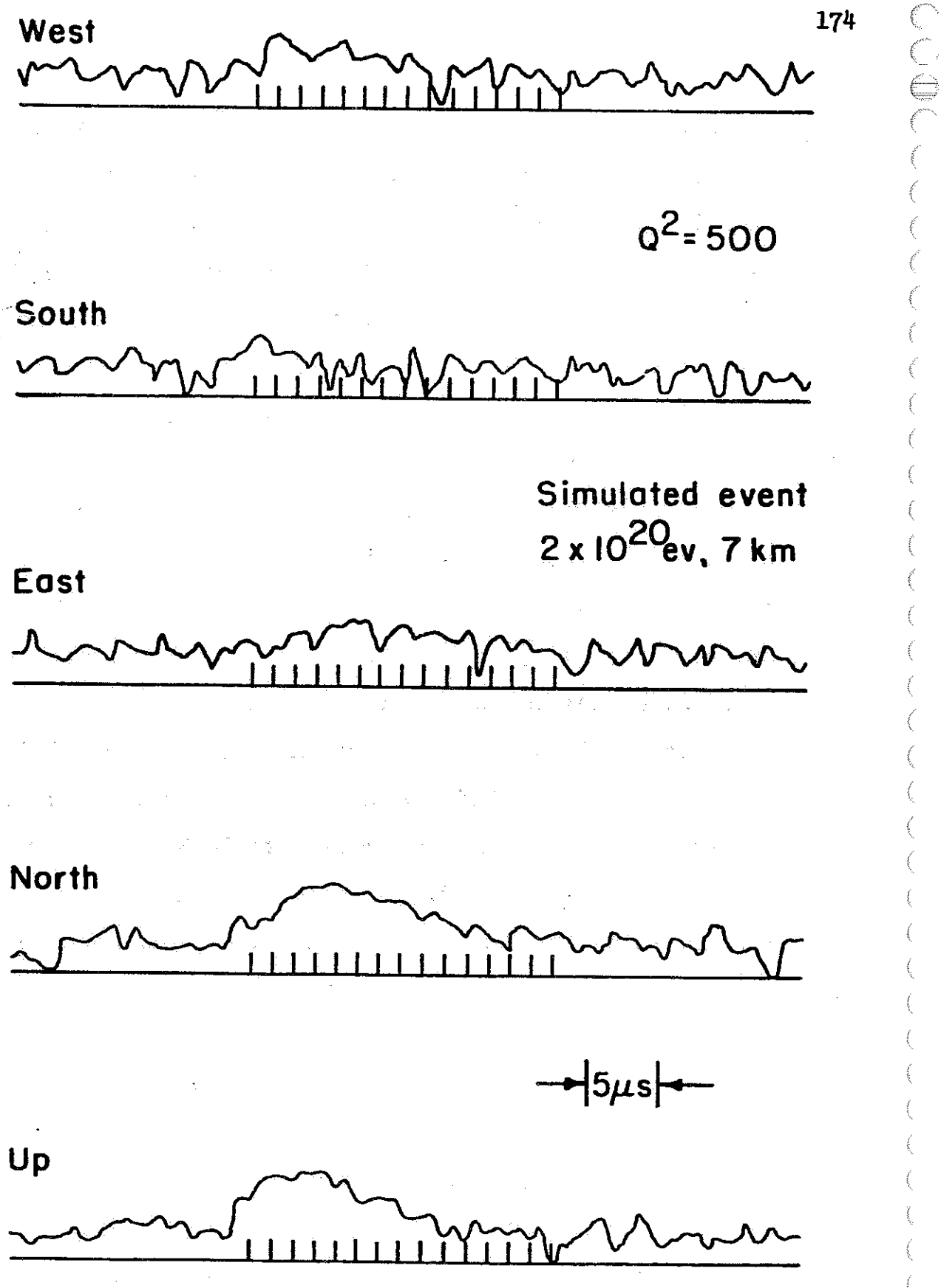
West
$Q^2 = 500$
South
Simulated event
2×10^{20} ev, 7 km
East
North
5μs
Up

Figure 12.5

significant portions (where the readings were taken) has been shown in an effort to give some impression of how well the shower's signals stand above the long train of noise. We must, in reality, have a group of signals which are recognizable enough to judge the time interval within which the data are significantly analyzable.

The final output obtained for the time independent study from the computer after having analyzed event (g) (depicted by Figure 12.5) is shown in Figure 12.6. As a matter of interest a small cross has been drawn in to indicate the true position of the orthogonal vector which naturally is a function of the known values of θ and ϕ in the simulator program.

It is perhaps more meaningful, however, to study the diagram shown in Figure 12.7 (and also Figure 12.9 which pertains to event (a) shown in Figure 12.8). For each orthogonal vector whose relative probability was calculated to exceed a certain value (e.g. all numbers exceeding 100 in Figure 12.6) we sketched the corresponding great circle as it would appear in the sky (using the stereographic projection). The numbers denote the probability (ln x 10) associated with each arc. The heavy line represents the true arc of the shower trajectory. The ellipses depict the contour of the least squares fit probability function W (see Equation 9.24) one standard deviation away from the most likely instantaneous positions x_o and y_o derived for each reading. The positions and shapes of the ellipses are drawn according to a tabulation produced by the computer of x_o, y_o, r_1, r_2, and θ which have been defined

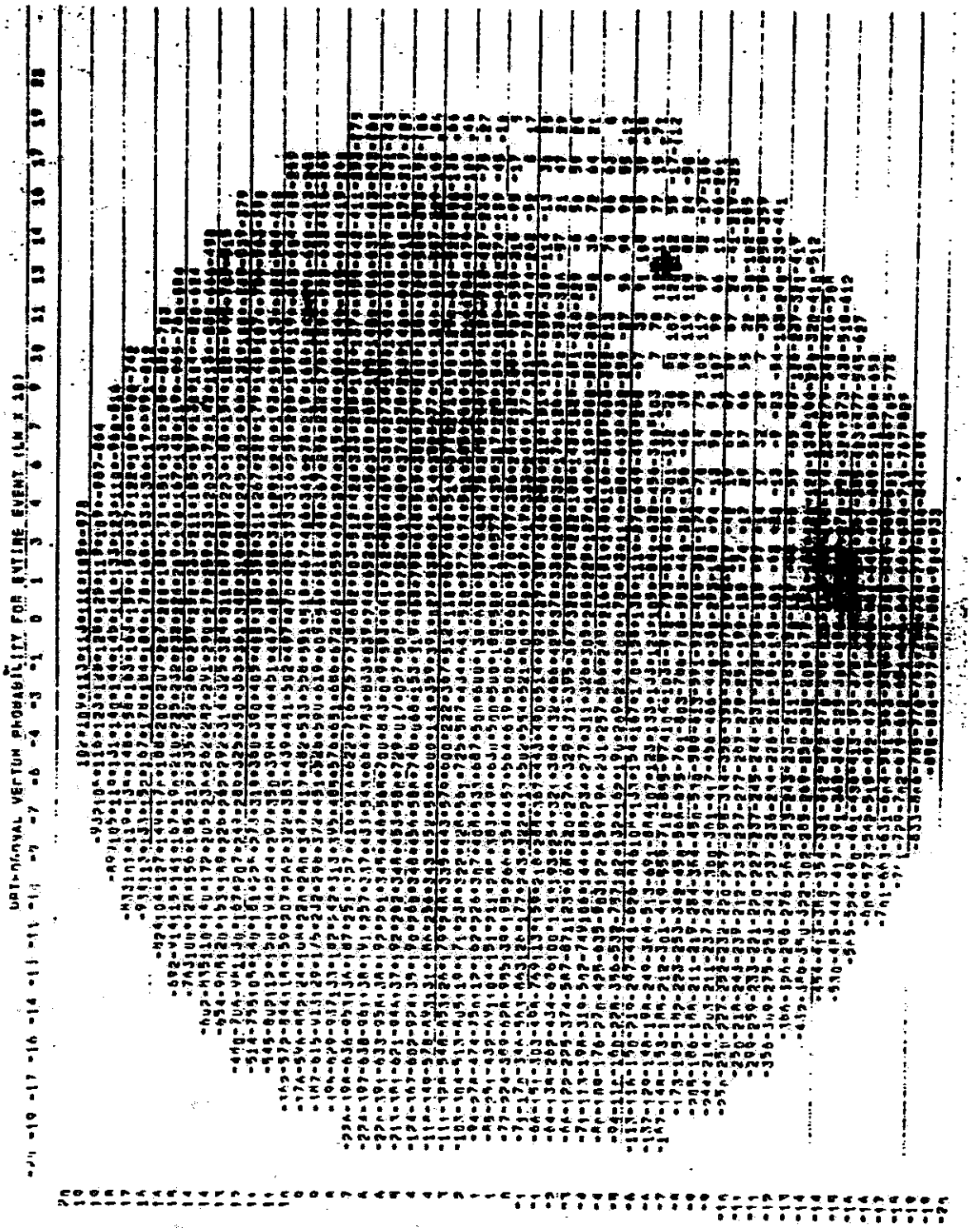

Figure 12.6

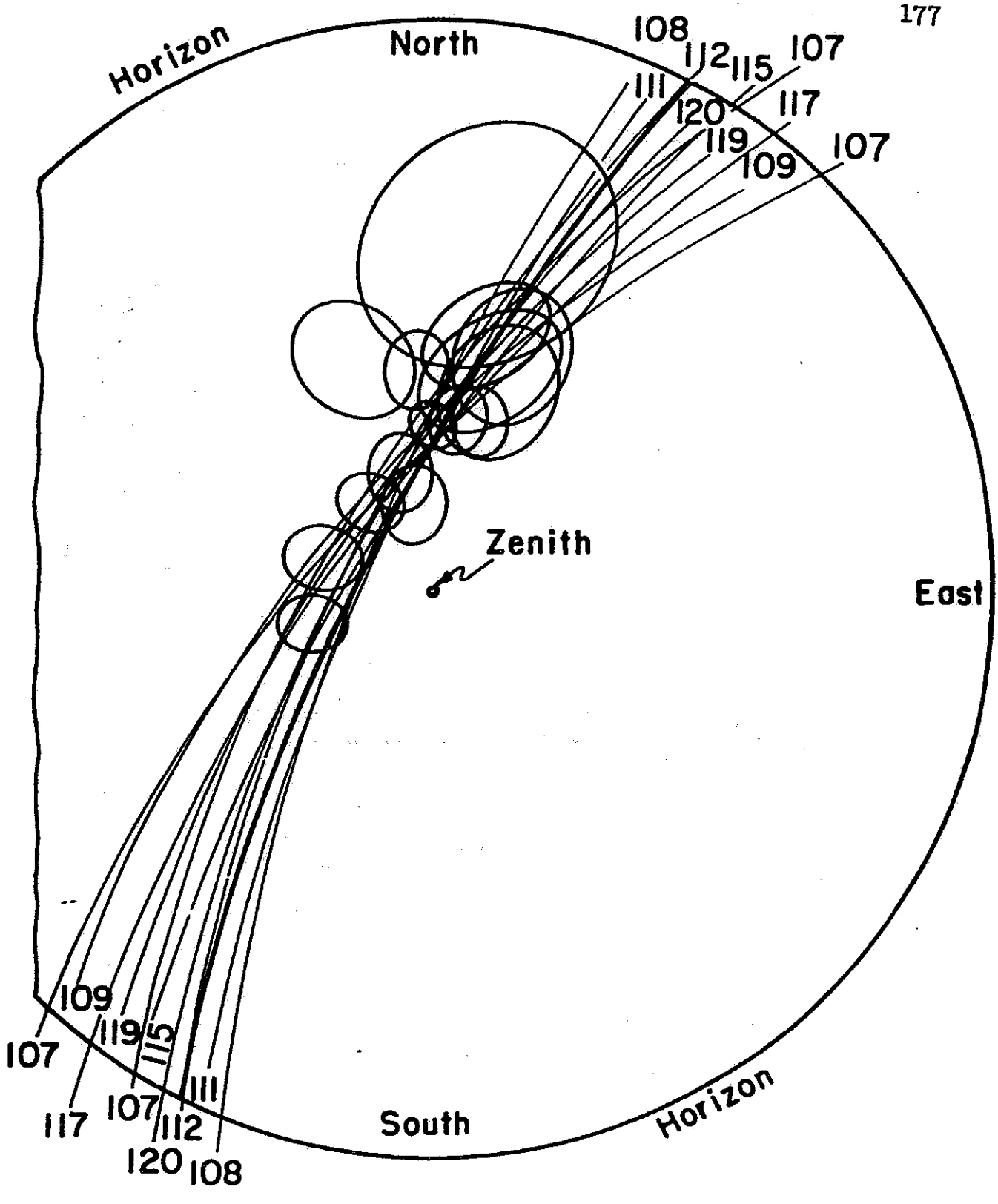

Figure 12.7 Family of great circle arcs having a computed joint probability integral exceeding e^{10} for event (g) shown in Figure 12.5.

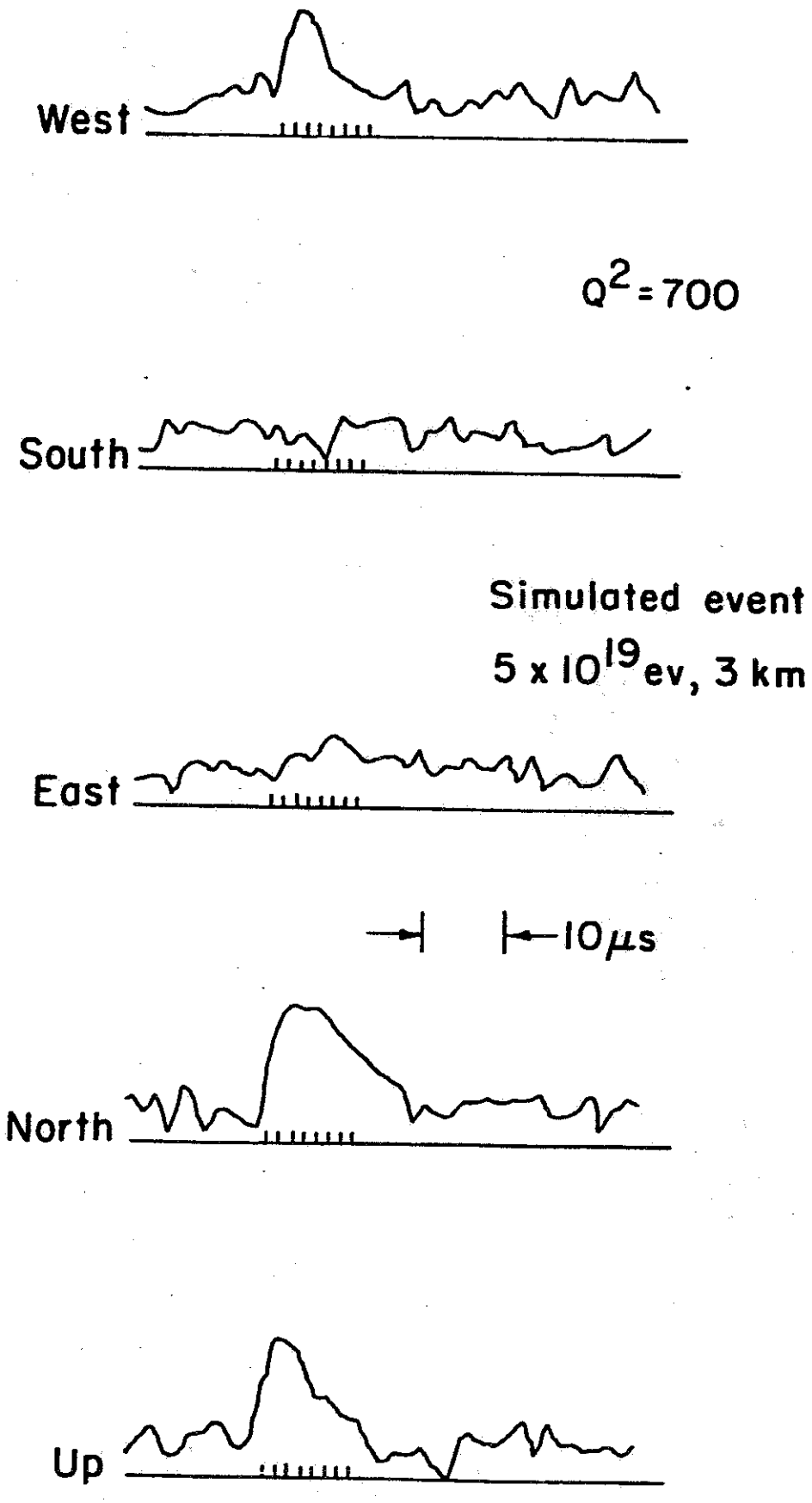
West
$Q^2 = 700$
South
Simulated event
5×10^{19} ev, 3 km
East
10 μs
North
Up

Figure 12.8

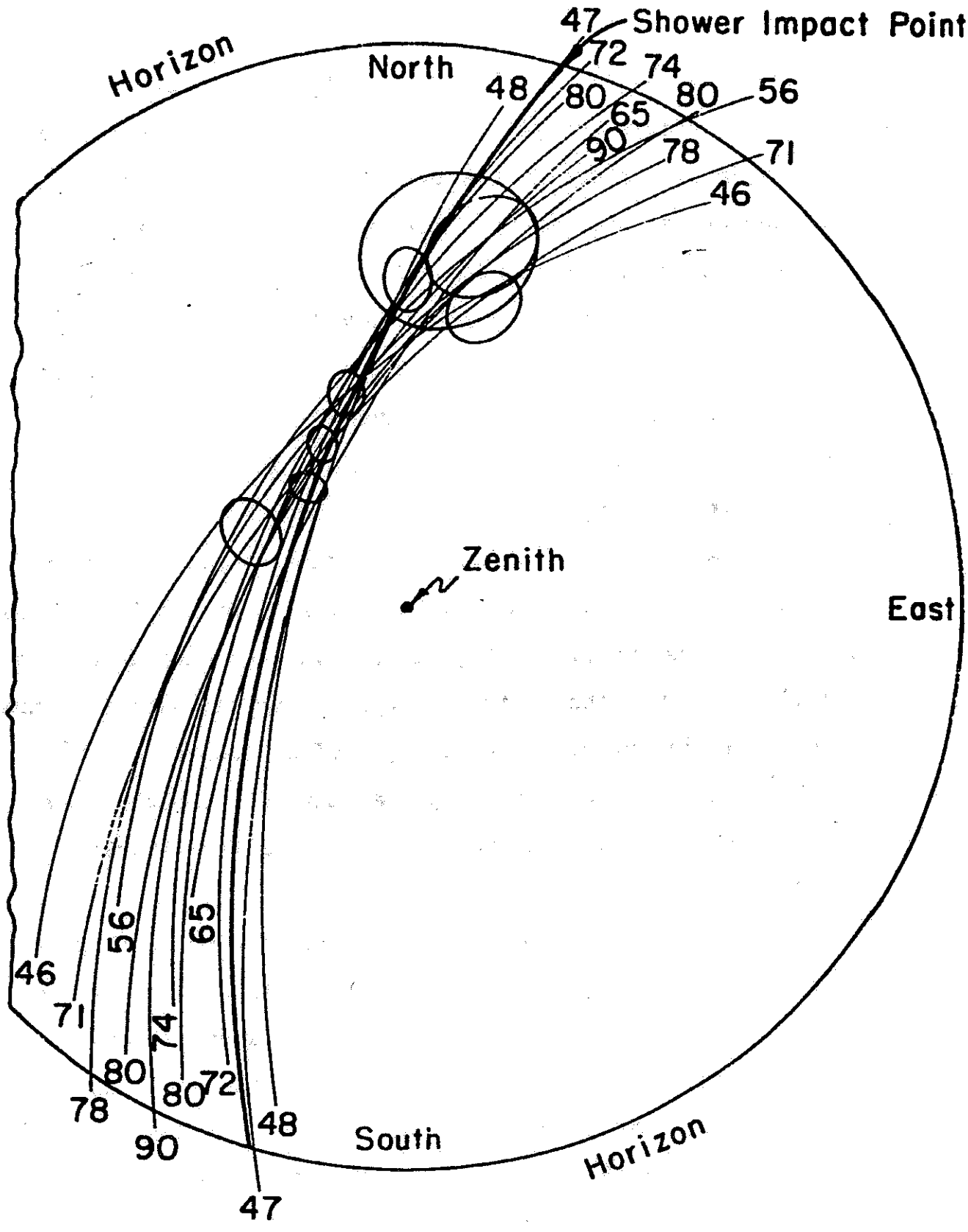

Figure 12.9 Family of great circle arcs having a computed joint probability integral exceeding $e^{4.5}$ for event (a) shown in Figure 12.8.

in Equations (9.24), (9.31), and (9.32). There are no numerical indications of how the ellipses are related to one another in time since it was felt that any attempt to give this sequential information would further confuse an already cluttered diagram. Instead it may be commented that as time advances the ellipses progress generally toward the horizon (upward in the diagram) with frequent erratic backtracking.

The printout of the actual probability distribution which was shown in Figure 9.4 was chosen from the calculation of the first reading in the sequence for event (g). This example was selected to allow us, at this stage, to compare the corresponding ellipse, which happens to be the lowest one in the drawing (Figure 12.9), with a detailed mapping of the function. We may thus obtain a feeling for the nature of the distribution's extent for an ellipse of a given size. We should recall that the actual probability distribution exp(U) does not differ much from the least squares fit distribution exp(W).

With some confidence it may be said that the orthogonal vector probability distribution indicates that the origin of the primary cosmic ray had a direction somewhere within, or closely neighboring, the clump of lines to the south of the first reading. As yet we have not determined the most likely longitudinal position along the lines. This position is specified in terms of the parameter θ_o which is connected with the time dependent study.

For the analysis of the change of θ_z with time for the two simulated events being shown here, the orthogonal vectors given in Table 12.5 were used. It should not be difficult for the reader to compare the results for event (a) in Table 12.5 with the size and placement of the ellipses in Figure 12.9 to ascertain the time ordering of the ellipses. Changing the orthogonal vector position within the small region where the probability is significant produces little change of any importance in the numbers listed in the table. The heights k_i vary and the θ_i values change by an additive constant. These variations do not appreciably alter the results of the time dependent analysis.

Figures 12.10 and 12.11 are sketches of the $k(r_o,t_o)$ and $\overline{\theta}_o(r_o,t_o)$ contours based on a computer printout of the variables for a variety of (r_o,t_o) combinations. We may recall that the goodness of fit parameter k, which was defined in Equation (11.1), is the logarithm of the overall probability at the most favorable position for θ_o (which occurs at $\overline{\theta}_o$). The heavy lines represent contour intervals in k of 5.0; lighter lines are drawn in to show intervals of 0.5 in the vicinity of high probability. The dotted lines indicate the mapping of $\overline{\theta}_o$ as a function of r_o and t_o. As the figures indicate, the values for σ are less than two degrees, and hence the certainty in the positions of the $\overline{\theta}_o$ lines far exceed the determinability of θ_o for the event (which is indicated by the range over which exp(k) is significant). One may conceptually think of the

EVENT (g)

Orthogonal Vector
x = 1.28, y = -.714

No.	Time	k_i	θ_i	σ_i
1	0.0	1.79	-15.9	6.34
2	1.7	2.00	-3.1	6.28
3	3.2	2.82	7.9	5.40
4	4.9	2.07	12.8	6.72
5	6.8	2.38	32.0	6.45
6	8.2	.63	14.5	5.89
7	9.8	2.66	26.6	5.20
8	10.6	1.54	31.1	6.97
9	12.3	2.06	33.9	6.37
10	13.2	2.23	40.9	10.10
11	15.1	2.13	46.3	10.09
12	16.1	.18	22.9	9.95
13	18.2	1.60	45.0	11.02
14	19.3	1.87	42.2	10.69
15	21.5	.78	59.9	22.18

EVENT (a)

Orthogonal Vector
x = 1.209, y = -.349

No.	Time	k_i	θ_i	σ_i
1	0.0	2.55	6.0	5.42
2	1.5	2.45	16.2	2.64
3	3.0	3.90	24.1	3.42
4	4.6	3.57	35.0	3.93
5	6.0	3.39	57.7	4.37
6	7.7	.31	59.8	4.65
7	9.6	2.39	63.8	7.07
8	11.8	1.92	63.9	9.92

Table 12.5 Parameters describing the Gaussian best fit probability function (Equation 11.6) for each reading of the two events. Times are expressed in terms of microseconds and angles are expressed in degrees.

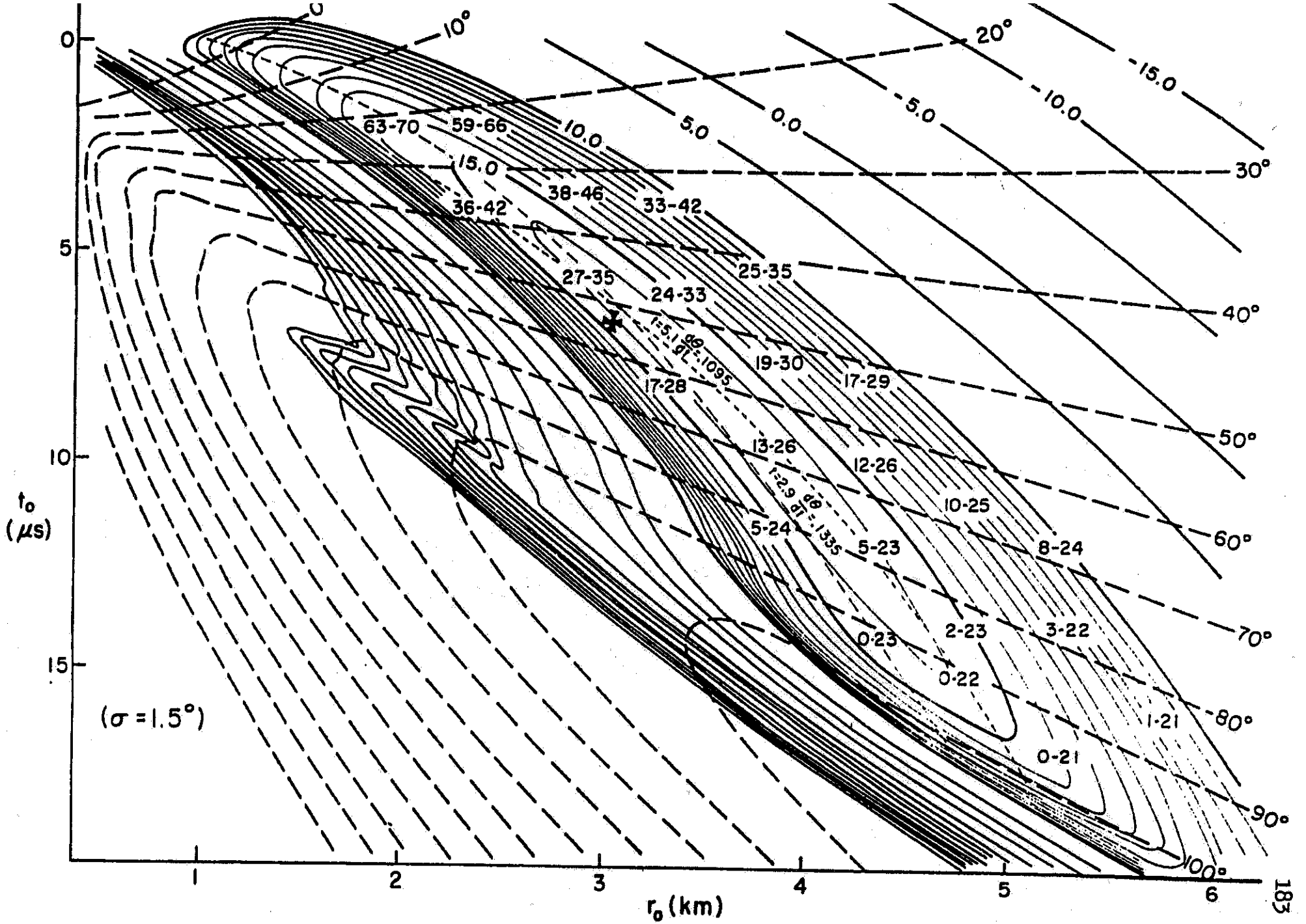

Figure 12.10 Probability map of variables from time dependent study for event (a).

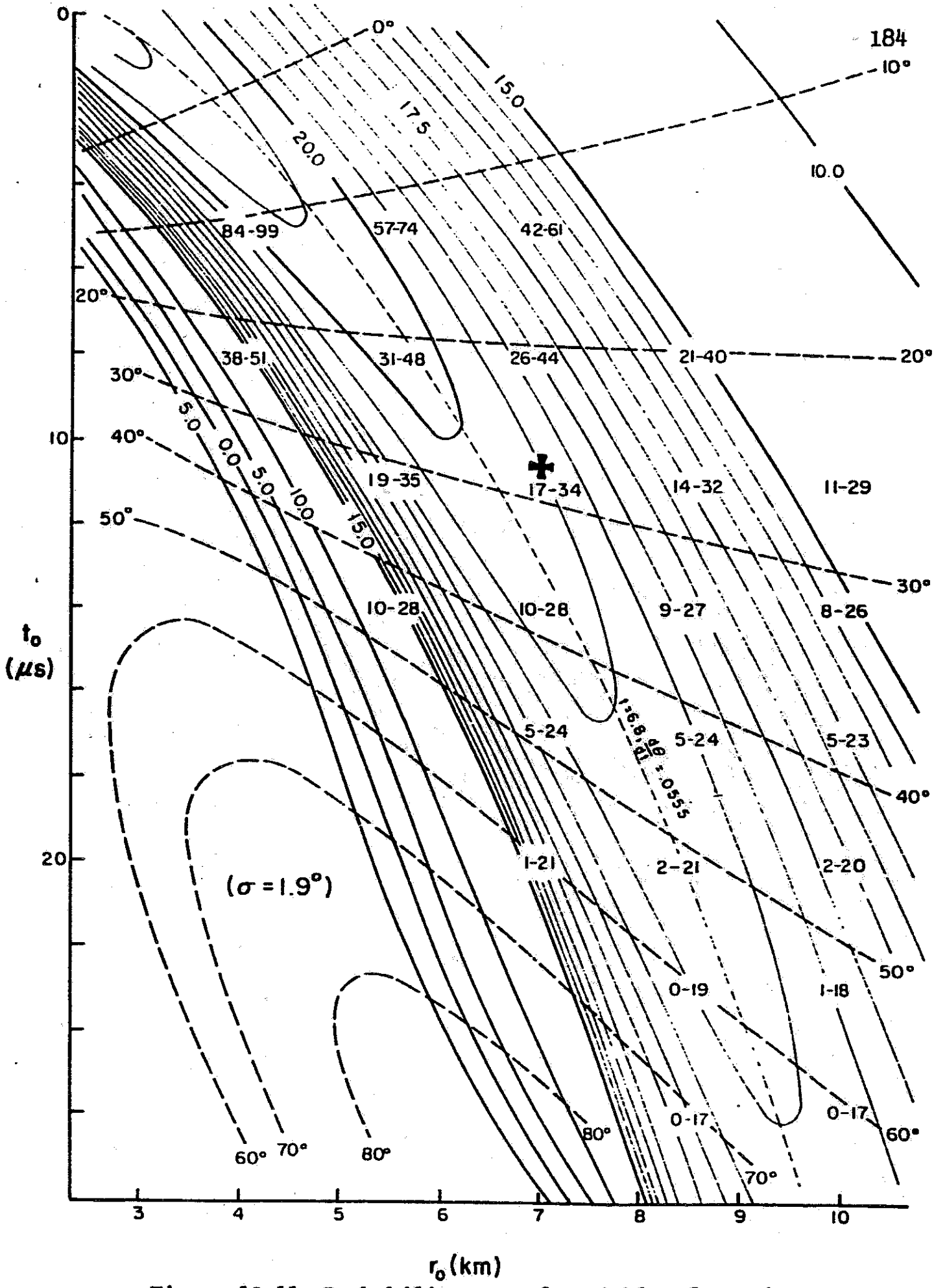

Figure 12.11 Probability map of variables from time dependent study for event (g).

dotted lines as being slightly fuzzy; the width of the fuzziness would be comparable to the standard error σ. The crosses in each figure indicate the true combinations of r_o and t_o whose values we know because the event is artificial. In both cases the values obtained for $\overline{\theta}_o$ evaluated at the true r_o and t_o are in error with respect to the true θ_o by approximately one σ in θ_z; that is, the $\overline{\theta}_o$ values indeed seem to be correct to within about two degrees.

The two drawings confirm the prediction expressed earlier in Chapter VI: namely, it is difficult to discriminate distant approaching showers from nearby receding showers. This uncertainty is not surprising when it is remembered that widely different combinations of θ_o, r_o, and t_o may produce strikingly similar θ_z versus time curves. It is evident that even for events whose observations span a moderately large angular range the lack of definition in r_o and θ_o is considerable, and we may expect the indistinguishability to worsen for events with shorter angular ranges, for instance simulated events having the closest approach occurring at a virtual point below the horizon.

Since the assertion was made in Chapter VI that the primary uncertainty in measuring r_o and t_o arises from the difficulty in determing $\frac{d^2\theta}{dt^2}$ from inaccurate readings over a limited angle, it may be of interest to compare the shape of high probability regions with the curve of t_o versus r_o one could hypothetically obtain with a single accurate measurement of $\frac{d\theta}{dt}$ taken at a time t. Substituting Equation (11.14) into the expression for $\frac{d\theta}{dt}$

(Equation 6.2) we find

$$\frac{d\theta}{dt} = \frac{c}{r_o}\left(1 - \frac{A^2 - 1}{A^2 + 1}\right) \qquad (12.12)$$

(the quantity A was defined in Equation 11.11) which gives the following quadratic equation in t_o:

$$c^2 t_o^2 - 2c(ct + r_o)t_o + c^2 t^2 + 2r_o ct + 2r_o^2 - \frac{2cr_o}{\frac{d\theta}{dt}} = 0 \qquad (12.13)$$

Solving the equation gives the result

$$t_o = \frac{r_o}{c} \pm \sqrt{\frac{2r_o}{c\frac{d\theta}{dt}} - \frac{r_o^2}{c^2}} + t \qquad (12.14)$$

Upon examination of simple examples it becomes clear that the minus sign gives the correct root. The light dotted lines in each figure are plots of this relation for the labeled values of t and $\frac{d\theta}{dt}$. The latter values were chosen to give a curve which fitted the high probability ridge, and we see that they roughly correspond to the mean values of t and $\frac{d\theta}{dt}$ for the more significant measurements of the entire group. The close agreement between the probability analysis and the curve representative of Equation (12.14) in effect demonstrates that for the most part our success in limiting the likely values of r_o and t_o to a long, thin, sausage-shaped region may be interpreted as being equivalent to our having obtained a good measurement of the average $\frac{d\theta}{dt}$ near a certain time t, and greater measurement accuracy must be achieved if we are to detect the more subtle features of the angular progression with time.

Arguments based on physical plausibility may be utilized to limit the extent of the region of uncertainty. For instance, we may categorically eliminate any values of r_o and t_o having a $\bar{\theta}_o$ value significantly (by a few standard deviations) less than zero. It was pointed out earlier that negative values for θ_o correspond to showers progressing upward. However we may carry the reasoning further to examine (θ_o, r_o) values which yield inordinately high or low atmospheric penetration thicknesses for observed positions in θ_z for the event. The paired numbers shown in Figures 12.10 and 12.11 indicate for the appropriate (r_o, t_o) coordinates the depth in radiation lengths to be expected for the first and last values of θ_i. That is, the numbers give an approximate indication of the observed range over which the shower had a large number of secondary electrons. Clearly we may eliminate the extreme upper left and lower right portions of the high probability region since they represent absurd shower configurations. How far one is willing to restrict the range of the allowed region using this line of reasoning is dependent of one's judgement of the accuracy of present models of shower growth and is also dependent on an estimate of the primary particle's energy. Offhand we might conclude that the region bounded by $35° < \bar{\theta}_o < 70°$ for Figure 12.10 and $15° < \bar{\theta}_o < 45°$ for Figure 12.11 would give tenable shower structures. The necessity for having to use the penetration depth criteria for establishing reasonable limits for r_o and θ_o under the

present circumstances of poor determinability should naturally preclude any application of the results we obtain to a study on the rapidity of shower development or the nature of the early, high energy interactions.

From a general point of view we have seen evidence, arising from both deductions on the nature of the time dependent equations and from the specific examples just given, indicating the degree of difficulty in resolving the shower coordinates along the plane of best fit from the data given by a single observing station. If we were fortunate enough to observe a particular shower from two or more widely separated stations we could indeed reduce the uncertainty. A time independent reduction of the data from two stations would be sufficient to determine the shower geometry since the intersection of two best fit planes would define the axis of the shower. In all likelihood the accuracy of the latter determination would surpass the precision of the time dependent analysis from each station alone. Naturally one would also want to employ a time dependent analysis to the pulses received in each station to possibly narrow the uncertainty in the intersection line of the two planes.

Additional improvement in determinability over the independent measurements of an event from two or more observing stations may be obtained if a time correlation could be introduced between the separate records. Each station registers the event in terms of four spatial variables and one

time variable. The spatial variables of the different stations have a known complicated relation to one another which is determined by the relative placement of the stations, and hence there are only four truly independent spatial dimensions to be measured in the combined analysis. However without some time reference the coordinate t_o for each observer would be an independent variable whose uncertainty would contribute to the overall error of the event's interpretation. A fraction of a microsecond time correlation eliminates all but one of the time unknowns, and we would be left with only five unknown parameters to measure, as in the case with a single station. In practice, a means for obtaining such a time reference between stations would not be difficult. For example, at some specific time while the recording of an event at one station is in progress, a strobe lamp which is beamed toward another station could be pulsed. If the other station also triggered on the event, it would automatically register the light pulse from the first station as a spike near the end of the CRT trace from a particular phototube channel. In addition to supplying microsecond timing comparisons, such a scheme provides assurance that both stations really recorded the event in unison. One could also employ the light signal as a monitor of the atmospheric transmission near the ground.

XIII. PROPOSED DETECTION APPARATUS OF ADVANCED DESIGN

After the pilot experiment had been in operation for over a year, it became increasingly clear that a more ambitious design was necessary to accomplish the task of acquiring within a reasonable period of operation meaningful information on the nature of high energy primary cosmic rays and the development of extensive air showers. The failure to achieve positive results in the first version of the experiment may be attributed to the fact that the orders of magnitude for the different parameters discussed in Chapter IV were too unfavorable. However, as we pointed out at the end of Chapter V, from the lack of clearly recorded events we can infer an upper limit to the cosmic ray frequency spectrum. Such an addition to the scant information which exists on the magnitude of the frequency is not only of scientific interest, but it plays an important role in determining the complexity and size of any future generation experiments which could yield tangible data. It should be clear that the results from the pilot experiment indicate that the next version of the apparatus for detecting showers by means of atmospheric scintillation should have a sensitivity far in excess of the present experimental version.

It was pointed out in Chapter IV that quantities which influence the detection capability of a single station are basically ε_s, ε_b, A and Ω. It would be difficult to raise the overall photoelectric efficiency ε above the values commonly found in photomultiplier tubes available nowadays without

resorting to the use of expensive, special purpose solid state devices or photomultipliers having a somewhat exotic type of photocathode. The easiest and most economical method of improving the equipment design appears to be an effort directed towards increasing the area A or decreasing the solid angle Ω of each photosensitive detector.

The glass absorbing filters which were employed in the pilot experiment appear to give the best $\frac{\epsilon_s}{\epsilon_b}$ enhancement of the commercially available colored glass. Considerable improvement might be obtained by using interference filters which have multilayer thin dielectric films deposited on a glass surface. Such filters may be custom designed to have a very narrow band-pass at any desired wavelength. The fabrication of an interference filter which admits a number of specific wavelengths, which would be desirable since there are several relatively strong emission lines present, is generally considered to be a difficult but not impossible task. However, the interference filters have a serious shortcoming of suffering a disruption of filtering properties for light beams which are not nearly at normal incidence. A system employing narrow band filters would therefore require the admission of light within a relatively small solid angle. Nonetheless one cannot immediately overrule the possibility of using such a technique in an experiment of advanced design.

In passing it may be worthwhile to mention a particular technique for enhancing the light gathering capability of a detector which in the course of preliminary design studies

briefly occupied our attention. The restrictions imposed by the conservation of phase space in an optical system may be overcome to a small degree if we allow the light to enter a region of high refractive index containing a wavelength shifting substance. The wavelength shifter is relatively opaque to the ultraviolet radiation, and hence nearly all of the scintillation light would be absorbed. Some of the absorbed energy would be re-emitted in the form of longer wavelength light by the substance, and such emission would be isotropic. A good fraction of the re-emitted light would be trapped within the refractive medium due to the fact that it would experience total internal reflection, and the medium would be relatively transparent to the longer wavelength light flux. Hence one could have in effect a means of "trapping" the ultraviolet radiation and conducting it to a small photosurface which is optically matched to the refracting body. Such a device would also have the desired spectral rejection properties since the night sky background light in the visible region would pass unabsorbed through the material.

A tentative design model was proposed employing a cylindrical aluminum mirror which focused the incoming light onto a long glass tube containing the trapping substance in liquid form. The scale model of the system shown in Figure 13.1 was constructed in an effort to learn how efficient the device would be in actual practice. In theory, if the many mechanisms for loss are neglected, the effective light

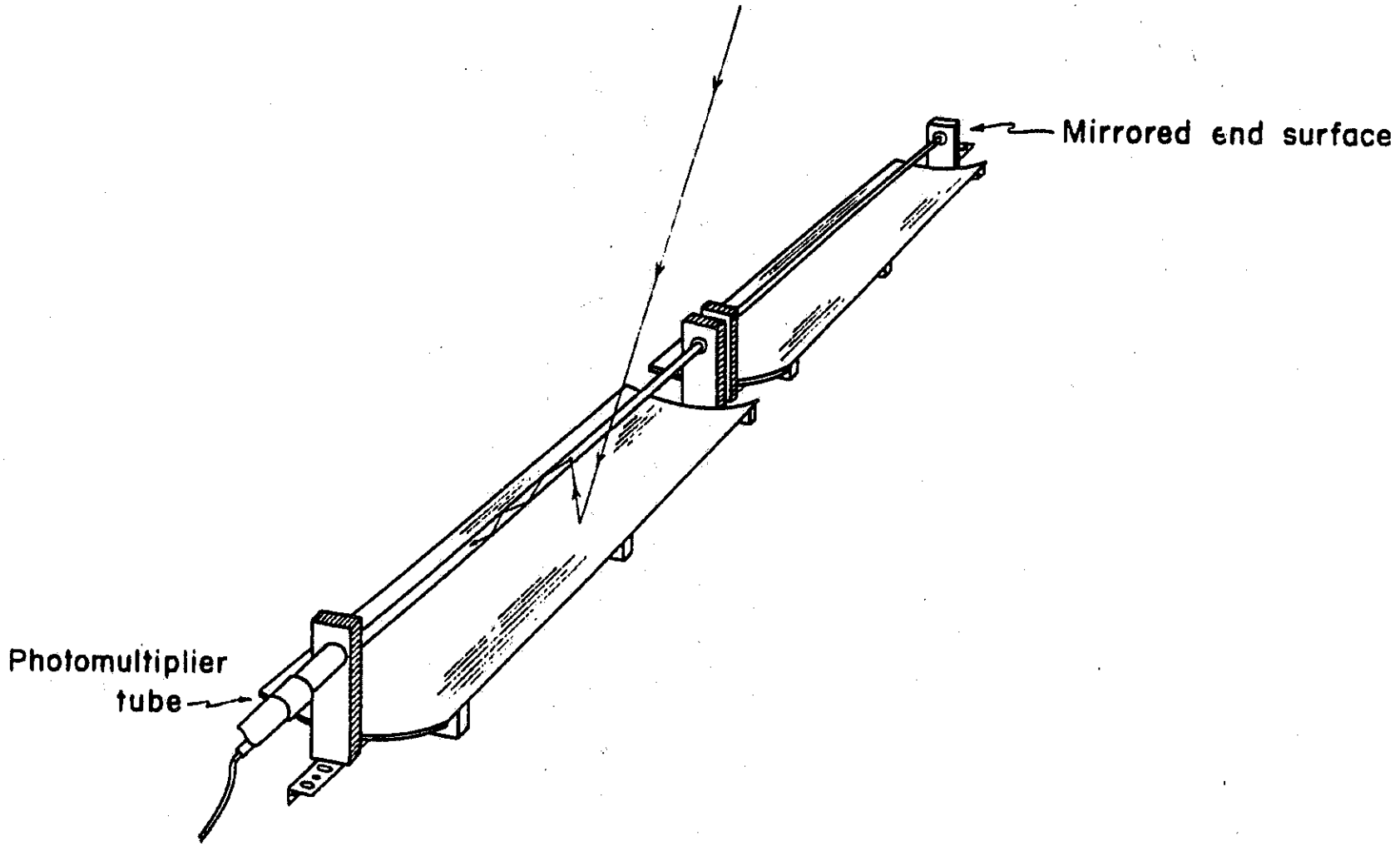

Figure 13.1 Scale model test section of proposed cylindrical detector using a wavelength shifter for converting the UV signal flux into trapped visible light.

gathering area equals the area of the mirror times the trapping efficiency of the light reradiated within the tube. To be trapped the light must be emitted in either of two directions within a cone whose half angle equals the complement of the critical angle for internal reflection, $\cos^{-1}(\frac{1}{n})$. The trapping efficiency therefore would be the relative fraction of solid angle contained within the cone, $(1 - \frac{1}{n})$. The limiting length over which the apparatus is effective is governed by how much the re-emitted light is absorbed as it travels down the tube. Not much is gained by extending the system longer than several mean absorption lengths. The detector effectively samples a slot in the sky whose angular width equals the arc tangent of the tube diameter divided by the mirror's focal distance and whose angular length would not exceed twice the arc tangent of the system's total length divided by the focal length. One could envision a detection station employing two large banks of these devices mounted perpendicular to one another. Each bank would contain units which viewed adjacent thin slots in the sky. The pair of units, one from each bank, which registered a signal would define the source direction of the light.

Measurements performed with the scale model indicated that the following loss mechanisms seriously limited the effectiveness of the system:

1. The reflection coefficient for the sheet aluminum surface (which was polished) is approximately 1/6 for the ultraviolet light. This figure includes losses due to small

irregularities in the curved mirror surface. The surface could be of better quality if greater care in fabrication had been taken.

2. UV absorption losses in the glass walls are a relatively moderate source of attenuation. Quartz tubes would be prohibitively expensive; plastic tubes are crazed or dissolved by most solvents and they are easily scratched on the outside. Losses can be minimized by using special UV transmitting glass (Vicor).

3. The efficiency in converting UV light into visible light for the wavelength shifter POPOP*, which seemed most suitable for the job, was measured to be approximately 17%. This figure represents how well the reradiated light is registered on an S-11 phototube compared to the response to the UV radiation alone (at 3600 Å).

4. Imperfections and dirt on the surface of the tube render the internal reflections less than 100% efficient.

5. To some extent the solvent and the POPOP really do absorb the visible light.

The mean absorption length (attributable to the last two effects listed above) was measured to be roughly one meter. Tests were performed using a number of solvents; the ones of principal interest were 1,2 dichlorobenzene and mineral oil, which have a high refractive index with relatively low UV

*2,2'-p-phenylene-bis-(5-phenyloxazole); see Ref. 49.

absorption. The concentration of POPOP was regulated to absorb most of the UV light across the tube's diameter without adding unnecessary additional absorption to the visible light. On the whole, the tests indicated the various losses negated the advantages inherent with the trapping concept. The tube without the focusing mirror effectively increased the collecting area of the photomultiplier by only a factor of 2.2; the mirror, of course, served as a means for collecting (rather inefficiently) the light over a large area from a small solid angle.

In view of the disappointing results obtained from the tests on the device featured in the previous discussion, an experiment utilizing a more conventional optical setup was favored as a choice for the design to supersede the pilot version. The plan incorporates the installation of a large array of small photomultiplier tubes mounted on the image surface (which has a mild curvature) of a Fresnel lens. The hexagonally close-packed cluster of two inch diameter tubes lying on the focal surface of the lens has an appearance reminding one of a fly's eye, and a cross section of the arrangement is shown in Figure 13.2. This assembly divides the sky two-dimensionally into small pieces of solid angle whereas the cylindrical system partitioned the sky in only one dimension.

The two-dimensional division calls for an ambitious undertaking in the sense that many phototubes are used, and there is a large number of independent signals which must be detected

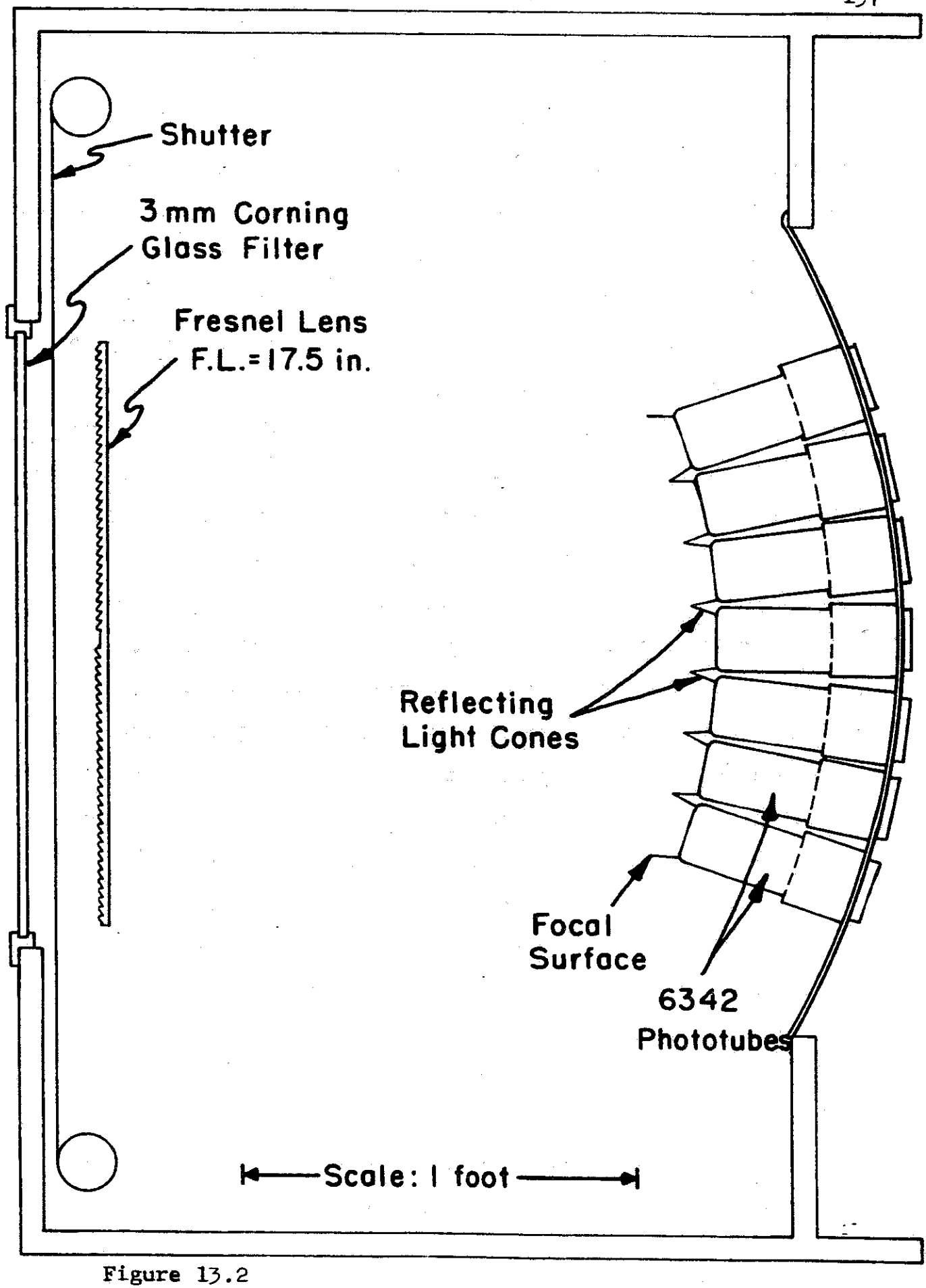
Shutter
3 mm Corning
Glass Filter
Fresnel Lens
F.L.= 17.5 in.
Reflecting
Light Cones
Focal
Surface
6342
Phototubes
Scale: 1 foot

Figure 13.2

and recorded by the electronic apparatus. However, in addition to a substantial enhancement of signal-to-noise ratio, our efforts are rewarded by the relatively precise means at our disposal for defining the source direction of the light. Hence accurate relative pulse amplitudes need not be determined, thus permitting one to analyze events of lower Q than what would be considered tolerable with the wide angle system. The solid angle viewed by each photomultiplier tube in the matrix is approximately $\frac{1}{100}$ str, and hence the night sky noise is reduced by a factor of $\sqrt{\frac{\pi}{1/100}}$ as compared with the pilot station. The diameter of the lens (18") is slightly larger than the diameter of the large phototubes in the pilot experiment. In short, one may compare the capability of the new experiment to the old one by again referring to the diagrammatical representation in Figure 5.4. For the new version the equivalent form of the diagram may be visualized by shifting the diagonal night sky noise line by slightly more than a factor of ten toward the upper left and by shifting the Q^2 lines a factor of several hundred toward the left. Table 4.1 shows us that the increase in counting rate may range from a factor of slightly less than ten for large events to nearly a hundred for barely detectable pulses. Additional gains may be realized since small phototubes have cathode efficiencies of typically around 18% (which significantly exceed the 11% efficiencies normally found for the larger phototubes).

To view the entire area above the horizon a single detection station must have sixteen complete viewing assemblies

pointed toward different regions of the sky. The coverage of solid angle for all of the units corresponds to the faces on the upper half of a truncated icosahedron (a semi-regular convex polyhedron consisting of twelve pentagons and twenty hexagons). The assemblies therefore are divided into two types: those viewing hexagonal sectors which contain thirty-seven photomultipliers and those viewing pentagonal sectors containing twenty-five tubes. All of the sectors are roughly forty degrees in width. To view the entire sky 520 phototubes are required.

The manner of recording the information on an event will be similar to the method already in use. A large bank of cathode ray tubes will display the signal pulses in front of a camera. The tubes will be arranged in an array having the proper sequence to visually represent a mapping of the sky for ease in interpretability. Thus an event would appear as a linear (or slightly curving) succession of traces which show pulses advancing in time, with the exclusion of any unusual disturbances in the traces of the remaining cathode ray tubes. The apparatus could be triggered by a logic circuit designed to detect the coincidence of large pulses occurring in any phototube and one of its neighbors.

With such a large volume of complex data being registered one might be encouraged to devise a digital recording system instead of having the gigantic array of cathode ray tubes to be photographed. The film reading may turn out to be a formidable task, especially if many false triggers are

obtained over long periods of operation, and furthermore the design of a display system capable of presenting accurately measurable pulse tracings (with good vertical and horizontal calibrations and reference points) and high level amplifiers for all 520 channels may be a significant challenge in fabrication. In the end, a computer processing of the information which has been accurately registered digitally may prove to be the most convenient and desirable. In the meantime, however, until one has had some preliminary experience with measuring and interpretative techniques after having studied the configurations and appearances of signal pulses together with the many possible forms of spurious noise disturbances, it is perhaps wise to make use of the visual form of representation --a form which retains all of the analog information present and displays it in a manner which is well suited for diagnostic purposes.

The comments stated earlier (at the end of the previous chapter) concerning the advantages of viewing air showers stereoscopically emphasize the desirability of having more than one station operating within a given area. Rather than building a single station which monitors the entire sky, therefore, we have favored a plan to build two separated half stations (i.e. stations which observe only π str instead of 2π str) which monitor a common region of the atmosphere. Such an overlap of detector sensitivity reduces the efficiency with regard to counting rate; however, those events which are registered will be recorded with a superior degree of precision.

If the improved apparatus appears to be successful in registering reasonably frequent events during preliminary running trials near Ithaca, plans may be carried out to build a number of observing stations and operate them in the vicinity of a one hundred square mile conventional air shower particle detection array operated by the Cornell-Sydney University Astronomy Center at a site near Narrabri in Australia. Situating the two experiments near one another provides the possibility of detecting the same air shower by both methods thus allowing an intercalibration of the two measuring techniques, in addition to a mutual reinforcement of the accuracy for the data taken on individual showers (such as particle density, arrival times, and arrival directions). An apparatus designed to detect radio pulses and experiments for studying the details of air shower cores would also share the same location. In effect the information obtained by comparing the results from the different experiments would add to the knowledge derived from each measurement alone.

References

1. J. Delvaille, F. Kendziorski and K. Greisen, Jour. Phys. Soc. Japan 17, Supplement A-III, 76 (1962).

2. J. Linsley, Phys. Rev. Letters 10, 146 (1963).

3. K. Greisen, Proc. Intnl. Conf. Cosmic Rays (London, 1965), 609.

4. H. Bradt et al., Proc. Intnl. Conf. Cosmic Rays (London, 1965), 715.

5. G. B. Khristiansen et al., ibid., p. 799.

6. J. V. Jelley, Cerenkov Radiation (Pergamon Press, London, 1958), Chap. 9.

7. A. Chudakov, unpublished graph.

8. James S. Brunner, Sea Level Cerenkov Light Intensities Due to Extensive Air Showers (Master's thesis, Cornell Univ., 1962).

9. D. A. Hill et al., Proc. 5th Inter-American Seminar on Cosmic Rays (Bolivia, 1962).

10. F. G. Smith, N. A. Porter and J. V. Jelley, Proc. Intnl. Conf. Cosmic Rays (London, 1965), 701.

11. N. A. Porter et al., ibid., p. 706.

12. F. D. Kahn and I. Lerche, Proc. Roy. Soc. A 289, 206 (1966).

13. Sterling A. Colgate, preprint, Oct. 1, 1965.

14. K. Suga, Proc. 5th Inter-American Seminar on Cosmic Rays (Bolivia, 1962).

15. A. Chudakov, discussion following reference 14.

16. G. W. Clark et al., Phys. Rev. 122, 637 (1961).

17. C. W. Allen, Astrophysical Quantities (Athlone Press, London, 1955), 2nd ed., p. 256.

18. A. D. Bray et al., Proc. Intnl. Conf. Cosmic Rays (London, 1965), 668.

19. J. Linsley and L. Scarsi, Phys. Rev. Letters 9, 123 (1962).

20. W. K. H. Panofsky and M. Phillips, Classical Electricity and Magnetism (Addison-Wesley, Reading, Mass., 1962), 2nd ed., p. 366.

21. C. W. Allen, Astrophysical Quantities (Athlone Press, London, 1955), 2nd ed., p. 253.

22. C. W. Allen, ibid., p. 269.

23. A. A. Penzias and R. W. Wilson, Astrophys. J. 142, 419 (1965).

24. K. Greisen, Phys. Rev. Letters 16, 748 (1966).

25. F. Hoyle, Phys. Rev. Letters 15, 131 (1965).

26. J. V. Jelley, Phys. Rev. Letters 16, 479 (1966).

27. R. J. Gould and G. Schreder, Phys. Rev. Letters 16, 252 (1966).

28. Alan N. Bunner, Cosmic Ray Detection by Atmospheric Fluorescence, (Ph.D. thesis, Cornell Univ., 1966).

29. P. L. Hartman and H. Hoerlin, Bull. Am. Phys. Soc. 7, Ser. II, 69 (1962).

30. D. T. Stewart and E. Gabathuler, Proc. Phys. Soc. 72, 287 (1958).

31. Alan N. Bunner, The Atmosphere as a Cosmic Ray Scintillator (Master's thesis, Cornell Univ., 1964).

32. C. W. Allen, Astrophysical Quantities (Athlone Press, London, 1955), 2nd ed., p. 135.

33. K. I. Greisen, Progress in Cosmic Ray Physics, ed. by J. G. Wilson (North-Holland, Amsterdam, 1956), Vol. III, p. 17.

34. David Ophir and Uzia Galil, Electronics 34, No. 28, 68, 70 (July 14, 1961).

35. F. Landford-Smith, ed. Radiotron Designer's Handbook (Radio Corp. of America, Harrison, N.J., 1953), 4th ed., p. 175.

36. F. A. Jenkins and H. E. White, Fundamentals of Optics (McGraw-Hill, New York, 1957), 3rd ed., p. 510.

37. J. A. Steers, An Introduction to the Study of Map Projections (Univ. of London Press, 1950).

38. C. Hastings, Jr., Approximations for Digital Computers (Princeton Univ. Press, 1955), p. 169.

39. R. A. Minzner, K.S.W. Champion, H. L. Pond, The ARDC Model Atmosphere 1959 (AFCRC-TR-59-267), Air Force Surveys in Geophysics No. 115, Air Force Cambridge Research Center, Bedford, Mass., p. 12.

40. C. W. Allen, Astrophysical Quantities (Athlone Press, London, 1955), 2nd ed., p. 122.

41. W. A. Baum and L. Dunkelman, J. Opt. Soc. Amer. 45, 166 (1955).

42. J. F. Carlson and J. R. Oppenheimer, Phys. Rev. 51, 220 (1936).

43. H. J. Bhabha and W. Heitler, Proc. Roy. Soc. London A 159, 432 (1937).

44. B. Rossi and K. Greisen, Rev. Mod. Phys. 13, 240 (1941).

45. H. S. Snyder, Phys. Rev. 76, 1563 (1949).

46. K. I. Greisen, Progress in Cosmic Ray Physics, ed. by J. G. Wilson (North-Holland, Amsterdam, 1956), Vol. III, pp. 10-12.

47. Goro Tanahashi, J. Phys. Soc. Japan 20, 883 (1965).

48. William Galbraith, Extensive Air Showers (Academic Press, New York, 1958), pp. 13-25.

49. C. G. Bell, Jr., and F. N. Hayes, ed. Liquid Scintillation Counting (Proceedings of a conference on Liquid Scintillation Counting held at Northwestern Univ., Aug. 20-22, 1957), Pergamon Press, 1958, p. 23.